JOHANNES GUTENBERG-UNIVERSITÄT MAINZ

Radioactive negative ions: Production and laser spectroscopy at ISOLDE

Author:

David LEIMBACH

born in Schwalmstadt,

Hessen

A thesis submitted in fulfillment of the requirements

for the degree of Doktor rer. nat.

in the

AG Wendt/LARISSA

Fachbereich Mathematik, Physik und Informatik

Geneva, July 1, 2021

ii

Declaration of Authorship

I, David LEIMBACH, declare that this thesis titled, "Radioactive negative ions: Production and laser spectroscopy at ISOLDE" and the work presented in it are my own. I confirm that:

- This work was done wholly or mainly while in candidature for a research degree at this University.

- Where any part of this thesis has previously been submitted for a degree or any other qualification at this University or any other institution, this has been clearly stated.

- Where I have consulted the published work of others, this is always clearly attributed.

- Where I have quoted from the work of others, the source is always given. With the exception of such quotations, this thesis is entirely my own work.

- I have acknowledged all main sources of help.

- Where the thesis is based on work done by myself jointly with others, I have made clear exactly what was done by others and what I have contributed myself.

Signed:

_____

Date:

_____

"All we have to decide is what to do with the time that is given to us. "

Gandalf, "*The fellowship of the Ring*" by J.R.R. Tolkien

Abstract

Radioactive negative ions: Production and laser spectroscopy at ISOLDE

by David LEIMBACH

Negative ions are fragile quantum systems in which electron correlation effects play a significant role in the binding of the extra electron to the atom or molecule. Hence, negative ions are of interest to gain insight into fundamental atomic properties by probing theory beyond the independent particle model. However, due to the shallow binding potential, the binding energy of the extra electron, referred to as electron affinity (EA) is typically the only atomic parameter which can be determined with high precision.

This thesis concerns production and spectroscopy of radioactive negative ions at CERN-ISOLDE. A key result in the study of radioactive negative ions is presented with the determination of the electron affinity of astatine by means of collinear laser photodetachment spectroscopy. This experiment was performed utilising the **G**othenburg **AN**ion **D**etector for **A**ffinity measurements by **L**aser **PH**otodetachment (GANDALPH), which underwent a detector upgrade to allow for operation in the UV spectrum using a novel, fully transparent graphene target. The EA of astatine was determined to be $2.41578(7)$ eV, which not only serves as a milestone towards the investigation of other heavy and eventually super-heavy negative ions, but also facilitates the use of astatine in targeted radionuclide therapy of cancer by revealing some of its fundamental chemical behaviour.

Furthermore, work towards the improvement of the sensitivity of laser photodetachment threshold spectroscopy was performed by utilising a Multi

Reflection Time of Flight (MR-ToF) device. In respect to the production of radioactive negative ions, efforts have been made to increase the production efficiency and broaden the availability of negative ions at ISOLDE. As an alternative low work function surface ioniser material, $SrVO_3$ was produced and characterised and alternatively the use of caesiated metal surfaces was explored. Furthermore, sputter type negative ion production was investigated utilising a FEBIAD type ion source as well as the modified KENIS ion source.

Acknowledgements

Removed due to copyright.

Contents

List of Figures

List of Tables

List of Abbreviations

CEM	Channel Electron Multiplier
CERN	Conseil Européen pour la Recherche Nucléaire
COLLAPS	COLlinear Laser Spectroscopy
CRIS	Collinear Resonance Ionisation Spectroscopy
DC-CCSD(T)	Dirac Coulomb- Coupled Cluster Single, Double and perturbative Triple excitations
DESIREE	Double ElectroStatic Ion Ring ExpEriment
EA	Electron Affinity
EN-MME-MM	ENgineering department - Mechanical and Materials Engineering group - Materials, Metrology and non-destructive testing
FC	Faraday Cup
FEBIAD	Forced Electron Beam Induced Arc Discharge
GANDALPH	Gothenburg ANion Detector for Affinity measurements by Laser PHotodetachment
GANDIS	GANDALPH Ion Source
GPS	General Purpose Separator
GUNILLA	Gothenburg University Negative Ion Laser LAboratory
HIE-ISOLDE	High Intensity and Energy ISOLDE
HRS	High Resolution Separator
INTC	ISOLDE and Neutron Time of flight Comittee
IP	Ionisation Potential
ISCOOL	ISOLDE COOLer

ISOL	**I**sotope **S**eparator **O**n**L**ine
ISOLDE	**I**sotope **S**eparator **O**n**L**ine **DE**vice
ITER	**I**nternational **T**hermonuclear **E**xperimental **R**eactor
KENIS	**K**inetic **E**jection **N**egative **I**on **S**ource
LASER	**L**ight **A**mplification by **S**timulated **E**mission of **R**adiation
LHC	**L**arge **H**adron **C**ollider
LINAC	**LIN**ear **AC**celerator
LIST	**L**aser **I**on **S**ource and **T**rap
LS2	**L**ong **S**hutdown **2**
MCP	**M**ulti **C**hannel **P**latae
MEDICIS	**MED**ical **I**sotopes **C**ollected from **IS**OLDE
MIRACLS	**M**ulti **I**on **R**eflection **A**pparatus for **C**ollinear **L**aser **S**pectroscopy
MR-ToF	**M**ulti **R**eflection **T**ime **of** **F**light
NMS	**N**ormal **M**ass **S**hift
PUMA	anti**P**roton **U**nstable **M**atter **A**nnihilation
QED	**Q**uantum **E**lectro **D**ynamics
QMF	**Q**uadrupole **M**ass **F**ilter
RIB	**R**adioactive **I**on **B**eam
RILIS	**R**esonance **I**onisation **L**aser **I**on **S**ource
RFQcb	**R**adio **F**requency **Q**uadrupole **c**ooler **b**uncher
SEM	**S**econdary **E**lectron **M**ultiplier
SMS	**S**pecific **M**ass **S**hift
SNICS	**S**ource of **N**egative **I**ons by **C**aesium **S**puttering
SY-STI-RBS	**SY**stems department- **S**ources **T**argets and **I**nteractions-

	Radioactive **B**eam **S**ources
TE-VSC-SCC	**TE**chnology department - **V**acuum, **S**urface and **C**oating group- **S**urface **C**oating and **C**hemistry section
UPS	**U**ltraviolet **P**hotoelectron **S**pectroscopy
VADIS	**V**ersatile **A**rc **D**ischarge **I**on **S**ource
VADLIS	**V**ersatile **A**rc **D**ischarge **L**aser **I**on **S**ource
XPS	**X**-ray **P**hotoelectron **S**pectroscopy
XRD	**X**- **R**ay **D**iffraction

Physical Constants

Bohr magneton	$\mu_B = 9.274\,010\,078\,3(28) \times 10^{-24}\,\text{J}\,\text{T}^{-1}$
Boltzman constant	$k_B = 1.380\,649 \times 10^{-23}\,\text{J}\,\text{K}^{-1}$ (exact)
Electron mass	$m_e = 9.109\,383\,701\,5(28) \times 10^{-31}\,\text{kg}$
Landé factor of the electron	$g_s = 2.002\,319\,304\,362\,56(35)$
Nuclear magneton	$\mu_N = 5.050\,783\,7461(15)\,\text{e-27 J T}^{-1}$
Plank's constant	$h = 6.626\,070\,15 \times 10^{-34}\,\text{J}\,\text{Hz}^{-1}$ (exact)
Proton mass	$m_p = 1.672\,621\,923\,69(51) \times 10^{-27}\,\text{kg}$
Richardson constant	$A_0 = 1.201\,73 \times 10^6\,\text{Am}^{-2}\,\text{K}^{-2}$
Rydberg constant	$R_\infty = 10\,973\,731.568\,160(21)\,\text{m}^{-1}$
Speed of Light	$c_0 = 2.997\,924\,58 \times 10^8\,\text{m}\,\text{s}^{-1}$ (exact)
Vacuum electric permittivity	$\epsilon_0 = 8.854\,187\,812\,8(13) \times 10^{-12}\,\text{F}\,\text{m}^{-1}$
Vacuum permeability	$\mu_0 = 1.256\,637\,062\,12(19) \times 10^{-6}\,\text{N}\,\text{A}^{-2}$

List of Symbols

A	Mass number [u]
a	Spin-orbit coupling constant [eV]
A_{HFS}	Hyperfine constant [eV]
A_{S}	Sputtering yield [%]
A_{R}	Material specific Richardson constant [A$/$(m^{2}K^2)]
$\vec{B}$	Magnetic field [T]
b	Material specific correction factor
B_l	Magnetic field caused by the angular momentum of the electron [T]
B_J	Magnetic field caused by the total angular momentum of the electron [T]
B_{Q_s}	Hyperfine structure coupling of the second order derivation of the electronic charge distribution [eV]
d	Distance [m]
d_{l}	Lattice parameter [m]
d_{if}	Transition dipole moment [C m]
E	Total energy [eV]
E_{E}	Electric field strength [V$/$m]
$\vec{E}$	Electric field vector [V$/$m]
EA	Electron affinity [eV]
E_B	Binding energy [eV]
E_{e}	Electron energy [eV]
E_{ground}	Lowest hyperfine structure level of the ground state of an atom or ion [eV]
E_{l_i,l_j}	Angular momentum coupling energy [eV]

E_n	Energy eigenvalues [eV]
E_{ph}	Photon energy [eV]
E_{s_i,s_j}	Spin coupling energy [eV]
E_{thr}	Threshold energy [eV]
E_{max}	Maximum energy [eV]
E_{min}	Minimum energy [eV]
E_F	Fermi level [eV]
$E_{hfs,F}$	Hyperfine energy levels of the atomic ground state [eV]
$\vec{F}_L$	Lorentz force [N]
F	Total angular momentum of the atom
F_{FS}	Field effect constant [Hz m^{-2}]
$F_{centrifugal}$	Centrifugal force [N]
f	Adjustment factor for the determination of the VADIS ionisation efficiency
g_0	Statistical weight of the atomic states
g_{ion}	Statistical weight of the ionic states
g_N	Nuclear Landé factor
H	Total Hamiltonian [eV]
H_e	Hamiltonian representing the kinetic energy of the individual electron [eV]
H_{ee}	Hamiltonian representing the inter-electron repulsion [eV]
I	Nuclear spin
I_e	Electron current [A]
i	Imaginary unit
I^-	Negative ion current due to secondary emission [A]
I^+	Positive caesium ion current [A]
I_{ion}	Ion current [A]
I_{atom}	Particle current [A]
IP	Ionisation potential [eV]

J	Total angular momentum number
j	Total angular momentum of the individual electron
j_e	Current density [A/m]
k	Linear momentum [kg m s^{-1}]
K_{NMS}	Normal mass shift component of the isotope shift [u Hz]
K_{SMS}	Specific mass shift component of the isotope shift [u Hz]
L	Total angular momentum
L_0	Length [m]
l	Angular momentum quantum number
l_N	Number of electrons in the valence shell
m	Mass [u]
$m/\Delta m$	Mass resolution
m_A	Mass of isotope A [u]
$m_{A'}$	Mass of isotope A$'$ [u]
M_J	Seconday total angular momentum quantum number
m_l	Magnetic quantum number
m_s	Secondary spin quantum number
n	Principle quantum number
n_0	Gas density [m^{-3}]
n_e	Electron density [m^{-3}]
n_{ions}	Ion density [m^{-3}]
P	Transition probability [s^{-1}]
P_2	Second order Legendre polynomial
Q_s	Electric quadrupole moment [C m^2]
q	Charge [C]
r	Radius/distance [m]
r_0	Half of the distance between two quadrupole rods [m]

$<r>$	Average radius [m]
$\vec{r}$	Position vector [m]
$R_{nl}(r)$	Radial component of the wave function [m$^{-3/2}$]
S	Total spin
S_M	Softness [eV^{-1}]
S_{out}	Area of the extraction hole [cm^2]
T	Temperature [K]
t	Time [s]
U	Applied electric potential [V]
U_{QMF}	Voltage applied to quadrupole rods [V]
$V(r)$	Potential in dependence of distance [eV]
V_{eff}	Effective potential [eV]
v	Velocity [m s^{-1}]
$<v^2_{rel}>$	Variance of the angle [rad^2]
$<x^2>$	Variance of the position [m^2]
Y_{lm_l}	Angular component of the wave function
Z	Atomic mass number [u]
z	Position in z-direction [m]
α	Degree of ionisation
α_C	Courant-Snyder parameter
α_D	Dipole polarisability of the atom [C m^2 V^1]
β	Asymmetry parameter
β_C	Courant-Snyder parameter
γ_C	Courant-Snyder parameter
ΔE	Fine structure level splitting [eV]
ΔE_{HFS}	Hyperfine structure splitting [eV]
$\Delta E_{HFS,Q}$	Hyperfine splitting component caused by nuclear electric quadrupole moment [eV]
Δm	Full width half maximum of a mass peak [u]
$\delta\nu^{A,A'}$	Isotope shift in the transition frequency between two atomic levels of different isotopes [Hz]

$\Delta\phi$	Work function reduction due to the Schottky effect [eV]
$\Delta\Phi_{ac}$	Accumulated phase
$\delta\langle r^2\rangle_{A,A'}$	Difference in the mean square charge radii of the nucleus [m^2]
ϵ_{is}	Ionisation efficiency [%]
ϵ_{transp}	Transport efficiency [%]
ϵ	Emittance [π mm mrad]
ϵ_{95}	95% transverse emittance [π mm mrad]
ϵ_{rms}	Root-mean-square emittance [π mm mrad]
ζ	Fraction of the speed of light
η^-	Efficiency of negative ion production in the secondary emission process [%]
η	Hardness [eV]
Θ	Heaviside function
κ	Number of wall collisions of the atom
λ	Wavelength [nm]
μ	Reduced mass [kg]
μ_d	Electronic dipole transition moment operator [C m]
μ_K	Nuclear magneton [J/T]
μ_s	Magnetic moment of the spin [J/T]
ν	Frequency [Hz]
ρ_f	Density of states [J^{-1}]
σ	Cross section [m^2]
σ_d	Electron detachment cross section [m^2]
$\frac{d\sigma}{d\Theta}$	Differential cross section [m^2 sr^{-1}]
τ	Trapping efficiency [%]
Φ	Work function [eV]
$\phi_{QMF}(\vec{r},t)$	Potential between quadrupole rods [V]
$\phi(J,I)$	Angle between J and I [rad]
χ_i	Spin function of the individual electron

χ_M	Electronegativity [eV]
Ψ	Wave function [$m^{-3/2}$]
ψ	Single electron wave function [$m^{-3/2}$]
ω	Angular frequency [1/s]
ω_e	Electrophilicity [eV]

Chapter 1

Introduction

In 1897, Sir Joseph John Thomson discovered that cathode rays consist of negatively charged particles, orders of magnitude smaller than the size of an atom [1], later named electrons. Thomson continued his investigations of charged particles in gases (for which he was awarded with the Nobel prize in physics 1906 [2]), utilising and improving the technique of mass spectrometry by extending previous work by Goldstein [3] and Wien [4]. This work lead Thomson to the first measurement on different stable isotopes of one element using neon ions in 1912 [5] as well as to the observation of negatively charged atoms and molecules in gas-discharges in 1913 [6], the first experiment ever to describe negative ions in the gas-phase.

Further experimental and theoretical findings by Planck [7], Einstein [8], Bohr [9] and Heisenberg [10] in the early twentieth century lead to the formulation of quantum mechanics, which describes the properties and behaviour of all particles with size in the order of molecules, atoms and below. This representation of the microscopic world resulted not only in a more fundamental understanding of those systems as well as related phenomena like radioactivity or optical emission, but gave rise to modern fields of applications and operational areas like the domain of photonics and the laser, the wide range of microelectronics and computers, the entire field using nuclear energy as well as solar power and finally day-to-day utilisation in mobile communication and the global positioning system (GPS). The mathematical formalism to describe quantum systems was first developed by Schrödinger [11] for non-relativistic and Dirac [12] for relativistic cases.

Due to their complexity, most quantum systems except e.g. the hydrogen or hydrogen-like atoms, cannot be quantitatively described by analytical formulae, but require approximations and simplifications. One of the most common theoretical approaches for the description of electromagnetic interactions in atomic systems is the mean-field approximation, where e.g. electromagnetic forces in between electrons are replaced by a mean field, essentially treating the electrons as independent particles within the strong Coulomb field of the nucleus [13].

For negative ions however, this approximation gives no meaningful results: Since the Coulomb potential of the nucleus is almost entirely screened, the binding of the additional electron in a negative ion is primarily due to correlations between the electrons, resulting only in a shallow dipole binding potential. Consequently, negative ions are sensitive probes for electron correlation theories that go beyond the mean field theory or independent particle approximation [14]. Due to the shallow binding potential, the binding energy of the additional electron, referred to as electron affinity (EA), is about an order of magnitude smaller than the ionisation potential (IP), the binding energy of the outermost valence electron in a neutral atom. Consequently, there typically exist no bound excited states with opposite parity in negative ions with noticeable exceptions being lanthanum [15], cerium[16], osmium [17] and thorium [18].

Experimental investigations to determine the EA with high precision are usually performed utilising laser photodetachment threshold spectroscopy [19, 14]. Here, a laser beam is overlapped with a negative ion beam, which can absorb a photon with sufficient energy to detach the electron, resulting in a free electron and a neutral atom. By measuring the cross section of photodetachment as a function of the photon energy, the electron affinity can be determined. First photodetachment experiments were performed by Branscomb in the 1950s on oxygen and hydrogen [20, 21], long after Massey had published the first compendium on negative ions in 1938 [22]. Since then, the EAs of most of the stable elements were determined and are available in publications such as those from Hotop *et al.* [23, 24] and Andersen *et*

al. [25]. Most recently, the EAs of thorium [18] and the lanthanides terbium, praseodymium and neodymium [26] were determined experimentally. An alternative method for high precision measurements of the EA is the use of the photodetachment microscope developed by Blondel [27, 28], where the interference of the outgoing electron wave in a static electric field is measured.

In addition to photodetachment studies determining the EA of an element, individual detachment channels can be investigated using a resonance laser ionisation scheme for detection [29], whereas measurements of angular distributions of the outgoing electron can give insight into the electronic states [30]. Recent developments include velocity map imaging and use the Abel inversion to recreate the three dimensional distribution of photoelectrons [31]. Furthermore, in storage rings such as DESIREE in Stockholm, Sweden [32], lifetime studies of meta-stable and doubly excited states of negative ions can be performed [33, 34]. Comprehensive overviews of the information on negative ions can be found in the reviews of Andersen [14] and Pegg [19].

Besides probing fundamental theory, negative ions are also of interest in a broad range of other research fields and applications: Due to the occurence of excited levels connected by strong allowed transitions to the grund state of the negative ion, lanthanum is a very promising candidate for laser cooling, which would potentially be of interest for sympathetic cooling of antihydrogen [35]. Furthermore, the PUMA experiment proposed at CERN [36] is aiming towards using exotic positive and negative ions to study antimatter [37].

In astrophysics, negative hydrogen ions are suggested to play a role in the creation of the hydrogen molecule in the early universe [38, 39, 40] and dominate the visible opacity in stars with photospheric temperatures smaller than $7000\,\text{K}$, like the sun [40]. In addition, C_6H^- anions and other hydrocarbons and carbon nitrides have been found in interstellar clouds [41]. In earth's atmosphere, photodetachment of anions plays a part as an electron donor in the lowest layer of the ionosphere [42]. TOKAMAK-type fusion

reactors such as the **I**nternational **T**hermonuclear **E**xpermimental **R**eactor (ITER) [43] in France, utilise negative ions to heat the fusion plasma confined in a toroidal magnetic field: Since the injection of charged particles would change the plasma conditions, negative ion beams of up to 40 A are accelerated towards the deuterium-tritium plasma and neutralised with a stripper foil or photodetached before entering the plasma chamber [44, 45].

In accelerator mass spectrometry, negative ions are used to suppress contaminants from the ion beam. One of the most utilised examples of this is the creation of negative ^{14}C beams for accurate carbon dating via the ^{14}C-method [46, 47, 48, 49] while suppressing nitrogen contaminants, which does not form a negative ion.

Only in recent years, studies of radioactive negative ions were performed, starting with the measurement of the EA of a radioactive isotope of iodine [50] and astatine [51], a measurement performed within the framework of this thesis.

In order to study these rare elements and specifically short-lived isotopes, they have to be produced at on-line facilities where they can immediately be guided to an experimental station as radioactive ion beams (RIBs) to investigate their nuclear and atomic properties by laser or decay spectroscopy [52, 53, 54] as well as high precision mass measurements [55]. One of the worldwide leading facilities is the **I**sotope **S**eparator **O**nLine **DE**vice (ISOLDE) at CERN, Geneva [56]. Here, a proton beam with an energy of 1.4 GeV is impinged on a thick target to induce nuclear reactions and in this way produce a broad range of elements and isotopes. These species are subsequently ionised in a dedicated ion source, extracted and mass separated for delivery to the subsequent experiments. Most commonly, positive ions are created at ISOLDE, but negative ions can be produced as well [57].

Although negative ions are more fragile than their positive counterparts, they can be created in several ways: Cesium sputter sources are commonly used to produce up to microamperes of ion beam current of most stable elements, as summarised by Middleton [58]. Other methods include the use of a plasma ion source or a charge exchange cell [59, 60]. Especially for elements

with high electron affinity like the halogens, surface ion sources utilising a low work function ioniser are feasible [59, 61]. For radioactive ion beam production, efficiency, emittance and release time of the ion source have to be considered specifically, since there is typically only a microscopic amount of the element available, which furthermore decays rapidly. Additionally, the robustness of the source is crucial, since it has to withstand the high temperatures, a variety of chemically reactive elements and the radioactive environment it is used in. Currently, the negative ion source at ISOLDE, referred to as MK4, is utilising a LaB_6 surface ioniser, which can efficiently produce high affinity elements such as the halogens [62]. However, the LaB_6 surface is prone to poisoning by e.g. carbon compounds [63] and starts to decompose at temperatures higher than 1500 °C [59]. Therefore, to support the pointed out increasing demand on investigations on negative exotic ions, there is a need for a robust negative ion source with high efficiency.

This thesis aims to advance experimental studies of radioactive negative ions. In chapter 5, possibilities to increase the availability and efficiency of radioactive negative ions at ISOLDE are investigated by exploring improvements of the current surface ion source as well as other ionisation methods applied. In chapter 6, the laser spectroscopic work of this thesis is presented, focussing on the determination of the electron affinity of astatine, which represents a first milestone in the study of heavy radioactive negative ions. Furthermore, efforts of improving the spectral resolution and overall quality of the signal from rare negative ions by utilising a multi-reflection time of flight device are discussed in preparation of measurements of the isotope shift of the EA as well as upcoming examinations of heavy and eventually superheavy radioisotopes are presented.

Chapter 2

Fundamentals

2.1 Atomic physics

In the late nineteenth and early twentieth century, the understanding of the structure and mechanics of microscopic particles such as atoms was revolutionised with the formulation of quantum mechanics. A detailed description and in depth derivation of the principles of atomic physics can be found in various textbooks [13, 64, 65]. In this chapter, the concepts and fundamental principles necessary for the work performed in this thesis are introduced.

Based on the ideas of N. Bohr [9] and L. de Broglie [66] and inspired by P. Debye, E. Schrödinger postulated a fundamental equation of quantum mechanics, which was later on entitled as Schrödinger-equation [11] which he soon extended into the Klein-Gordon equation in the early twentieth century, introducing the wave function Ψ of a system. The wave function describes the state of a quantum system and the absolute square $|\Psi|^2$ the probability density of its position or momentum. The Schrödinger-equation in its general form can be written as

$$H|\Psi\rangle = -i\hbar\frac{\delta}{\delta t}|\Psi\rangle, \qquad (2.1)$$

where H is the Hamiltonian of the system, i the imaginary unit, t the time, $\hbar = \frac{h}{2\pi}$ the reduced Planck constant and Ψ the wave function.

2.1.1 Single electron systems: The hydrogen atom

One of the simplest atomic cases that can be solved by the Schrödinger-equation is the hydrogen atom (or hydrogen-like atoms), where the system is

comprised of only one electron in the outer shell, referred to as valence elec-
tron, moving within the Coulomb potential of the positive nucleus. There,
the two particle Hamiltonian can be written as

$$H = -\frac{\hbar^2}{2m_\mathrm{p}}\Delta_\mathrm{p} - \frac{\hbar^2}{2m_\mathrm{e}}\Delta_\mathrm{e} + V(r), \qquad (2.2)$$

where $V(r) = -\frac{e^2}{4\pi\epsilon_0 r^2}$ is the Coulomb potential, $\hbar$ the reduced planck con-
stant, $\Delta_\mathrm{p,e}$ the Laplace operator and $m_\mathrm{p,e}$, $+e$ and $-e$ are the masses and
charges of proton and electron, respectively.

Using the reduced mass $\mu = \frac{m_\mathrm{e} m_\mathrm{p}}{m_\mathrm{e} + m_\mathrm{p}}$, the center of mass motion and the
relative motion of the electron can be separated, resulting in a Hamiltonian

$$H = \frac{\hbar^2}{2\mu}\Delta + V(r) \qquad (2.3)$$

for the electron. Additionally, since there is no time-dependence in Eq. (2.3),
the Schrödinger-equation can be simplified into its stationary form:

$$H|\Psi\rangle = [\frac{\hbar^2}{2\mu}\Delta + V(r)]|\Psi\rangle = E|\Psi\rangle \qquad (2.4)$$

where E is the energy. Eq. (2.4) can then be solved by transforming into
spherical coordinates and using the ansatz

$$\Psi(r) = R_{nl}(r) \cdot Y_{lm_l}(\theta, \phi) \qquad (2.5)$$

where $Y_{lm_l}(\theta, \phi)$ and $R_{nl}(r)$ are separated functions for the angular and radial
components respectively, characterized by the quantum numbers n, l, and m_l.
Here, $n = 1, 2, 3, ...$ is the principal quantum number, $l = 0, 1, 2, ..n - 1$ is the
angular momentum quantum number and $m_l = -l, -l + 1, ..., l - 1, l$ is the
magnetic quantum number.

Eq. 2.4 can then be separated into a radial

$$\frac{\hbar^2}{2\mu}(\frac{dR}{dr^2} + \frac{2}{r}\frac{dR}{dr}) + [E - [\frac{\hbar^2}{2\mu}\frac{l(l+1)}{r^2} + V(r)]]R_{nl}(r) = 0 \qquad (2.6)$$

and angular equation

$$\frac{1}{\sin(\theta)}\frac{d}{d\theta}\left(\sin(\theta)\frac{Y_{lm_l}(\theta,\phi)}{d\theta}\right) + \frac{1}{\sin^2(\theta)}\frac{d^2Y_{lm_l}(\theta,\phi)}{\phi^2} = -l(l+1)Y_{lm_l}(\theta,\phi).$$
(2.7)

In Eq. (2.6), the term $\frac{\hbar^2}{2\mu}\frac{l(l+1)}{r^2}$ is referred to as centrifugal barrier due to its repulsive nature as indicated by its sign. Combined with $V(r)$, this gives an effective potential of

$$V_{eff}(r) = V(r) + \frac{\hbar^2}{2\mu}\frac{l(l+1)}{r^2}.$$
(2.8)

Solving Eq. (2.7) and Eq. (2.6) (in detail shown in textbooks such as by W. Demtröder [13]) then leads to energy eigenvalues E_n of the hydrogen atom given by

$$E_n = -\frac{\mu e^4}{2\hbar^2(4\pi\epsilon_0)^2 n^2} = -\frac{R_\mu}{n^2}$$
(2.9)

where R_μ is the mass-reduced Rydberg constant.

2.1.2 Fine structure

In addition to its orbital angular momentum mentioned above, the electron itself also exhibits an angular momentum-like property referred to as its spin $|\vec{s}| = \sqrt{s(s+1)}\hbar$ with its component in z-direction $m_s = \pm\frac{1}{2}\hbar$. The state of an individual electron is described by its four quantum numbers n, l, m_l, m_s, while the configuration of N equivalent electrons in a subshell is given by nl^N, where $l = 0, 1, 2, ..$ is denoted as letters $s, p, d, f, g, ..$ with j being omitted. The interaction of the spin with the angular momentum, called spin-orbit coupling, results in a splitting of the energy levels in the atom: The spin of the electron induces a magnetic moment

$$\vec{\mu}_s = -g_s\frac{e}{2m_e}\vec{s} = -g_s\frac{\mu_B}{\hbar}\vec{s},$$
(2.10)

where μ_B is the Bohr magneton and $g_s \approx 2$ the Landé factor of the electron. This magnetic moment interacts with the magnetic field $\vec{B}_l = \frac{\mu_0 Ze}{8\pi r^3 m_e}\vec{l}$ caused

by the electrons angular momentum l, inducing a shift in the energy levels ΔE given by

$$\Delta E = -\vec{\mu}_s \cdot \vec{B}_l = g_s \mu_B \frac{\mu_0 Z e}{8\pi\hbar r^3 m_e} \vec{s} \cdot \vec{l} \approx \frac{\mu_0 Z e^2}{4\pi r^3 m_e^2} \vec{s} \cdot \vec{l}. \tag{2.11}$$

Introducing the total angular momentum $\vec{j} = \vec{l} + \vec{s}$ with $|\vec{j}| = \sqrt{j(j+1)}\hbar$ and substituting into Eq. (2.11) yields

$$\Delta E = \frac{a}{2}[j(j+1) - l(l+1) - s(s+1)] \tag{2.12}$$

with the spin orbit-coupling constant $a = \frac{\mu_0 Z e^2 \hbar^2}{4\pi r^3 m_e^2}$.

The energy shift due to spin-orbit coupling combined with relativistic effects such as corrections for relativistic kinetic energies as well as non-localization effects is referred to as **fine structure** [13]. Fine structure level splittings are typically in the order of 1×10^{-4} eV to 1×10^{-1} eV.

2.1.3   Hyperfine structure

The **hyperfine structure** describes the splitting of the atomic levels caused by the interaction of the valence electron with the electric and magnetic moments of the nucleus. As an example, Figure 2.1 shows the level splitting in the hydrogen atom due to the fine structure and hyperfine structure. Similar to the electron, the nucleus possesses a spin $|\vec{I}| = \sqrt{I(I+1)}\hbar$ as an angular momentum, resulting in a magnetic moment $\vec{\mu}_N = g_N \frac{\mu_K}{\hbar} \vec{I}$, where g_N is the nuclear g-factor, and $\mu_K = \frac{\hbar e}{2m_p}$ the nuclear magneton. Analogous to the fine structure splitting, one can then determine the energy shift ΔE_{HFS} with the magnetic field B_J resulting from the total angular momentum of the electron as

$$\Delta E_{HFS} = -\vec{\mu}_B \cdot \vec{B}_J = -|\vec{\mu}_B| \cdot B_J \cos(\phi(J, I)), \tag{2.13}$$

where $\phi(J, I)$ is the angle between $\vec{J}$ and $\vec{I}$. With the total angular momentum of the atom $F = J + I$, Eq. (2.13) can be written as

$$\Delta E_{HFS} = \frac{A_{HFS}}{2}[F(F+1) - J(J+1) - I(I+1)], \tag{2.14}$$

Principle levels   Fine structure levels   Hyperfine structure levels
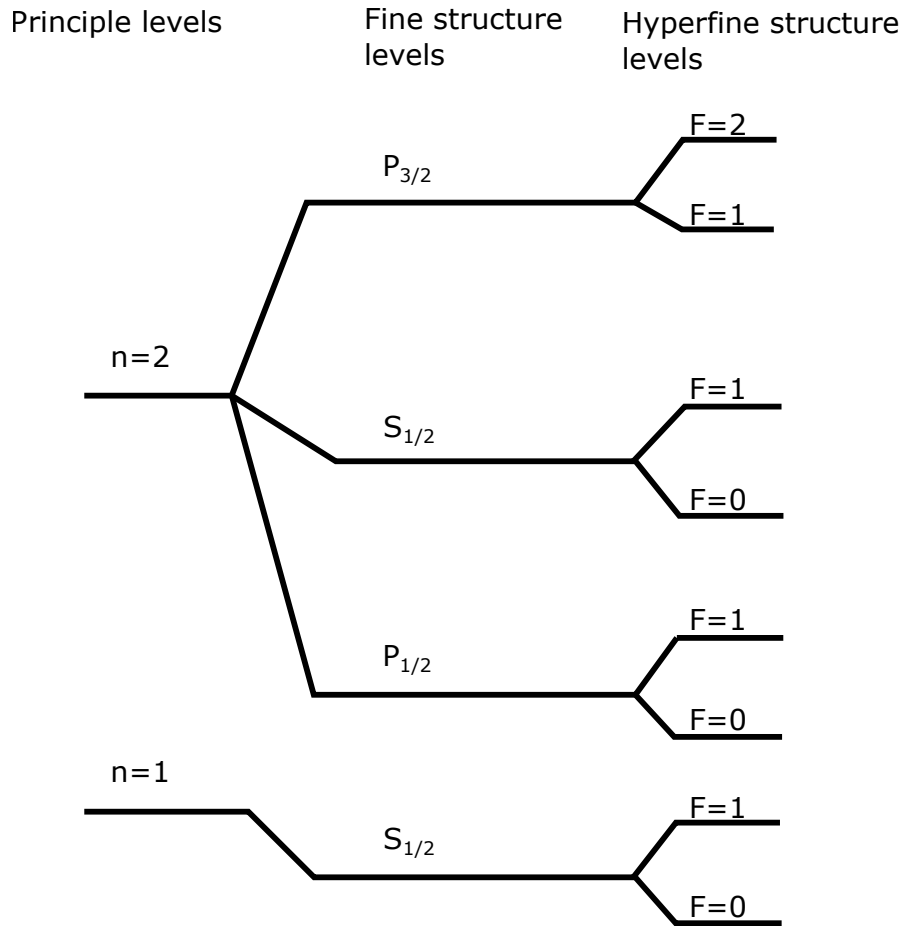
FIGURE 2.1: Fine structure and hyperfine structure splitting of the hydrogen atom. Not drawn to scale.

with the hyperfine constant $A_{\text{HFS}} = \frac{g_{\text{N}}\mu_{\text{K}}B_J}{\sqrt{J(J+1)}}$.

For nuclei with $I > \frac{1}{2}$, there can be an additional contribution to the hyperfine structure due to the interaction of a nuclear electric quadrupole moment with the electronic shell, given by

$$\Delta E_{\text{HFS},Q} = \frac{B_Q}{4} \cdot \frac{\frac{3}{2}(C+1) - 2I(I+1)J(J+1)}{(2I-1)J(2J-1)} \tag{2.15}$$

where $C = F(F+1) - J(J+1) - I(I+1)$ and $B_{Q_s} = eQ_s[\frac{\delta^2 V_e}{\delta z^2}](r=0)$ represents the coupling of the second order derivation of the electronic charge distribution with the nuclear electric quadrupole moment Q_s. The order of magnitude of the hyperfine structure splitting is typically between $1 \times 10^{-7}\,\text{eV}$ and $1 \times 10^{-4}\,\text{eV}$.

2.1.4   Isotope shift

Atoms with the same number of protons but a different number of neutrons are called isotopes. Energy differences in the same positions of the atomic levels of individual isotopes lead to shifts in the optical transitions between two isotopes that are called isotope shifts. An energy shift that arises due to the difference in mass is referred to as *mass shift*, which can be further divided into the *normal mass shift* (NMS) and the *specific mass shift* (SMS).

The *normal mass shift* describes only single valence electron systems accurately by accounting for the difference in the reduced mass of two isotopes in positions of their electronic energy level.

The *specific mass shift* is the additional shift resulting from the electron correlation in multi-electron atoms. Overall, the contribution of the mass shift to the isotope shift is dominant for isotopes with low atomic masses.

Additionally, the charge distribution in the nuclei of the individual isotopes of an element differs, altering the electric field experienced by the electrons, also causing a shift in the atomic levels. This is called *field shift* or *volume shift*. Combining these effects, the shift $\delta \nu^{A,A'}$ in transition frequency between two atomic levels of different isotopes A and A$'$ can be written as

$$\delta \nu^{A,A'} = (K_{\text{NMS}} + K_{\text{SMS}}) \frac{m_A - m_{A'}}{m_A \cdot m_{A'}} + F_{\text{FS}} \delta \langle r^2 \rangle_{A,A'}, \tag{2.16}$$

where $K_{\text{NMS,SMS}}$ are the contributions from the normal and specific mass shift, respectively, F_{FS} the field effect constant and $\delta \langle r^2 \rangle_{A,A'}$ the difference in the mean square charge radii of the nucleus for the two isotopes A and A$'$. The first term is accounting for the mass shift and the second for the field shift.

2.1.5   Multi-electron systems

For multi-electron systems, electron-electron interactions have to be taken into account, increasing the complexity of the atomic system. The non-relativistic Hamiltonian for the electronic wave function without spin-orbit

coupling is given by

$$H = H_{\mathrm{e}} + H_{\mathrm{ee}} + V(r_i) = -\frac{\hbar^2}{2m_{\mathrm{e}}}\sum_i \Delta_i + \sum_{i,j,i\neq j}\frac{e^2}{4\pi\epsilon_0 r_{ij}} - \frac{Ze^2}{4\pi\epsilon_0 r_i} \qquad (2.17)$$

where H_{e} represents the kinetic energy of the individual electron, $V(r_i)$ the Coulomb potential from the nucleus and H_{ee} the inter-electron repulsion.

As a result of the electron-electron interaction, the Hamiltonian can not be reduced to a simple hydrogen-like problem. Consequently, very few atomic systems can be solved analytically and approximations and numerical methods are needed.

One such approximation is the independent particle model as used in the Hartree-Fock method. Here, the individual particle interactions are simplified by assuming a mean field with which an electron interacts, neglecting the fluctuations arising from electron-electron interactions. The resulting Schrödinger equation for one electron is then hydrogen-like and can be solved with a similar ansatz:

$$\psi_i = R_{nl_i}(r) \cdot Y_{lm_l i}(\theta, \phi) \cdot \chi_i(s_i), \qquad (2.18)$$

where χ_i is the spin function and $R_{nl_i}(r)$, $Y_{lm_l i}(\theta, \phi)$ are the radial and angular components. Accounting for parity and the Pauli-exclusion principle, the multi-electron wave function Ψ can be written as a Slater-determinant

$$\Psi = \frac{1}{\sqrt{N!}} \begin{vmatrix} \psi_1(1) & \psi_2(1) & \psi_3(1) & \dots & \psi_N(1) \\ \psi_1(2) & \psi_2(2) & \psi_3(2) & \dots & \psi_N(2) \\ \dots & \dots & \dots & \dots & \dots \\ \psi_1(N) & \psi_2(N) & \psi_3(N) & \dots & \psi_N(N) \end{vmatrix}.$$

The energy

$$E = <\Psi|H|\Psi> \qquad (2.19)$$

of the system can be determined iteratively by applying the variational principle with regards to ψ_i until the the solution converges within a certain precision, as shown in detail in textbooks such as by W. Demtröder [13] and C.

J. Foot [64].

LS coupling

In multi-electron systems, there are several possible spin-orbit coupling mechanisms. If the coupling energy of the angular momentum $E_{l_i,l_j} = a_{ij}\vec{l_i} \cdot \vec{l_j}$ and spin $E_{s_i,s_j} = b_{ij}\vec{s_i} \cdot \vec{s_j}$ between electrons is large in comparison to the individual spin-orbit coupling, the angular momenta and spins combine to a total angular momentum $L = \sum_i l_i$ and a total spin $S = \sum_i s_i$ [13]. This is referred to as LS-coupling. The fine structure components of the term are then given by the total angular momentum number $\vec{J} = \vec{L} + \vec{S}$ and individual atomic levels are described by the term symbol $n^{2S+1}L_J$, where $2S + 1$ is the spin multiplicity, giving the amount of possible fine structure states. The total angular momentum is given as letters S,P,D,F (ongoing in alphabetical order with J omitted) instead of numbers. The LS coupling is the dominant coupling mechanism for valence electrons in light elements with $Z < 30$ [13].

jj coupling

If the energy of the individual spin orbit coupling of an electron is larger than the one between different electrons, so called jj coupling describes the system better. Here, each electron's spin and angular momentum couple to a total angular momentum $j_i = l_i + s_i$ of the electron. The total angular momentum of the system is then given by $\vec{J} = \sum_i j_i$. Pure jj coupling occurs mainly for heavy elements with $Z > 60$, e.g. lead, while an intermediate coupling scheme is realised in the middle region of the periodic table. A more detailed discussion of coupling mechanisms in multi electron systems including intermediate coupling mechanisms can be found in textbooks such as by W. Demtröder [13] and C. J. Foot [64].

2.1.6   Selection rules

For absorption of a photon by an atom or ion, certain selection rules have to be obeyed: The transition dipole moment d_{if} between two electronic states is

given by:

$$d_{if} = < \Psi_f | \mu_d | \Psi_i > = e \int \Psi_f \, \vec{r} \, \Psi_i \, d^3r \qquad (2.20)$$

where Ψ_i and Ψ_f are the initial and final states and μ_d the electronic dipole transition moment operator. Furthermore, the transition probability P per unit of time for a transition from initial to final state according to Fermi's golden rule is given by

$$P = \frac{2\pi}{\hbar} d_{if}^2 \rho_f \qquad (2.21)$$

where ρ_f is the density of states. Since the dipole moment operator has an odd parity, only transitions between states with opposite parity lead to a non-vanishing transition probability. These transitions are called allowed, while higher order multi-pole transitions are significantly less likely and thus are called forbidden. However, these transitions, can still occur, e.g. induced by high power laser irradiation. Additional rigorous selection rules are:

$$\Delta J = 0, \pm 1, \quad 0 \Longleftrightarrow 0 \text{ forbidden}$$
$$\Delta M_J = 0, \pm 1, \qquad (2.22)$$

where M_J is the magnetic quantum number, given by the projection of the total angular momentum vector in z direction $J_z = M_J \cdot \hbar$. Furthermore, there are additional selection rules for the various cases of spin-orbit coupling as well as hyperfine structure transitions, all of which are discussed in detail in the textbooks by W. Demtröder [13] and C. J. Foot [64].

2.2 Negative ions

Negative ions are the quantum systems focussed on in this thesis. A negative ion is an atom or molecule with one or more additional electrons, generating a net negative charge. In neutral atoms and positive ions, the bonding of the electrons is dominated by the Coulomb potential resulting from the positively charged nucleus. However, for negative ions this is not the case: For a free electron approaching a neutral atom, the Coulomb attraction is effectively screened by the electrons surrounding the nucleus.

However, the electron will induce an electric dipole moment in the atom, similar to the process of Van-der-Waals bonding between neutral atoms. This induced dipole potential, which depends on the correlation of the valence electrons, of the atom and the incident electron, in turn can bind the electron to the atom, creating a negative ion. The binding potential for this outermost electron in the negative ion is then given by

$$V(r) = \frac{l(l+1)}{2r^2} - \frac{\alpha_D}{2r^4} \tag{2.23}$$

where r is the distance of the electron from the nucleus, α_D the dipole polarisability of the atom and $\frac{l(l+1)}{2r^2}$ the centrifugal barrier as described in Eq. (2.6). However, Eq. (2.23) is not valid for distances comparable with those of the electron orbitals, when the Coulomb attraction of the nucleus is not fully screened and therefore contributing to the binding energy.

Due to the significant contribution of electron correlation effects to the binding energy, approximations such as the independent particle model used e.g. in the Hartree-Fock method break down, resulting in the need for more sophisticated approaches, such as the coupled cluster method used in publication C. The binding energy gained when attaching an electron to a neutral atom is called *electron affinity* (EA), and is given by

$$\text{EA}(A) = E_{\text{ground}}(A) - E_{\text{ground}}(A^-), \tag{2.24}$$

where $E_{\text{ground}}(A; A^-)$ are the lowest hyperfine structure levels of the ground states of the neutral atom A and the negative ion A^-, respectively [67].

Due to the shallow binding potential in negative ions, the EA of an element is typically only in the range of 1 eV, while about fourteen elements do not form stable negative ions at all, as shown in Figure 2.2. In comparison, the energy needed to remove an electron from the neutral atom, referred to as ionisation potential (IP) is about an order of magnitude greater. For example, the EA of hydrogen is $0.754\,195(19)$ eV [68], while its IP is $13.598\,434\,49(8)$ eV [69]. Consequently, in most cases, negative ions only exhibit a single bound-state configuration with some known exceptions such as lanthanum [15], os-

mium [17], cerium [16] and the recently measured thorium [18], where bound excited states with opposite parity have been observed. In turn, this makes e.g. lanthanum a candidate for laser cooling, which would potentially be of interest for sympathetic cooling of antiprotons [35].
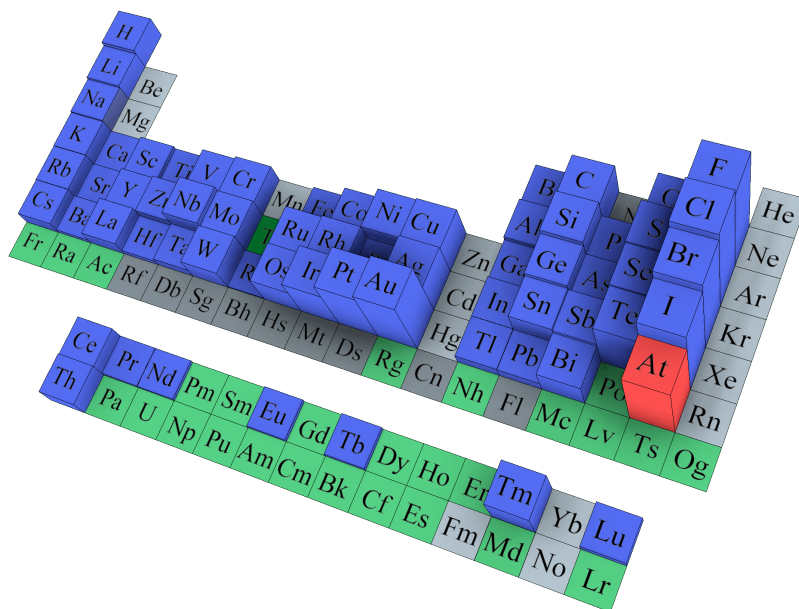
FIGURE 2.2: The periodic table of elements, where the height of the column corresponds to the value of the EA. Blue represents experimentally determined EAs, green elements which are theoretically predicted to form stable negative ions, light grey for for those that do not. Dark grey is indicating for which elements neither theoretical predictions nor experimental values are available. Astatine is highlighted as the measurement of the EA(At) was performed within the framework of this thesis. (Figure courtesy of J. Warbinek.)

An overview of the theoretically and experimentally known EAs is shown in Figure 2.2, where the periodic table of elements is illustrated, with the height of the column representing the value of the EA. In general, the EA increases as an atomic shell is filled, while elements with closed shell atomic structures are observed to have very low EAs or do not even form stable negative ions at all. Consequently, the group of elements with the largest EAs are the halogens with EAs ranging from 3.612 725(28) eV for chlorine [70] to 2.415 78(7) eV for astatine [51], while the noble gases, which do not form stable negative ions, possess a negative EA. Furthermore, a decrease of the EA from top to bottom within a group is generally expected due to the

change in the atomic radius. However, the EA of the second element of a group tends to possess the largest EA as is the case for e.g. the halogens and chalcogens. This can be attributed to the increased electron-electron repulsion in the smaller $n = 2$ shell.

TABLE 2.1: Predicted and experimentally determined EAs for the lanthanides and actinides.

Lanthanide	EA [eV]	Reference	Actinide	EA [eV]	Ref.
La	0.557 546(20)	[71]	Ac	0.221	[72]
Ce	0.57(2)	[73]	Th	0.607690(60)	[18]
Pr	0.109 23(46)	[26]	Pa	0.384	[72]
Nd	0.09748(31)	[26]	U	0.373	[72]
Pm	0.129	[74]	Np	0.313	[72]
Sm	0.162	[74]	Pu	0.085	[72]
Eu	0.116(13)	[75]	Am	0.076	[72]
Gd	0.137	[74]	Cm	0.321	[72]
Tb	0.13131(79)	[26]	Bk	0.031	[72]
Dy	0.063(2)	[72]	Cf	0.018	[72]
Ho	0.338	[74]	Es	0.002	[76]
Er	0.312	[74]	Fm	-0.1	[76]
Tm	1.029(22)	[77]	Md	1.0	[76]
Yb	-0.3	[78]	No	-0.3	[76]
Lu	0.238 8(7)	[79]	Lr	0.465	[72]

In the case of the noble metals, the EA even increases within the group e.g. from 1.235 78(4) eV [80] for copper to 2.308 610(25) eV for gold [25] due to an increase of relativistic effects for the heavier elements resulting in an enhancement of the binding of the s electrons. Regarding the lanthanides and the iso-electronic actinides, very low EA values are expected as shown in table 2.1, which for most cases have not been measured yet [78, 76, 72].

Theoretical predictions are limited by the necessity of describing the very complex atomic structures.

2.2.1 Doubly excited states

Although only rarely bound excited states are observed in negative ions, quasi-bound excited states can exist in the continuum above the detachment threshold. By absorbing a photon, the negative ion can be promoted into a doubly excited state, which then decays into one of several possible lower lying states of the neutral atom and a free electron. In photodetachment spectra, doubly excited states are visible as resonances in the cross section spectrum. Comparable to auto-ionising states in neutral atoms, these states involve the simultaneous excitation of two electrons possibly including a core electron and are therefore referred to as doubly excited states. The possible transitions into and from a doubly excited state are shown schematically in Figure 2.3. A more detailed discussion and investigations of doubly excited
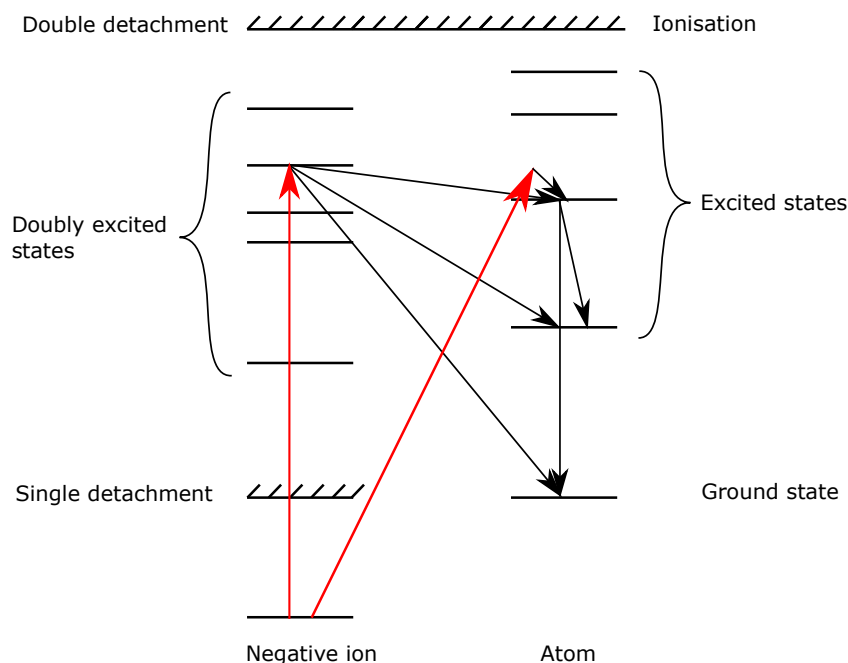
FIGURE 2.3: Level structure in negative ions. When the negative ion absorbs a photon (red arrows) an electron can be photodetached via a doubly excited state or directly into a state of the neutral atom. From an excited level of the neutral atom, the electron decays back into the ground state.

states of negative ions can be found e.g. in the thesis of J. Rohlen [81] as well
as in reviews such as those by H.S.W. Massey [82] and D.R. Bates [83].

2.2.2   Molecular negative ions

In case of molecular negative ions, the determination of the the EA is more
difficult due to the additional rotational and vibrational states of the molecule,
resulting in a variety of possible photodetachment channels. In addition, the
most likely transitions are not necessarily into the vibrational ground state of
the neutral molecule, as described by the Franck-Condon principle [84, 85].

In contrast, by applying the Born-Oppenheimer approximation, it is as-
sumed that the electron transition is quasi instantaneous compared to the
nuclear motion as illustrated in Figure 2.4.
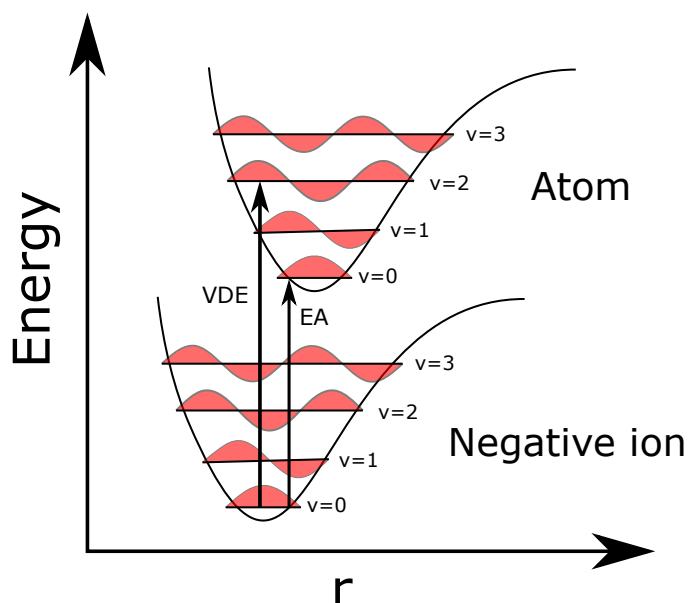
FIGURE 2.4: Level diagram of the ground states of an molec-
ular anion and the corresponding atom. The respective vibra-
tional states ν are indicated with their wave function in red on
horizontal lines. The adiabatic EA and the vertical detachment
energy are shown by arrows.

Hence, in molecular negative ions, the electron affinity defined as the en-
ergy difference between the vibrational ground state of the negative ion and
the neutral respectively, is called *adiabatic electron affinity*. Furthermore, the
vertical detachment energy (VDE) is defined as the energy needed to detach an

electron from the electronic and vibrational ground state of the negative ion without changing the intra-nuclear distance.

Experimentally, the EA of molecular anions can be determined in storage ring experiments such as DESIREE in Stockholm, Sweden [86] with the capability to cool down the ions into their vibrational ground states.

2.3   Photodetachment spectroscopy

Since the invention of the laser as light source, the most precise way to determine the electron affinity of an element or molecule is by laser photodetachment, where a laser beam is superimposed with a beam of negative ions.

If the photon energy $h\nu$ is greater than the electron affinity of the negative ion A^-, the ion can be neutralized and either the neutral particle, the detached electron (e^-) or both can be detected:

$$A^- + h\nu \rightarrow A + e^-. \tag{2.25}$$

In case of photodetachment, the electron is far from the core, hence the centrifugal barrier term in Eq. (2.23) is the dominating potential. As a result, the cross-section σ of the detachment process in the threshold region can be described by the Wigner threshold law, derived in [87],

$$\sigma \propto k^{2l+1}, \tag{2.26}$$

where k is the linear momentum and l is the orbital angular momentum of the detached electron [87]. Eq. (2.26) written in terms of energy gives

$$\sigma(E) \propto (E_{ph} - E_{thr})^{l+\frac{1}{2}}, \tag{2.27}$$

where $E_{ph} = h\nu$ is the energy of the photon, E_{thr} the threshold energy necessary to detach the electron, ie. the EA, and l the orbital angular momentum quantum number of the emitted electron.

According to the electric dipole transition rules (see section 2.1.6), the angular momentum of the detached electron is given by $l = l_0 \pm 1$, where l_0

is the initial angular momentum of the bound electron. Electrons detached from an s state with $l_0 = 0$ will be emitted with $l = 1$, giving rise to a slow onset, as shown as p-wave in Figure 2.5.
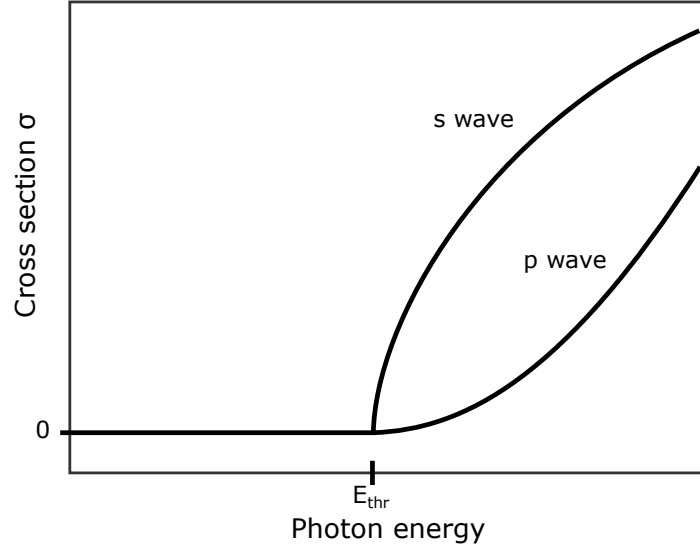
FIGURE 2.5: Photodetachment cross section close to the threshold. For photon energies below the threshold, the cross section is zero. Electrons detached from a p-state will be emitted as s-wave.

For electrons detached from states with higher l , $l = l_0 - 1$ is dominating close to the threshold due to the centrifugal barrier potential (see Eq. (2.23)). For example, electrons detached from a p state are almost exclusively emitted as s-wave electrons with $l = 0$ where the cross section follows a sharp, square root behaviour.

When multiple states are involved in the photodetachment process, the total cross section is given as the sum of the partial cross sections of each detachment channel

$$\sigma(E_{\mathrm{ph}}) = \sum_i E_{\mathrm{ph}} - (\mathrm{EA} + E_i)^{(l+\frac{1}{2})} \Theta\left(E_{\mathrm{ph}} - (\mathrm{EA} + E_i)\right), \qquad (2.28)$$

where E_i is the energy of the respective state, E_{ph} the photon energy, EA the electron affinity and Θ the Heaviside function. O'Malley treated the threshold behavior by including the polarisation of the neutral atom by the outgoing electron (i.e. treating the full potential of Eq. (2.23)), leading to an

alternative formulation of the threshold law including higher order terms [88, 89]. For double detachment processes, Wannier predicts a nearly linear threshold law [90]:

$$\sigma \propto E^{1.127} \tag{2.29}$$

In Figure 2.6, the general cross section behaviour is shown in a broader energy range. Around the threshold region, the cross section behaves according to the Wigner law (as shown in Figure 2.5), then increasing up to a maximum, where the wave functions of the initial state in the negative ion and the free electron overlap optimally and falls off to zero beyond.
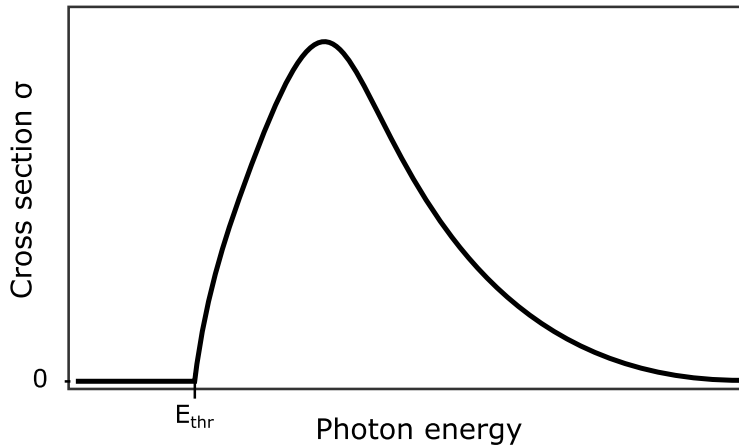
FIGURE 2.6: Wigner threshold law without excited states. Before the threshold, the cross section is zero, afterwards it increases according to the Wigner law. Eventually, a maximum is reached after which the cross section drops back down to zero. Doubly excited states are seen as resonances.

If present, doubly excited states are visible as resonances. As pointed out in the thesis of P. Andersson [91], assuming the negative ion as a square potential well, the de Broglie wavelength λ of the outgoing electron at the point of maximum cross section can be related to the average radius $< r >$ of the negative ion as

$$\lambda = n \cdot < r >, \quad n = \begin{cases} 2 & \text{for s-wave electron} \\ 4 & \text{for p-wave electron} \end{cases}. \tag{2.30}$$

This can be used to gain an approximation of the size of negative ions as well

as trends along a group of elements, especially for closed shell systems such as the halogens.

2.3.1 Laser photodetachment threshold spectroscopy

In laser photodetachment threshold spectroscopy, an ion beam is overlapped either collinear or perpendicular with a laser beam as shown in Figure 2.7. Subsequently, either the ion velocity or the laser frequency ν is scanned across the threshold region of detachment, and either resulting neutral particles or photo-electrons are detected. In both collinear and perpendicular geometries, one has to account for the Doppler shift arising from the velocity difference of ions and photons, given by:

$$E' = E \cdot \frac{1 - \zeta \, \cos(\theta)}{\sqrt{1 - \zeta^2}}, \tag{2.31}$$

where E' is the Doppler-corrected photon energy, $\zeta = \frac{v}{c_0}$, v the ion beam velocity, c_0 the speed of light in vacuum and θ the angle between the ion and laser beams.
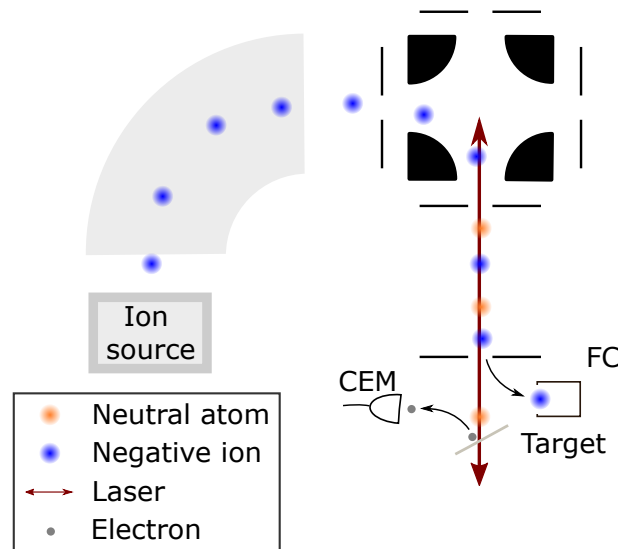
FIGURE 2.7: Schematic view of laser photodetachment threshold spectroscopy. A laser beam is superimposed collinearly with a negative ion beam. Detached neutral atoms impinge on a target, creating secondary electrons detected with a Channel Electron Multiplier (CEM). Residual charged particles are deflected into a Faraday cup.

Another advantage of the collinear geometry is a much greater interaction volume, since the integrated spatial overlap between laser and ion beam is greater. In addition, in the collinear case, the Doppler spread of the ions is compressed due to the acceleration of all the ions by the same extraction potential in the ion source [92, 93]. As a result of the cosine dependence, slight shifts in angle for a perpendicular geometry result in greater deviations than in the collinear case. Furthermore, when a measurement can be performed in both parallel and anti-parallel direction, the Doppler shift can be eliminated to all orders when taking the geometric mean of anti-parallel and parallel results.

In this case, the accuracy is determined by the uncertainties in the laser bandwidth or frequency measurement. However, if the measurement can only be performed in one direction, the precision with which the velocity of the ions is known is limiting the accuracy of this technique.

2.3.2 Laser photodetachment electron spectroscopy

In laser photodetachment electron spectroscopy, the energy of the detached electron is measured to determine the electron affinity. As shown in Figure 2.8, a laser with a photon energy above threshold is overlapped with the negative ion beam and subsequently the energy of the electron is measured. The electron energy can be determined either using a deflecting electrostatic or magnetic field or by measuring the time of flight of the electron.

If the energy levels of the neutral atom are known, the EA and the energy of any excited states can be determined by

$$\text{EA} = E_{\text{ph}} - E_{\text{e}}, \tag{2.32}$$

where $E_{\text{ph}} = h\nu$ is the photon energy and E_{e} the energy of the electron. However, the accuracy of the determination of the EA is limited by the precision with which electron energies can be measured, which is significantly lower than that of laser photodetachment threshold spectroscopy, where the photon frequency is measured.
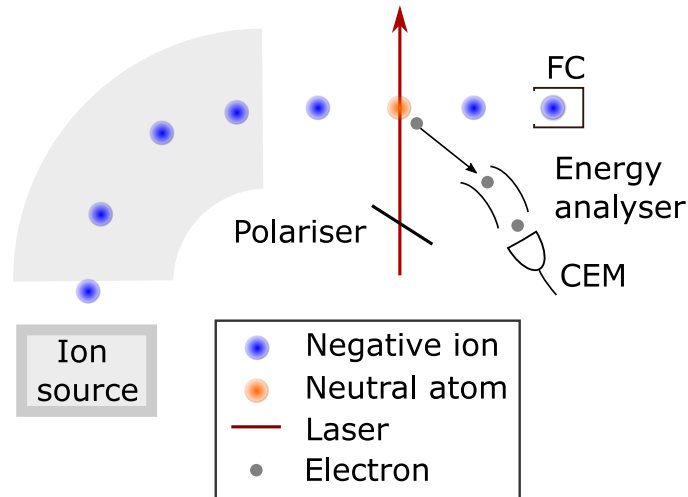
FIGURE 2.8: Photoelectron spectroscopy. A laser is intersected perpendicular with a negative ion beam. The detached electrons are guided into an electron energy analyser, residual negative ions are detected in a Faraday cup.

The difficulty in determining the electron energy is partly due to its sensitivity towards electric and magnetic fields (e.g. earths magnetic field), in particular since electrons emitted around threshold possess energies with only a few eV or less. The advantage of this method is the possibility to gain more information about the electronic states of the negative ion: If the laser light is polarised, the angular momentum of the detached electrons can be determined by measuring their angular distribution. The differential cross section is given by

$$\frac{d\sigma}{d\Theta} = \frac{\sigma}{4\pi}(1 + \beta P_2(\cos(\theta)))   \tag{2.33}$$

where σ is the total cross section, θ the angle between the ion momentum and the polarisation of the laser light, Θ the solid angle, β the asymmetry parameter and P_2 the second order Legendre polynomial [30]. By comparing the ratio between two perpendicular differential cross sections $C = \frac{\sigma(\theta=90)}{\sigma(\theta=0)}$, the asymmetry parameter β

$$\beta = \frac{1 - C}{1 + \frac{C}{2}}   \tag{2.34}$$

can be determined. The asymmetry parameter in turn contains information on the relative amplitudes and phases of the partial waves that represent the

free electron in the final state as discussed in detailed in [94, 30].

2.3.3 Laser photodetachment microscopy

Another method to precisely investigate negative ions developed by Blondel *et al.* is laser photodetachment microscopy [27]. A beam of negative ions is intersected perpendicular with a laser in the presence of a weak uniform electric field as shown in Figure 2.9. Due the lack of long-range attraction from the residual atom, the detached electron can be considered as free electron. In a semi-classical picture, the electron is guided by the electric field on a parabolic trajectory towards a detector plate where each point on the plate can be reached by two distinct trajectories, giving rise to an interference pattern [27]. In a quantum mechnical point of view, the spherical wave function of the free electron is folded back onto itself by the electric field, therefore interfering with itself [14]. This interference pattern can be observed with e.g. a multi channel plate.

In order to avoid uncertainties through a slight misalignment of the necessary 90° angle, oftentimes the laser beam is intentionally misaligned and retro-reflected, leading to two interference patterns. The average of those two patterns then gives the actual energy of the electron. The accumulated phase $\Delta\Phi_{\mathrm{ac}}$ is then given by

$$\Delta\Phi_{\mathrm{ac}} = \frac{4\sqrt{2}}{3}\frac{\sqrt{m}}{\hbar q E_{\mathrm{E}}}E_{\mathrm{e}}^{3/2}, \tag{2.35}$$

where q is the electric charge, E_{E} the applied electric field, and E_{e} the initial kinetic energy of the electron [95]. The EA can then be derived from $E = h\nu - \mathrm{EA}$.

In 2020, Eklund et al. [31] demonstrated a tomographic imaging method capable of recreating the full three dimensional photoelectron distribution without limitations for the laser polarisation by applying a so called inverse Radon transform [96] on photodetached electrons using an electron velocity imaging spectrometer similar to the setup depicted in Figure 2.9.
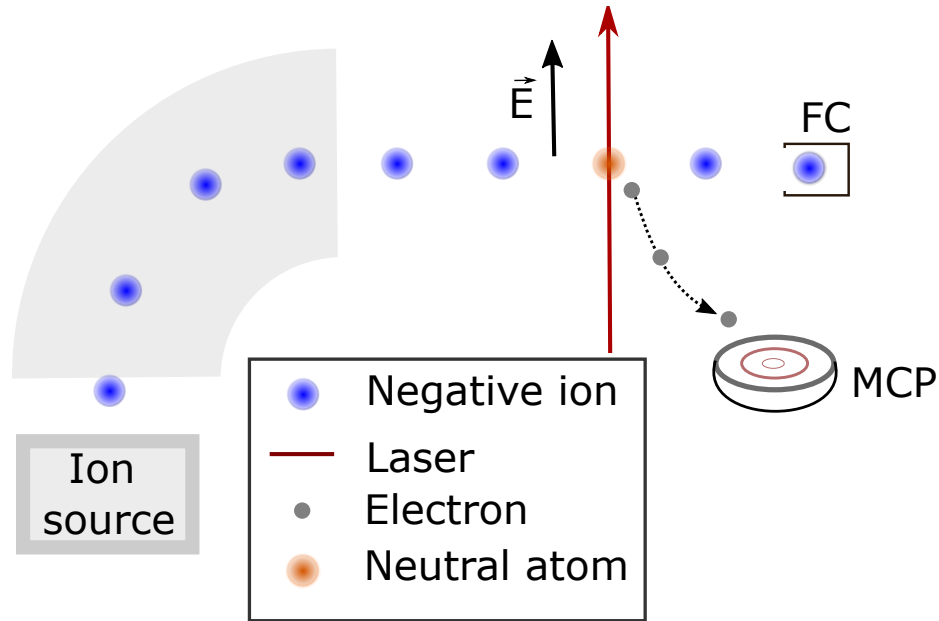
FIGURE 2.9: Schematic view of photodetachment microscopy. A detached electron is interfering with itself due to an static external electric field. The interference pattern can then be detected by a position sensitive detector such as a MCP.

2.4   Negative ion sources

In the following section a brief overview is given over the mechanisms to produce negative ions relevant for the work presented in this thesis. A broader overview is given in various textbooks [59, 97].

2.4.1   Surface ion sources

When an atom is desorbed from a hot surface, it can gain or lose an electron in the process, creating a negative or positive ion respectively. The ionisation probability for this process is given by the Saha-Langmuir equation, derived from the Saha-equation in the early twentieth century [98, 99]:

$$\alpha = \frac{N_{\mathrm{ion}}}{N_0} = \frac{g_{\mathrm{ion}}}{g_0} \exp\left(\frac{\beta}{k_{\mathrm{B}} T}\right); \quad \beta = \begin{cases} EA - \Phi & \text{for negative ionisation} \\ \Phi - \mathrm{IP} & \text{for positive ionisation} \end{cases}$$

$$(2.36)$$

Here, α is the degree of ionisation, N_{ion} and N_0 are the number densities of ions and neutral atoms respectively, k_{B} the Boltzmann constant, T the equilibrium temperature of the system in Kelvin and $g_{0,\text{ion}} = 2\sum_i s_i + 1$ the statistical weights of the ionic and neutral states with spin s_i of the individual electron respectively, Φ is the work function of the ioniser surface, EA the electron affinity of the atom and IP the ionisation potential of the atom.

The ionisation efficiency ϵ_{is} for a surface ion source, assuming one interaction between neutral atom and surface, is then given by

$$\epsilon_{\text{is}} = \frac{N_{\text{ion}}}{N_{\text{ion}} + N_0} = \frac{\alpha}{1 + \alpha}. \tag{2.37}$$

In order to achieve a high ionisation efficiency, the ioniser material, in particular its work function and stability at high temperatures, is of crucial importance. For negative ion production, a material with a low work function (i.e. $\Phi < 3\,\text{eV}$) is needed to yield high efficiencies. Most commonly, lanthanum hexaboride (LaB_6), with a work function of about 2.6 eV [100, 101] is used as a surface ioniser. LaB_6 has shown to be thermally stable up to about 1500 °C and has produced negative ion beams of halogens with efficiencies in the order of 10 % [102]. However, for elements with EAs lower than this
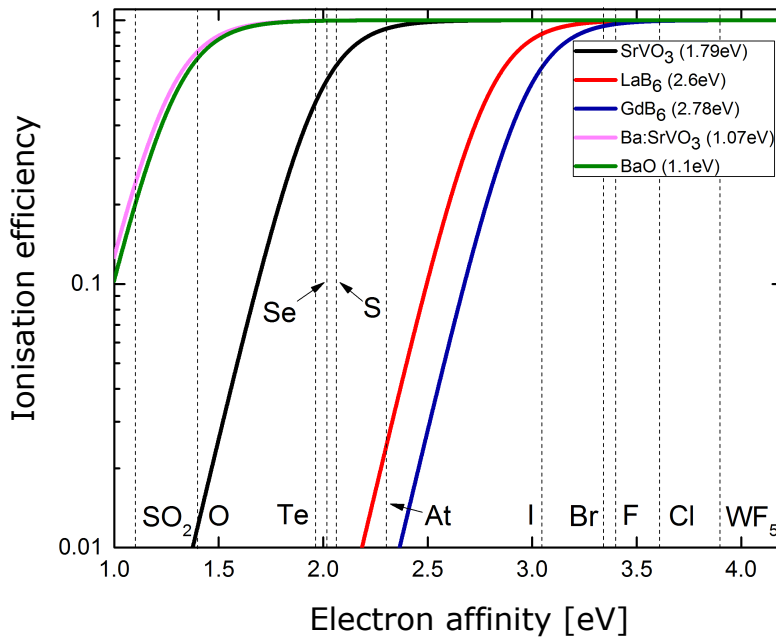
FIGURE 2.10: Surface ionisation efficiency for different ionisers and elements at 1500 K. Taken from [103].

work function, the ionisation efficiency drops drastically, as can easily be calculated from equation (2.36) and is shown in Figure 2.10 for different ioniser materials.

In addition, it has been shown that LaB_6 ion sources are prone to poisoning when getting into contact with carbon or other highly reactive chemical elements or molecules including fluorine, thereby increasing its effective work function [57]. As a result, negative surface ion sources have mainly been used for beams of halogens, the group of elements with the highest EAs. For example, the determination of the EA of astatine in publication C was performed using an LaB_6 surface ioniser to produce negative beams of astatine at the ISOLDE facility.

2.4.2   Caesium sputter sources

One of the most common ways to produce a variety of negative ion beams of stable elements are by means of caesium sputtering. Here, a beam of positive caesium ions is accelerated with an energy of a few keV onto a cathode containing the desired element. The caesium will sputter fragments off the cathode material as well as create a surface layer of caesium on the cathode, thereby reducing its work function, as shown in Figure 2.11.

As a consequence, fragments sputtered out of the cathode have to pass through the caesium layer, increasing the probability of picking up an electron. The ion current I^- of this process, called secondary emission, is given by

$$I^- = I^+ A_S \eta^- \exp\left(-n_0 L_0 \sigma_d\right), \tag{2.38}$$

where I^+ is the positive ion current of caesium, A_S is the sputtering yield, η^- the efficiency of the negative ion production, σ_d the electron detachment cross section and n_0 the gas density in the ion beam path of length L_0 [59]. The cathode usually consists of a metal cylinder with a hole in which the desired species is pressed to avoid heating or electrical charge up. For the same reason, non-conducting target materials are often mixed with conducting ones such as silver powder. In order to prevent elements with a low

melting point to evaporate, the cathode is additionally water cooled.
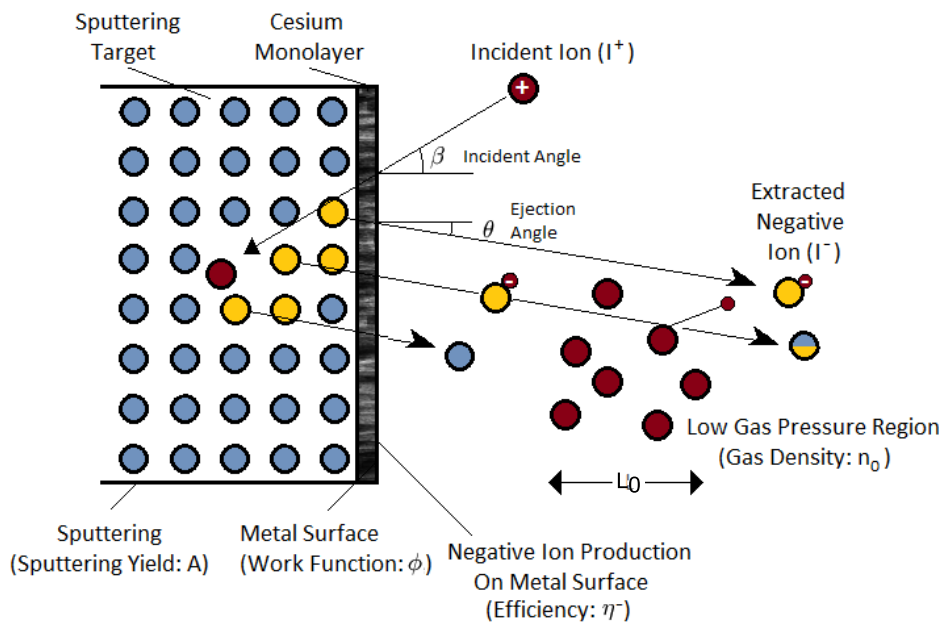
FIGURE 2.11: The process of secondary negative ion emission. An atom is sputtered or reflected and picks up an electron via passing through the caesium monolayer. Illustration taken from [103].

Krohn [104] first discovered that the presence of caesium in a sputter source increased the negative ion yield. Ming *et al.* proposed a tunneling mechanism to explain the work function dependence in sputtering [105]. Several sources using caesium as sputtering agent were developed and improved by e.g. Alton [106] and Middleton [107] .

Currently, one of the most commonly used sputter sources, the **S**ource of **N**egative **I**ons by **C**aesium **S**puttering (SNICS), shown schematically in Figure 2.12, was developed independently by Middleton [108] as well as J.H. Billen and H.T. Richards [109]. Here, the caesium is kept in a reservoir which can be heated externally. Neutral caesium atoms then diffuse through a feeding tube onto a heated cylindrical or spherical surface ioniser where they are ionised positively. The ioniser is kept at a positive potential of a few keV with respect to the cathode, resulting in an acceleration of caesium ions towards the cathode. The electric field applied for caesium acceleration can then be used to extract the produced negative ions through a central hole in the caesium ioniser.

A detailed collection of suitable cathode materials for each element with their respective expected negative ion mass spectra was published by Middleton in "A Negative Ion Cookbook" [58]. Detailed reviews of caesium sputter sources and the ionisation mechanisms involved are given e.g. by Alton [110, 111] and Mori [112]. In this thesis, the sputter ionisation method was investigated for the production of negative ions at the ISOLDE facility with the KENIS ion source, which was developed at Oak Ridge National Laboratory for negatively charged fluorine beams (see chapter 3 and 6).
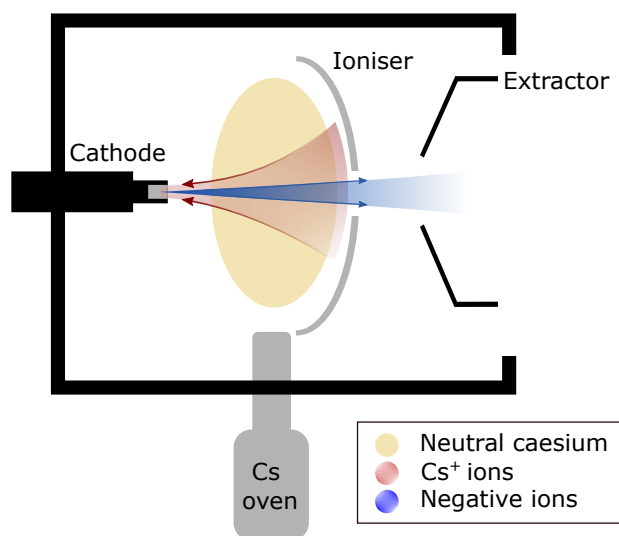
FIGURE 2.12: Schematic view of a caesium sputter source. Caesium vapor is released from an oven and ionised on a heated ioniser. The positive Cs ions are then accelerated onto a cathode where they sputter fragments as negative ions. Subsequently, the negative ions are extracted using the acceleration field.

2.4.3   Creation of negative ions by charge exchange

As an alternative approach, negative ions can be produced by collision of an ion or atom with another ion or molecule. Depending on the kinetic energy, EAs and IPs of the reaction partners, there is a probability of an electron transfer, creating the negative ion. Most commonly, a beam of positive ions is guided into a charge exchange cell containing a vapour of elements with low IP such as alkaline earth metals or alkaline metals. Upon impact, a double exchange of electrons can take place. A practical rule for maximum nega-

tive ion production was derived and tested [97, 113]. This calculation was based on Massey's derivation of a maximum cross section outside an adiabatic regime where the electron transition is unlikely [114]. For high impact energies and assuming that electron transition times are comparable to the collision time, the incident energy E_{max} in keV for maximum negative ion production is given empirically by

$$E_{\text{max}}[\text{keV}] = 8.31 \cdot 10^{-3} m_1[\text{amu}] (a[\text{Å}] \Delta E[\text{eV}])^2 \qquad (2.39)$$

where m_1 is the mass of the incident particle (in atomic mass units), a the distance of the interaction (in Angstrom) and $\Delta E = \text{EA} - \text{IP}$ the difference between electron affinity of the incident particle and the ionisation potential of the electron donor (in eV). Experimentally, charge exchange efficiencies of up to 90 % for chlorine were found using sodium and magnesium vapour and incident energies between 10 keV and 90 keV [115, 60].

Charge exchange ionisation can be especially useful for elements which can not be produced efficiently directly as negative ions, but in contrast as positive ions which are then guided into a charge exchange cell. One application of this is the production of radioisotopes such as astatine and polonium, where experiments using a charge exchange cell for negative ionisation and subsequent determination of the EA were proposed at ISOLDE [116]. First studies of the production of polonium using charge exchange are expected to take place in 2021 (see letter of intent F as well as minutes of the INTC [117]).

Chapter 3

Radioactive ion beams

3.1 Production of radioactive ion beams

The phenomenon of radioactivity was first discovered by Henry Becquerel in 1896 when he found that a photoplate was dimmed when a uranium salt was placed on top [118]. This subsequently also lead to the discovery of isotopes [119, 120], atoms with the same proton number Z, but different mass number A due to a different amount of neutrons in the nucleus.

A commonly used graphical depiction of the elements and their isotopes is the *table of nuclides* [121], shown in Figure 3.1, where each block corresponds to an isotope with atomic number Z and mass number A, denoted as $^{A}_{Z}E$, with element symbol E as a one or two letter code. The x-axis represents the number of neutrons, the y-axis the number of protons, i.e. the atomic number Z, of an isotope. The study of radioactive isotopes has become an important part of fundamental research fostering numerous fields of nuclear physics and astrophysics. Further, radioactive isotopes are commonly used as resources in solid state physics, for diagnostic or cancer therapy in nuclear medicine [122] and additionally as fuel in nuclear power plants [123] or for military purposes [124].

Although some of the few radioactive elements like uranium and thorium have longest lived isotopes which are naturally occurring in reasonable quantities, the vast majority of shorter lived isotopes has to be created artificially in nuclear reactors or accelerator facilities in order to obtain sufficient amounts for experimental investigation. Particularly suitable for short-lived

isotopes, is the extraction of radioisostopes in form of radioactive ion beams (RIBs), which can be easily directed towards experimental stations immediately after creation.
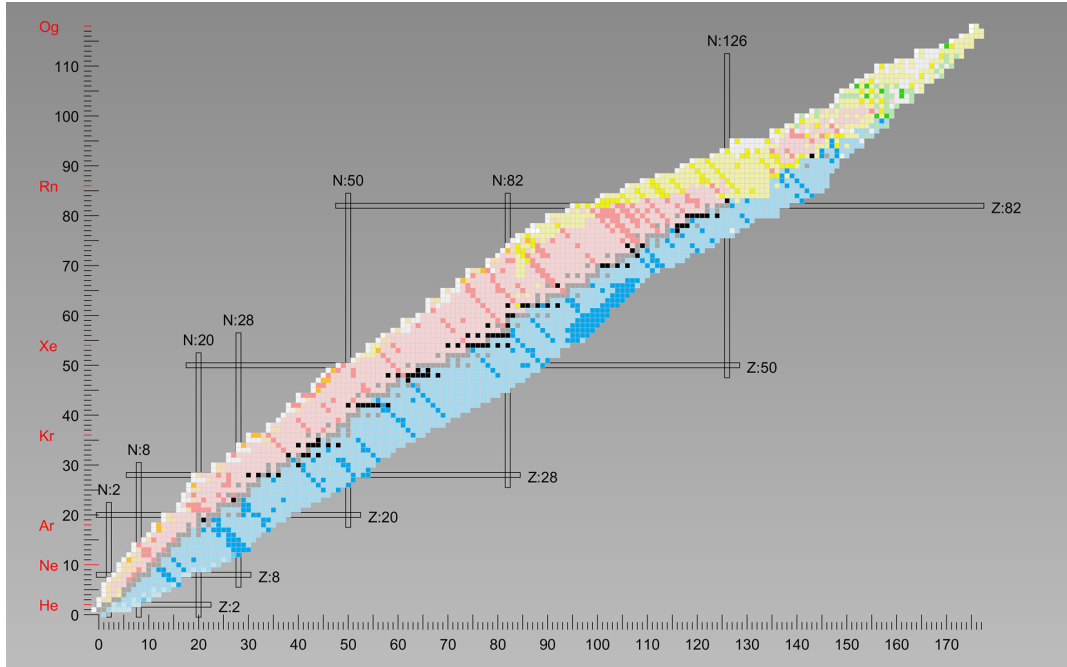
FIGURE 3.1: The chart of nuclides, where the x-axis indicates the number of neutrons (Z) and y-axis the number of protons in a nucleus. Stable nuclei are shown in black, blue indicates nuclei mainly decaying via β^- and red via β^+ decay. Yellow indicates α decaying nuclei and green spontaneous fission. Image by Z. Sóti et al. [121], under Creative Commons Attribution License CC BY 4.0.

Radioactive isotopes as the constituents of RIBs are produced by the collision of a high energetic beam of primary particles with a target, inducing nuclear reactions, some of which are shown in Figure 3.2, to produce a large variety of radioisotopes.

- **Spallation** is the dominant process for primary beams with an energy of above 50 MeV-100 MeV [125]. The impacting particle creates an intranuclear cascade in the target, resulting in a few protons and neutrons being ejected, while leaving the residual nucleus in an excited state [125]. Subsequently, the excited nucleus releases its energy by evaporating more nucleons from the core, ultimately creating a residual nucleus typically 10 u to 20 u lighter than the original [126].

- **Fragmentation** primarily produces lighter elements $6 < A < 40$ by either impinging a heavy primary beam onto a light target or vice versa [127]. The cross section for fragmentation is small for low energy primary beams and increases up to a kinetic energy of $10\,\text{GeV}$, where it stabilizes [127].
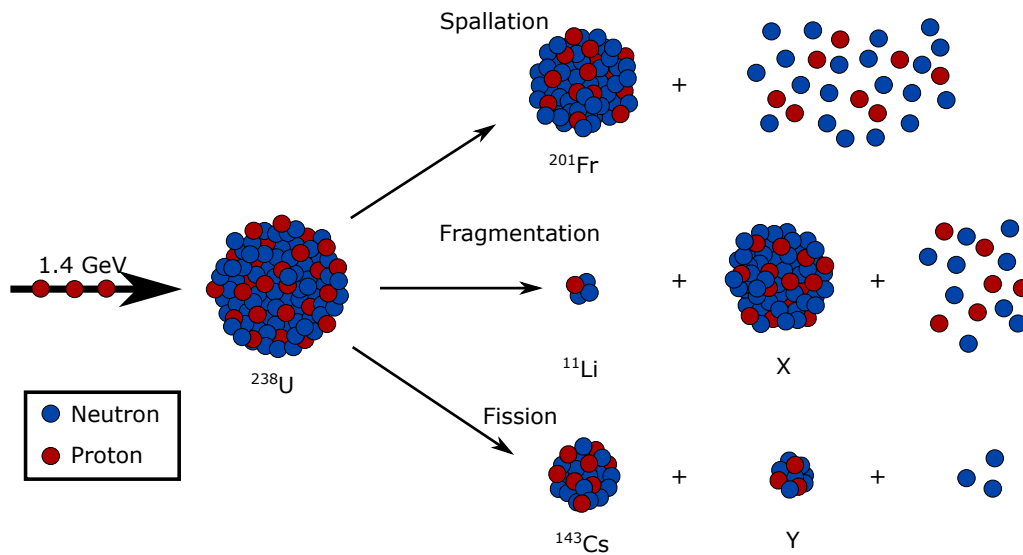
FIGURE 3.2: Nuclear reactions induced in ^{238}U by collision with a $1.4\,\text{GeV}$ proton beam causing fission, fragmentation and spallation reactions.

- **Fission** can occur when the primary particle is absorbed by the target nucleus. As a result, a fissile nucleus in an unstable excited state could be formed, which subsequently releases its excess energy by splitting into typically two heavy fission fragments with additional emission of typically some neutrons and possibly other light particles [128]. Most commonly, fission is known as the underlying process used in nuclear power plants. Here, the energy released by the fission of typically a fissile uranium or plutonium isotope by thermal neutrons is used to produce thermal energy which is converted to electric power by heating a cooling agent which in turn drives turbines [129].

- In **Fusion evaporation** reactions, the primary particle and the target nucleus fuse into one compound system, which subsequently releases energy via evaporating neutrons and gamma rays [126].

There are two common production methods employing the various reactions for RIB production, the *in-flight separation* and the *Isotope Separation OnLine (ISOL)* method, shown in Figure 3.3. The in-flight separation method
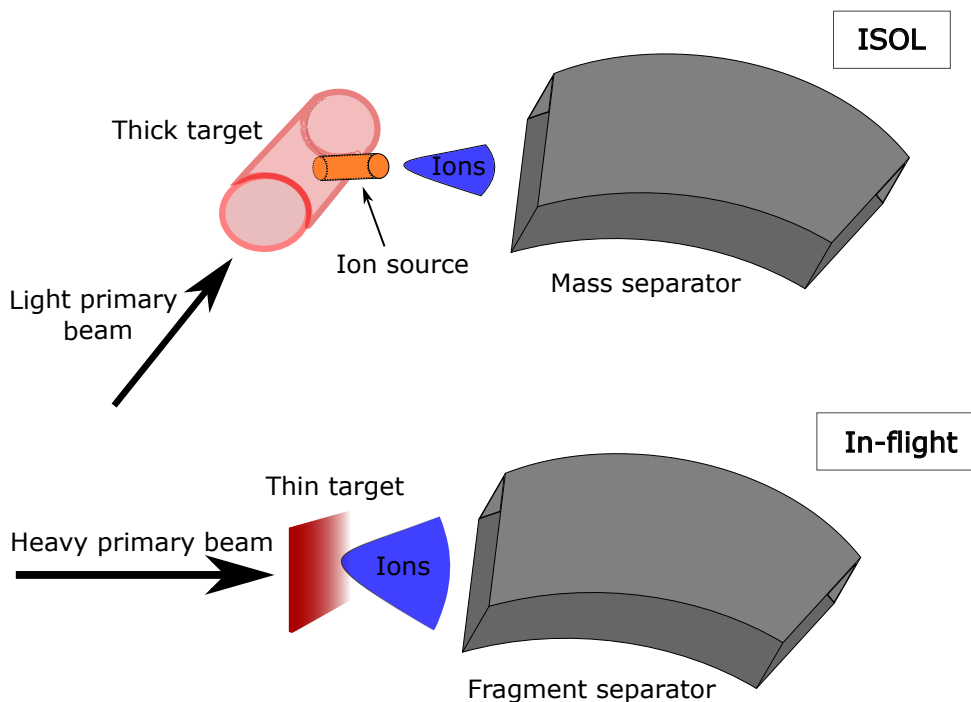
FIGURE 3.3: Comparison of the in- flight and ISOL production method. For ISOL, a light primary beam impinges on a hot, thick target. Radioisotopes then effuse into an ion source, where they are ionised and extracted. The in-flight method utilises a heavy primary beam impinging on a thin target made of a light element, producing a variety of recoil fragments, which are subsequently mass separated.

uses a primary beam of heavy ions colliding with a thin target consisting of light elements such as graphite or beryllium [130]. The heavy ions collide with the target, inducing mainly fragmentation and fusion-evaporation reactions. The resulting reaction products then recoil out of the target with charge and approximately the same energy and direction as the incident beam and are subsequently mass separated and guided towards experimental stations. The in-flight technique has the two advantages that shorter-lived elements down to half-lives of a few µs can be produced and that their release is independent from their chemical properties [131]. Additionally, there is no need

of re-acceleration, since the fragments retain most of their kinetic energy and direction [131]. However, this also results in a larg emittance and low intensity of the extracted RIB, in particular in comparison to the ISOL method, due to the recoil moments and angular distribution of fragments from the target.

The ISOL method, first demonstrated in 1951 [132], uses a thick, hot target, bombarded with a light primary beam, inducing fission, spallation and fragmentation. Resulting radioisotopes diffuse out of the target material and effuse into an ion source, where they are ionised and subsequently accelerated into a beam-line.

The diffusion process is facilitated by keeping the system at high temperatures, thereby also reducing condensation and sticking times on surfaces. Nevertheless, due to the comparatively slow extraction from the target, the ISOL method can only produce elements with half-lives in the order of ms or longer [131]. However, in return, the particle yield and the beam-quality regarding emittance and energy distribution is significantly higher than in the in-flight technique due to the high number of target nuclei contained in a thick target interaction volume as well as the the dedicated target ion source configuration which can be optimised for the element of interest.

An overview of the different ISOL and in-flight facilities worldwide can be found in articles by Blumenfeld *et al.* [130] and Lindroos [133].

3.2   Ion beam manipulation

In the following, a brief overview of ion beam manipulation and characterisation methods as well as mass separating techniques is given. In depth discussion of these topics is found in textbooks and reviews such as by Hellborg [134], Szilagyi [135], Reiser [136] and Dahl [137].

3.2.1   Emittance

Rather than solving the equations of motion for individual particles of an ion beam, the particle ensemble can be characterised by its **emittance** ϵ, i.e. the

volume in six-dimensional phase space, which is occupied by the beam particles [136, 138]. If the coupling between the three spatial directions is weak, the emittance can be further divided into the transverse and the longitudinal emittance. The longitudinal emittance describes the distribution of energy and phase along the direction of travel (conventionally chosen to be the z-axis) of the beam which is especially relevant when using bunched beams. The transverse emittance describes the spread in space and momentum in x and y.

According to Liouville's theorem, the emittance of a beam is constant under the influence of conservative forces [139, 134]. However, the emittance of an ion beam is changed by deceleration or acceleration, where deceleration increases and acceleration decreases the emittance.

Often times, the trace space with the relative velocity, e.g. $v_{\text{rel},x} = \frac{v_x}{v_z} \approx \theta$, or the angle θ is used instead of the momentum. The transverse emittance can then be defined as the area A of an ellipsoid enclosing the ions in e.g. $(x, v_{\text{rel},x})$-phase space as shown in Figure 3.4.
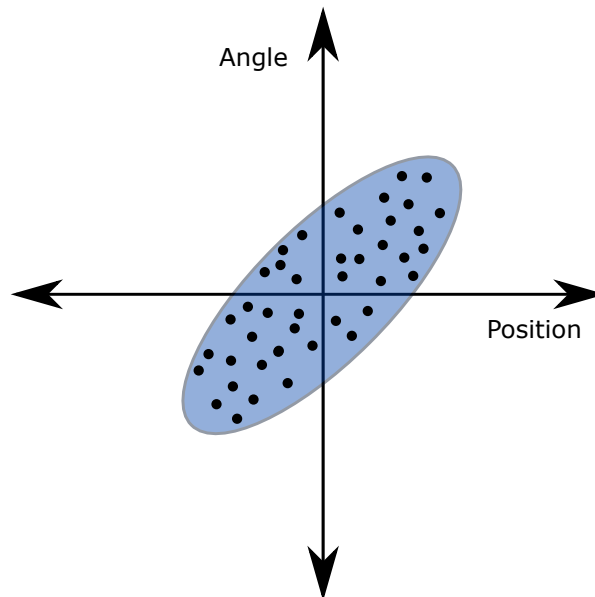
FIGURE 3.4: Transverse emittance. The ions in black are distributed over the trace space, while the beam emittance is shown by the ellipsoid envelope.

The transverse emittance is then given by

$$\epsilon = \frac{A}{\pi} = \gamma_C x^2 + 2\alpha_C x v_{\mathrm{rel},x} + \beta_C v_{\mathrm{rel},x}^2, \tag{3.1}$$

where α_C, β_C and γ_C are the "Twiss" or "Courant-Snyder" parameters determining shape and orientation of the ellipse, and

$$\beta_C \gamma_C - 1 = \alpha_C^2. \tag{3.2}$$

However, for real particle distributions it is difficult to define the boundary of the beam, which is why the emittance ellipse is often defined by an envelope incorporating a certain percentage of particles. For example ϵ_{95} includes 95 % of the ions.

Another frequently used definition of the emittance is the root-mean-square (rms) emittance, based on the statistical distribution of the particles. The rms emittance is defined as

$$\epsilon_{\mathrm{rms},x} = \sqrt{< x^2 >< v_{\mathrm{rel},x}^2 > - < x v_{\mathrm{rel},x} >^2}, \tag{3.3}$$

where $< x^2 >$, $< v_{\mathrm{rel},x}^2 >$ are the variance of the position and angle, respectively and $< x v_{\mathrm{rel},x} >$ the correlation between angle and position in the beam. The emittance is usually given in units of π mm rad, however some authors omit the factor π or instead include it in the numerical value of the emittance.

3.2.2   Ion beam optics

In order to extract an ion beam from a source and change its trajectory or shape, various ion optical elements are commonly used, some of which are briefly described in the following.

Generally, ion optical elements utilise the Lorentz force $\vec{F}_L = q\vec{E} + q\vec{v} \times \vec{B}$ by applying an electric or magnetic field on the ion beam during passage in order to focus or deflect it. For a high energy beam in an accelerator such

as the LHC, where the beam velocity is close to the speed of light, magnetic fields from supraconducting dipole, quadrupole or higher order multipole magnets are used to capitalize on the scaling of the magnetic part of the Lorentz force with the speed of light, resulting in higher practically achievable magnetic field strengths than with an conventionally generated electrostatic field.

In order to extract an ion beam from a source, an electrostatic potential between source and an extraction electrode in the order of 10 keV to 100 keV is used. To further accelerate an ion beam up to beam energies of hundreds of kilovolts and far beyond, pulsed electric fields are usually employed.

In a linear accelerator for example, an ion bunch travels through a series of electrodes, to which an AC field is applied. The frequency of the field and in most cases also the length of each electrode is adjusted, so that ions are attracted towards it when approaching and repelled from it upon exiting.

In order to steer an ion beam into a certain direction, an electric dipole, such as generated within two opposing metal plates as shown in Figure 3.5 a) can be used.
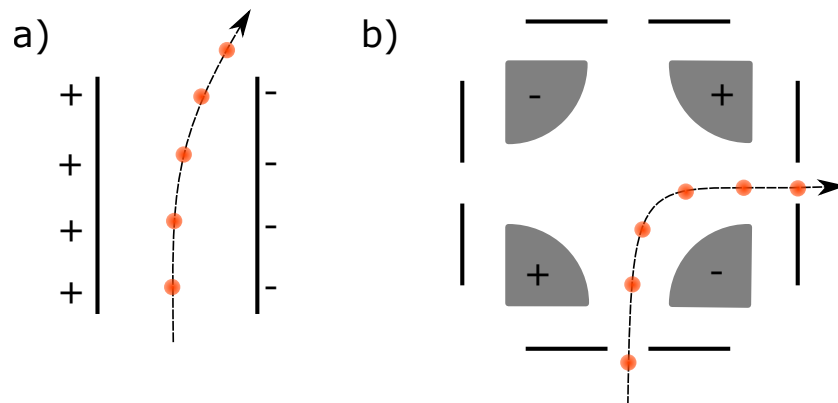
FIGURE 3.5: Electrostatic beam deflection using a) an electrostatic steerer and b) a quadrupole deflector.

Here, a static electric field is applied between the plates, deflecting ions according to the field direction and strength. For beam energies greater than 100 keV, magnetic dipoles are used, utilising the aforementioned scaling of the magnetic part of the Lorentz force with the speed of light [134].

In addition, also electrostatic quadrupole fields can be used in ion beam optics. One possible application is an electrostatic quadrupole deflector as shown in Figure 3.5 b) which can be used to bend ions by 90°, enabling beam transport in 3 directions by simply switching potentials.

Electric or magnetic quadrupoles can also be used to focus the beam in one transverse direction, while defocussing in the other. Hence, quadrupole duplets or triplets are employed for beam focussing in both transverse directions using the principle of strong focusing, also called alternative gradient focussing [140]. In order to correct for higher order perturbations, storage rings and accelerators additionally employ higher order multipoles such as electrostatic or magnetic octupoles.

For beams with energies up to tens of keV in most cases simple electrostatic Einzel lenses are used [134]. An Einzel lens typically consists of three cylindrical ring (or aperture) electrodes (for circularly shaped beams) as shown in Figure 3.6, two of which are typically on the beamline potential (i.e. ground) while the center electrode is put on a static potential.
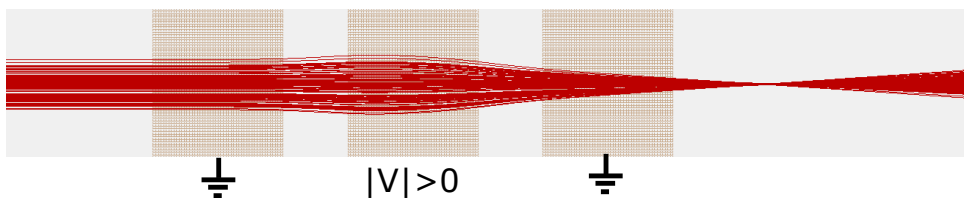
FIGURE 3.6: Schematic view of an Einzel lens. An ion beam (red) entering the lens is deflected by the potential between the grounded outer electrodes and the center one, leading to a focussing effect.

The resulting electric field then affects the outermost ions the most, pushing them towards the center of the beamline, while ions which are already situated closer to the center are less affected, resulting in a focusing of the beam. An Einzel lens can be used in both accelerating and decelerating configuration, where the potential on the central electrode is attracting or repulsing respectively. However, the refractive power is greater for the decelerating configuration, requiring a lower voltage than the accelerating one to achieve the same refractive power.

3.2.3   Mass separation

In order to investigate a specific element or isotope, in most of the cases it is desirable to separate them from the other constituents of the initial ion beam. This can be achieved via mass separation.

Dipole mass separating magnets

One of the most common ways to separate an ion beam by mass is by using an electromagnetic mass separator. Here, the ions are sent into a dipole magnet as shown in Fig 3.7. In the magnetic field of the separator, the ions are forced into a circular motion, where the radius r can be derived from the equilibrium of the Lorentz and the centrifugal forces:

$$F_{\text{L}} = F_{\text{centrifugal}} \Leftrightarrow qv \cdot B = \frac{mv^2}{r}, \tag{3.4}$$

where B is the magnetic dipole field and q, v, m the ions charge, velocity and mass respectively. From Eq. 3.4 follows

$$r = \frac{m}{q} \cdot \frac{v}{B}. \tag{3.5}$$

If all the ions originate from the same source, they are accelerated by the same potential U. Eq. (3.5) can then be written as

$$r = \frac{\sqrt{2meU}}{Bq}. \tag{3.6}$$

Consequently, ions with different mass to charge ratios $\frac{m}{q}$ travel on separate trajectories within the dipole magnet. By placing an aperture at the exit focal point of the separator magnet, the mass to charge ratio of the passing ions can then be chosen by varying the magnetic field accordingly. Mass separating magnets have the advantage of being reliable and stable in operation conditions, while covering a large mass range or, respectively, a broad range of beam energies by adjusting the field strengths. However, the mass resolution of magnetic sector fields mass spectrometers, defined as $\frac{m}{\Delta m}$, where

Δm is the full width half maximum of the mass peak, is limited due to the energy distribution of the ion source and possible imperfections in the magnetic field distribution (fringing fields, inhomogenities) and usually does not permit e.g. the separation of isobars. In particular for highly intense beams, space charge effects come into play in addition to image aberrations of the ion optical system. In all cases, gaskinetical collisions with residual gas constituents have to be considered too [141].
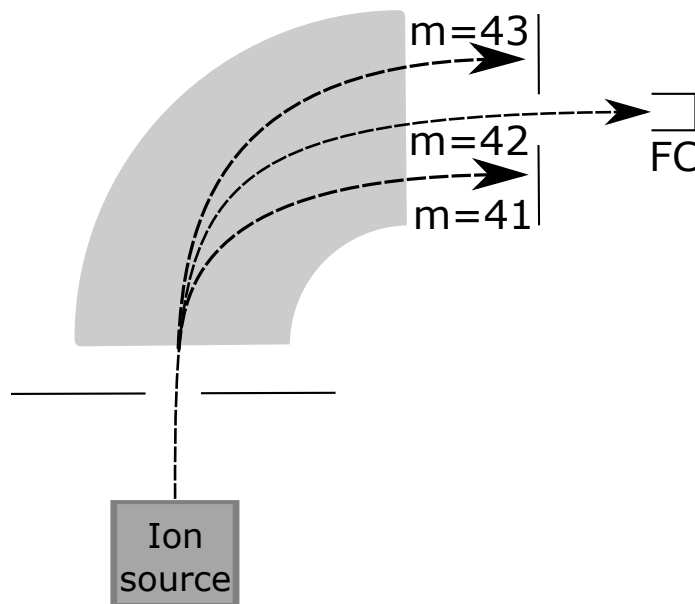
FIGURE 3.7: Schematic of the working principle of a mass separating magnet. Ions with the chosen mass to charge ratio exit the magnet, while all others are blocked by a slit system.

Quadrupole mass filter

A quadrupole mass filter (QMF), employs a high frequency oscillating electric quadrupole field superimposed to a DC field to achieve mass separation. A QMF consists of a geometry of two opposing pairs of rods, generating the quadrupole field as shown in Figure 3.8. The radio-frequency voltage and a DC offset is applied on each pair with a 90° phase shift, given by

$$U_{QMF}(t) = U_{DC} + U_{AC} \cdot \sin(\omega t). \tag{3.7}$$

The potential between quadrupole rods with distance $2r_0$ is given by

$$\Phi_{\text{QMF}}(\vec{r}, t) = (U_{\text{DC}} + U_{\text{AC}} \cdot \sin(\omega t)) \cdot \frac{(x^2 - z^2)}{r_0^2}. \tag{3.8}$$

The movement of an ion in this potential can be determined by

$$m \frac{d^2}{dt^2}\vec{r} + e \nabla \Phi_{\text{QMF}}(\vec{r}, t) = 0. \tag{3.9}$$

By introducing the dimensionless parameters $a_x = -a_y = \frac{8eU_{\text{DC}}}{mr_0^2\omega^2}$ and $q_x = -q_y = \frac{4eU_{\text{AC}}}{mr_0^2\omega^2}$, Eq.(3.9) can be transformed into a Mathieu's differential equation, which can be solved analytically, leading to two sets of solutions [142].

Stable solutions describe particles which follow a periodic oscillating trajectory in x and y, while unstable solutions describe particles which follow an oscillating trajectory with exponentially increasing amplitude, resulting in the particle impinging on the quadrupole rods. Whether or not an ion moves on a stable trajectory only depends on the parameters q and a, which contain the mass. The detailed display and discussion of the solutions of the Mathieu differential equation and the description of the resulting parameter range for a QMF are given elsewhere [142, 143]. The theoretical mass resolution of a QMF can be approximated by [144]

$$\frac{m}{\Delta m} \approx \frac{0.126}{0.16784 - \frac{U_{\text{DC}}}{U_{\text{AC}}}}. \tag{3.10}$$

However, in order to achieve this value or high resolution in general, the ions have to undergo a sufficiently high number of oscillations N within the longitudinally limited quadrupole field [143]

$$\left(\frac{m}{\Delta m}\right)_{\text{max}} \approx \frac{N^2}{12.25}, \tag{3.11}$$

In addition, this leads to an upper energy limit E_{max} for the ions:

$$E_{\text{max}}[\text{eV}] = \frac{0.0426L[\text{cm}]^2 \nu[\text{MHz}]^2 m[\text{amu}]}{\frac{m}{\Delta m}}, \tag{3.12}$$

where L is the length of the QMF in cm and ν is the frequency in MHz. Due to this energy dependence, either the length of the device has to be adjusted to the expected ion energy, or the ions need to be decelerated before entering the QMF, which can lead to significant losses in beam intensity due to the increase in beam emittance.
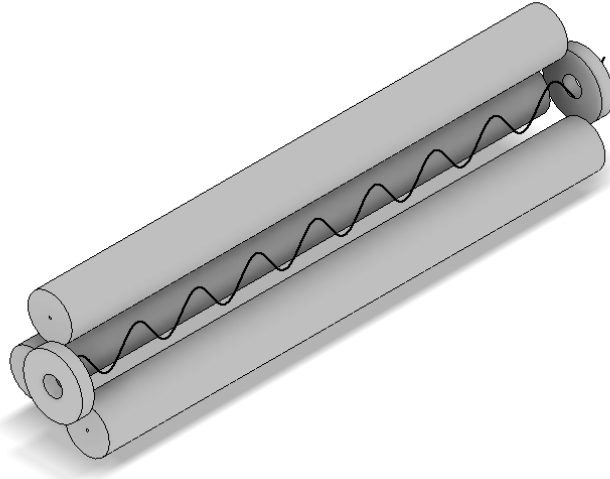
FIGURE 3.8: Three quarter view of a quadrupole mass filter (one rod removed) with entrance and exit apertures and a stable sinusoidal ion trajectory in one direction shown in black.

In addition, due to the motion of the ions in the radio-frequency field and depending on the injection conditions, the ion beam diverges in the fringe fields at the exit of the QMF, which can lead to additional losses or distorted mass peak shapes [143]. However, this effect can be mitigated by appropriate ion guides and by proper clipping of the fringe field at the exit of the mass filter [145].

Time of flight

Time of flight mass separation utilises that ions with different masses but the same kinetic energy will have different velocities: If all ions are accelerated by the same potential, their kinetic energy is classically given by

$$E = q \cdot U = \frac{1}{2}mv^2. \tag{3.13}$$

Hence, two ions with the same charge but different masses will have different velocities. If those ions drift over a sufficient long path length, they will separate in distance. By a time-resolved detection or, alternatively, by adjusting e.g. a blocking voltage for some respective arrival times, ions of different masses can be separated. However, depending on the mass difference and kinetic energy, the flight path to separate ions with sufficient precision can be impractical. Consequently, this method can be optimized by trapping the ions between a set of mirror electrodes, essentially extending the flight path with the number of revolutions. Such an arrangement is called Multi-reflection time of flight (MR-ToF) device, and is discussed in more detail in chapter 4.

3.2.4   Beam diagnostics

In order to gain insight into the properties of an ion beam such as its intensity, beam envelope, spatial position or temporal structure, several different detecting devices can be employed.

Faraday cups (FCs) are simple metallic cups into which the ion beam is directed to measure its intensity. The charged particles impinging on the metal cup create a charge transfer which can be measured as an electric current with a sensitive amperemeter. Secondary electrons created by the impact of a beam of a few keV or more are usually suppressed by a biasing voltage of typically e.g. $-40\,\mathrm{V}$ at the entrance of the FC. FCs can measure beam intensities in the order of pA and higher. In addition, an upper limit in terms of beam intensity is given by the ability of the FC to absorb the power deposition of an ion beam without e.g. melting.

More sensitive devices with capability to count single ions usually employ a form of electron multiplication. Here, the ion beam is directed onto a dynode, creating secondary electrons by impact, which are subsequently multiplied by directing them to impact on another dynode held on a higher, positive voltage. This can be repeated multiple times until the electron pulse is amplified enough to be measured by conventional electronics. Detectors

employing this kind of detection scheme and used within the frame of this thesis are channel electron multipliers (CEMs), MagneToFs and micro channel plates (MCPs). MCPs have the additional advantage of achieving a spatial resolution by utilising plates with multiple channels in which the electron multiplication takes places. For radioactive ion beams, decay spectroscopy, utilising the specific decay channel of an element, can be used with the advantage of additional identification of the detected species by its characteristic ejectiles.

For the determination of the beam envelope or beam shape, wire scanners or wiregrids are typically employed. In a wire scanner, a thin wire is moved through the beam, which results in an electric current loaded onto the wire. By measuring the current against the position of the wire, the transversal beam profile can be extracted. An in-depth overview of beam instrumentation and diagnostics is given in textbooks and reviews such as by Strehl [146] and Forck [147].

3.3 ISOLDE

The **I**sotope **S**eparator **O**n **L**ine **DE**vice (ISOLDE) is a radioactive ion beam facility at the European Center for Nuclear Research (CERN in Geneva, Switzerland), producing a large variety of radioactive ion beams by application of the ISOL method. Situated within CERN's accelerator complex (shown in Figure 3.9), it is one of the major ISOL-type facilities worldwide. Here, over 1000 radioactive isotopes from 72 different chemical elements have been produced up to today by irradiation of a thick target with a 1.4 GeV proton beam. Intensities of up to 2 μA were delivered by the Proton Synchrotron Booster (PSB) [56].

Initially, the first version of ISOLDE came into operation in 1967 and received 600 MeV protons from the Proton Synchlocyclotron [130]. After several upgrades during the following decades, ISOLDE was moved to connect to the PSB in the 1990s, now able to accept protons of 1.4 GeV kinetic energy and with an intensity of up to 2 μA [148, 149]. In the early 2000s, a linear

accelerator (LINAC) was added to the ISOLDE facility to enable post acceleration of the low energy beams from the ISOLDE RIB machines.
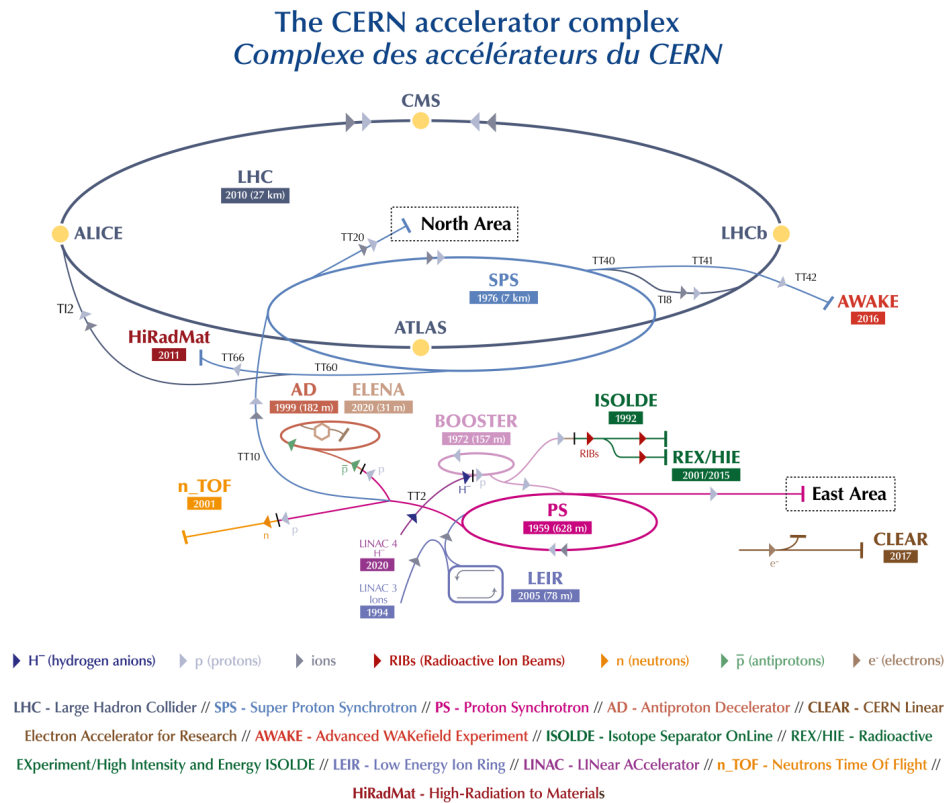
FIGURE 3.9: The accelerator complex of CERN; negative hydrogen ions are produced in LINAC4, subsequently injected into the PS booster where electrons are stripped off. From the PSB, the remaining protons are distributed further down the accelerator chain to fixed target experiments as well ultimately to the LHC. The ISOLDE facility is connected to and receives protons from the PSB. Illustration from [150].

The first stage, called REX was operational in 2001, generating post accelerated beams of energies of up to 3 MeV/u [151, 152]. The second high-energy upgrade, called HIE-ISOLDE, added superconducting LINAC modules to REX, enabling operation with beam energies of up to 5.5 MeV/u with possibilities to increase up to 10 MeV/u [153, 154].

With the ongoing work on the entire CERN-accelerator chain for the high luminosity upgrade of the LHC, proton beam energies up to 2 GeV and intensities up to 4 μA will become feasible at ISOLDE in the future, when the

infrastructure such as beamdumps and proton delivery line have been upgraded accordingly.

In addition, the **MED**ical **I**sotopes **C**ollected from **IS**OLDE (MEDICIS) facility was initiated in 2010 and has been running since 2017 [155]. Here, a rail system is employed to position a second nuclear reaction target behind the irradiation station of the high resolution separator (HRS) stage of ISOLDE, parasitically taking advantage of those protons which have not interacted with the primary ISOLDE target material. The irradiated target is then removed and connected to a the MEDICIS mass separator, where radioactive elements relevant for medical research are extracted as an ion beam, purified by laser ionisation and mass separation and implanted onto a foil.

On top of that, MEDICIS receives external radioactive sources for processing, enabling the facility to stay active even when the CERN accelerator chain is in a shutdown period. Such samples are shipped to external researchers and collaborators. In 2019, the MEDICIS laser ion source, called MELISSA, was comissioned, introducing highest isobaric selectivity through laser resonance ionization into the production of medical radioisotopes [156].

The ISOLDE experimental hall and adjacent laboratories are shown in Figure 3.10. In the highly radioactive "target area", the proton beam is sent to either of two different target stations or "Frontends", GPS and HRS, named after the subsequent electromagnetic separators, the General Purpose Separator (GPS) and the High Resolution Separator (HRS). From both target stations, RIBs can be extracted with up to 60 keV kinetic energy. Adjacent to the target area are the MEDICIS facility as well as the Class A laboratory, where radioactive target materials are stored and handled. Following the respective target stations, the ion beam is guided through an electromagnetic mass separator.

The GPS magnet has a mass resolving power $m/\Delta m$ of 800 and is connected to an electrostatic switch-yard, making it possible to deliver beams in the range of $\pm 13\%$ of the central mass quasi- simultaneously to three different beam-lines. The central mass is delivered to the main beamline connected to all experiments in the experimental hall, while slightly lower or higher mass

are directed to the General Low Mass (GLM) and the General High Mass (GHM) beamlines respectively, where travelling setups can be installed [56].
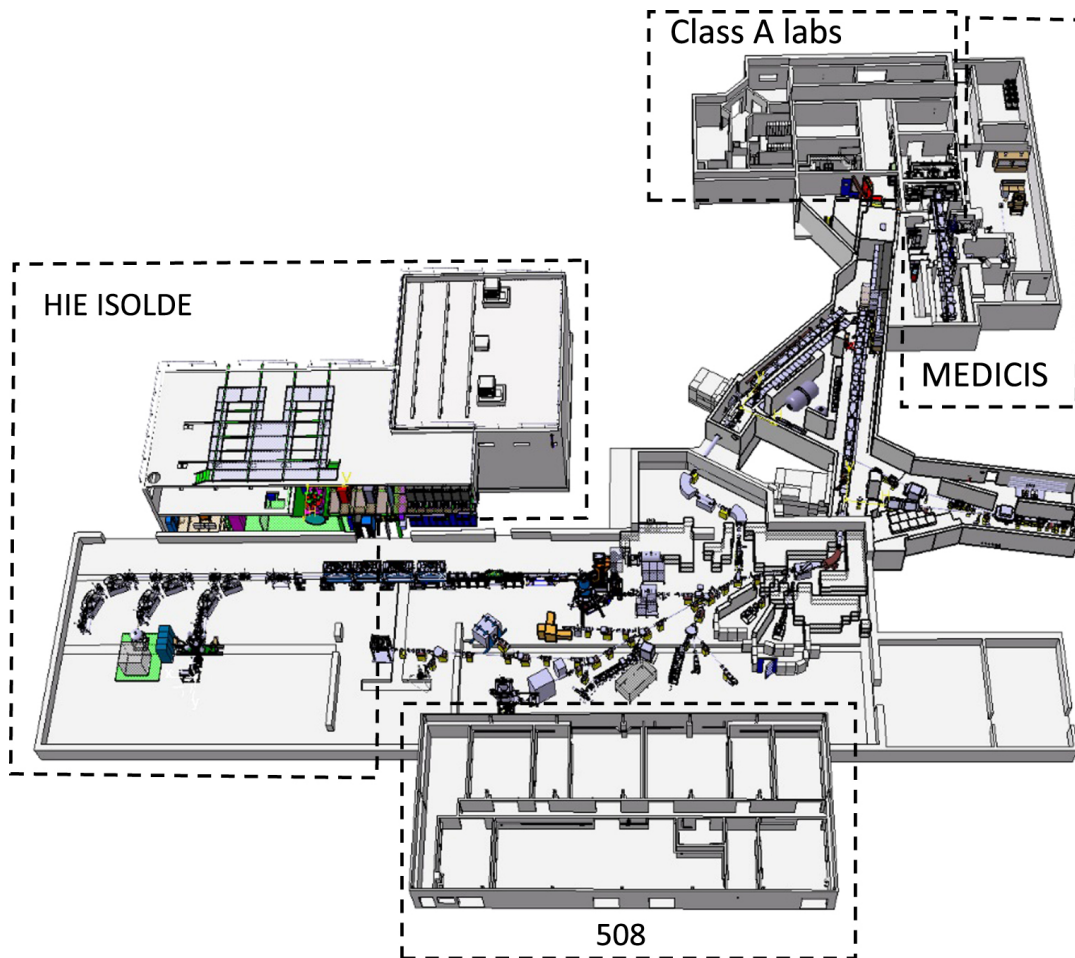
FIGURE 3.10: The ISOLDE facility. On the upper right the medical facility MEDICIS is located next to the Class A laboratory where radioactive targets are prepared or inspected. A rail system connects the MEDICIS separator Frontend to the highly shielded target area, with the GPS and HRS target station. From there, both separators transport radioactive ion beams into the low energy sector of the experimental hall, which was extended to include the post acceleration beamlines of HIE-ISOLDE. Located above the experimental hall is building 508, which encompasses the ISOLDE control room as well as several offices and laboratories for permanent experiments. Image by R. Catherall et al. [56], under Creative Commons Attribution License CC BY 3.0.

HRS is equipped with two mass separating magnets, resulting in a higher mass resolving power of about 6000 [56]. Following the HRS mass separator, a radio frequency cooler-buncher (RFQcb) called ISCOOL [157, 158] is

connected, enabling cooling and bunching of the ion beam, which is highly beneficial for many high-sensitivity spectroscopy experiments.

3.3.1 ISOLDE target Unit

The ISOLDE target and ion source unit, referred to as the target unit and shown in Figure 3.11, is an aluminium vacuum vessel in which the generation and ionisation of the radioisotopes takes place. It generally comprises of a target container, a transfer line, an ion source and necessary feedthroughs for electrical connections, cooling water and gas injection, if needed.
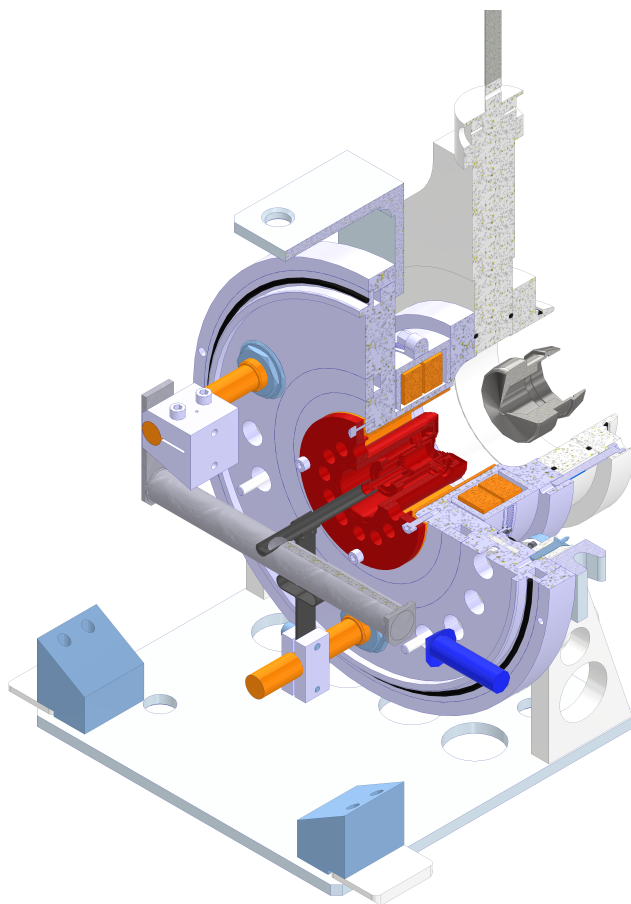
FIGURE 3.11: ISOLDE target unit. Protons (blue arrow) impinge on the target container (light grey) filled with the target material. The created radioisotopes diffuse through the transfer line (dark grey) into the ion source (central cylinder of the red part), where they are ionised and subsequently extracted with an extraction electrode (shiny grey) by a potential difference up to 60 keV.

The **target container** is a 20 cm long tantalum tube with 2 cm inner diameter, filled with the target material, which is irradiated by the proton beam originating from the PSB. Recently, an enlarged target container with 50 mm inner diameter was designed, to suit the needs of the MEDICIS facility and for application at a new proton to neutron converter target type [159].

In contrast to direct bombardment of the target material with protons, the target can be equipped with a proton to neutron converter. Here, the proton beam is directed onto a solid tungsten rod with a length of 125 mm and a diameter of 12 mm instead, creating a shower of neutrons which impinge e.g. upon an actinide target, producing neutron-rich fission fragments [160, 159]. Originally, the tungsten rod was mounted underneath the target container. However, a new design was developed recently [159], placing the tungsten rod within the large target container and surrounding it with the target material. In order to extract the isotopes of interest from the target container, a small tube referred to as **transfer line** is welded to the target container, connecting the target container to the ion source. The transfer line is typically made out of tantalum, but different materials can be chosen, e.g. in order to chemically select isotopes passing into the ion source.

The target container, the transfer line and the ion source are resistive heated individually to typically around 2000 °C and up to 2400 °C, depending on the characteristics of the target material and ion source type. This ensures fast diffusion out of the target material and reduces transport times to the ion source by minimising wall sticking times. As an example visualising the variety of target materials used in ISOLDE, Figure 3.12 shows the target materials used in 2017.

In general, about half of the targets used are based on carbide compounds (UC_x, SiC and multi wall carbon nanotubes (MWCNT)), but also oxide materials such as ZrO and CaO are frequently used as well as metal targets made out of e.g. Ta or Ti foils. In addition, among other, liquid target materials such as molten Pb are available. An in-depth review of target materials used for ISOL facilities such as ISOLDE can be found in articles e.g. by T. Stora [161], U. Köster [162] and the thesis of J.P. Ramos [163].
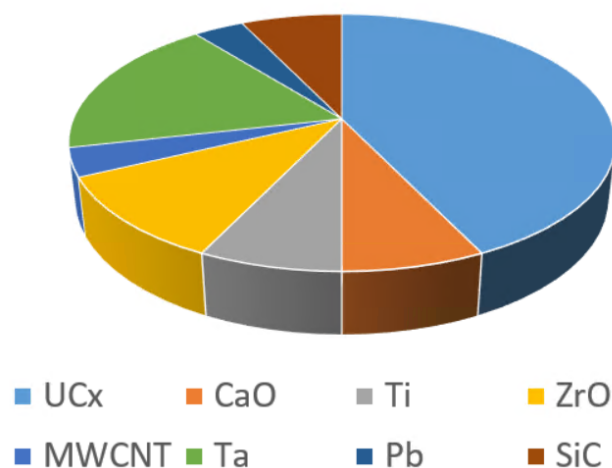
FIGURE 3.12: ISOLDE target materials used in 2017.

Due to the high requirements in regards to low chemical reactivity and mechanical stability under radiation as well as high temperature distress, the target container, transfer line and ion source are mostly manufactured exclusively from refractory metals such as tantalum, molybdenum, tungsten or rhenium.

One of the advantages of the quickly exchangeable and modular ISOLDE target unit compared to other ISOL facilities is its high variability in target material, transfer line and ion source combinations, which enables a multitude of options to optimize beam purity and intensity for a specific experiment.

3.3.2 Ion sources for RIB production

In the following, the different types of ion sources employed at most ISOL-facilities are discussed using the ion sources employed at ISOLDE as example. The three most commonly employed ionisation mechanisms are surface ionisation, laser ionisation or electron impact ionisation, in all cases operated to create predominantly single-charged positive or negative ions. The respective ion sources are required to reliably and efficiently ionise the species of interest while maintaining short ion extraction times to avoid strong decay losses even of short lived species within the target unit itself. In addition,

it is often desired to immediately suppress unwanted isobaric contaminants in the ion source, using chemical properties of the elements or alternatively employing the difference in their ionisation efficiency for a certain ionisation mechanism. In Figure 3.13, all elements which can be produced at ISOLDE with the different ion source types are shown. Elements with low IP ($<6\,$eV) such as the alkali metals can efficiently be ionised positively with a surface ion source, while for elements with higher IPs electron impact ionisation or laser ionisation, if a laser scheme is available, is more suitable. Negative ions of the halogens are usually produced with a negative surface ion source.

FIGURE 3.13: Overview of the chemical elements available as ion beams at ISOLDE and the respective ionisation mechanism. Figure courtesy of J. Ballof.

Positive surface ion source

The underlying principle of surface ionisation was already described in chapter 2. At ISOLDE, surface ionisation is most commonly used for production of positive ions, most efficiently group I elements due to their low IPs. However, in cases where negative ion beams of halogens are of interest, a negative surface ion source with a LaB_6 ioniser is utilised [102].

The positive surface ion source of ISOLDE, shown in Figure 3.14 is a tube of 3 mm inner diameter, about 34 mm length and 0.5 mm wall thickness. This tube is made of a high work function refractory metal, typically tantalum,

tungsten or rhenium, enabling high ionisation efficiencies and mechanical stability at typical operating temperatures of 2000 °C to 2200 °C.

The ionisation efficiency for this geometry has been shown to be underestimated by equation 2.37 due to neglecting multiple wall collisions and mainly due to the electron emission from the hot ion source walls and the thermal plasma well formed that way.
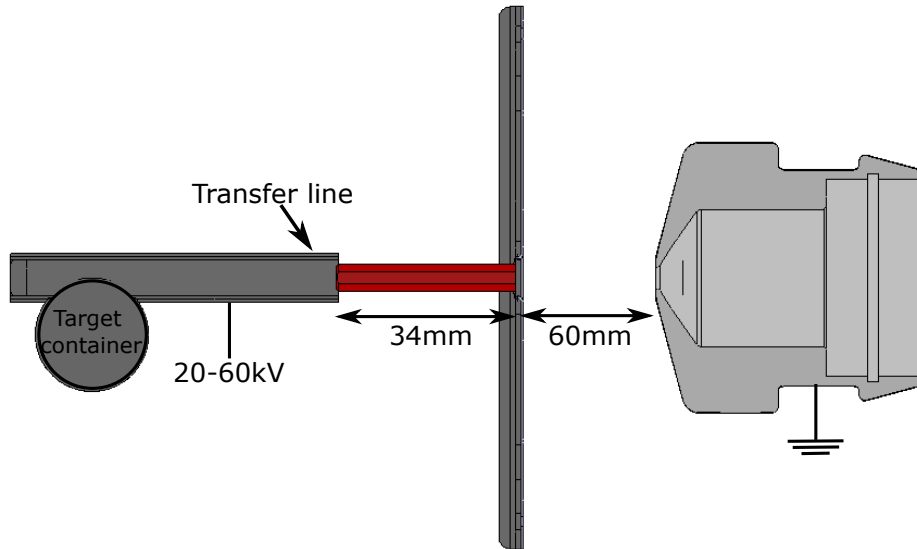
FIGURE 3.14: Positive surface ion source used at ISOLDE. Neutral atoms diffuse out of the target into the hot line, where they are ionised positively on the hot surface (red) and subsequently extracted.

According to the Richardson-Dushman equation [164, 165, 166], a hot surface with a work function Φ will emit electrons with a current density j_e, given by

$$j_e = A_R \cdot T^2 \cdot \exp \frac{-\Phi}{k_B T}, \tag{3.14}$$

where $A_R = b \cdot A_0 = b \cdot \frac{4\pi m_e k_B^2 e}{h^3}$ is the Richardson constant with material-specific correction factor b, T the absolute temperature and k_B the Boltzmann constant. A typical tubular ISOLDE surface source made out of tungsten (Φ =4.54 eV, $A \approx 60$ A/(Kcm)^2) would then emit an electron current of about 2 mA/mm^2 at 2200 °C. These electrons create a transverse plasma potential within the source, shielding ions in part from further wall collisions.

This plasma potential is given by

$$\frac{k_B T}{2e} \cdot \ln\left(\frac{n_{ions}}{n_e}\right),\tag{3.15}$$

where e is the electron charge, n_{ions} and n_e the density of ions and electrons respectively [167]. In addition, the voltage drop of typically about $2\,V$ over the resistive heated source cavity guides the ions towards the extraction region of the ion source. Accounting for this plasma potential and multiple wall collisions, Eq. 2.37 was modified [168, 161] to

$$\epsilon_{is} = \frac{\tau \kappa \alpha}{1 + \tau \kappa \alpha},\tag{3.16}$$

where κ is the number of wall collisions of the atom before extraction and τ the trapping efficiency of the plasma potential in the source.

Surface ion sources generally have the advantage of being mechanically simple and therefore reliable as well as easy to operate. However, the surface source offers very little elemental selectivity and only elements with low ionisation potential, e.g. lower than the work function of the ioniser, are efficiently ionised.

Negative surface ion source

The negative ion source used in ISOLDE is a surface ion source, based on the principle discussed in chapter 2. The basic geometry of the source, depicted in Figure 3.15 is similar to the positive surface ionisation source discussed above, where atoms diffuse into a tantalum transfer tube towards the extraction region of the source, where the ioniser is situated.

The LaB_6 ioniser exhibits a work function of around $2.6\,eV$ and a temperature stability of up to about $1500\,°C$ [59, 100]. LaB_6 is pressed into a pellet which is inserted into the front part of the transfer line by means of a small mounting piece. According to Eq. 2.36, atoms diffusing out of the target onto the pellet can then acquire an electron and are subsequently extracted as negative ions. The low work function of the ioniser also gives rise to a

significant amount of thermally emitted electrons (see Eq. 3.14) which have to be deflected out of the beam to avoid collisional detachment as well as to avoid space charge effects in the extraction of the ions.
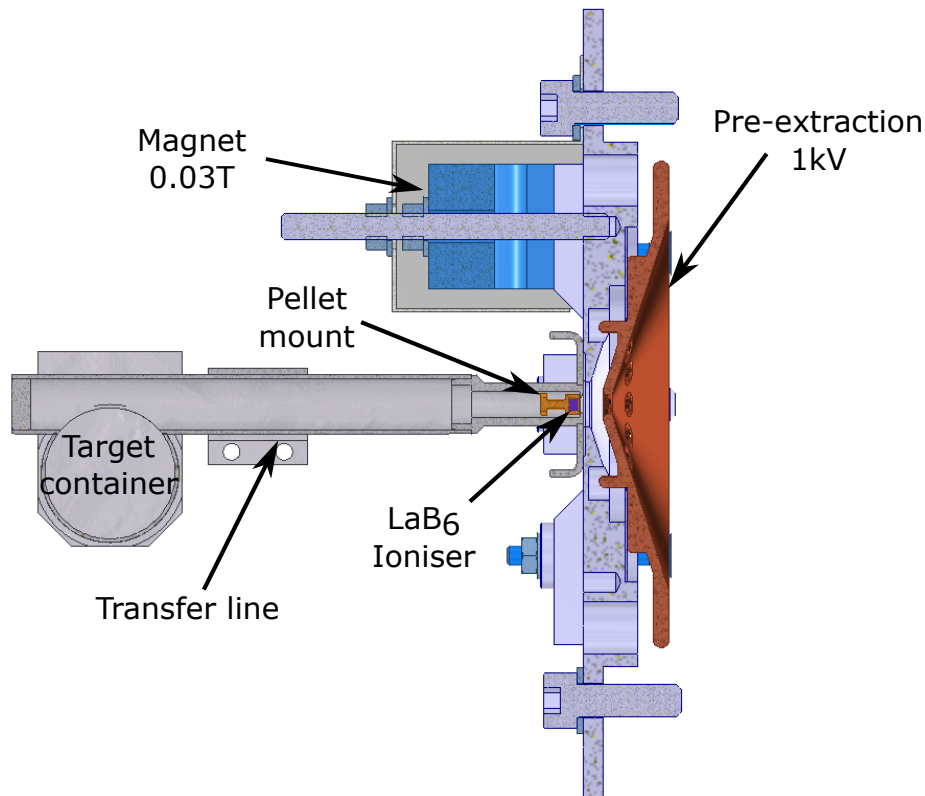
FIGURE 3.15: The negative surface ion source at ISOLDE. Neutral atoms diffuse out of the target container and effuse through the transfer line (both grey) and are ionised in an LaB_6 ioniser (purple) mounted at the end of the transfer line (orange). Electrons emitted from the low work function surface are bend away by a permanent magnet (blue) onto the pre-extraction plate (red-brown), biased with 1 kV.

This is achieved by a small magnetic field of 0.03 T from a permanent magnet mounted on the base plate of the target unit. The magnetic field deflects the electrons onto the pre-extraction plate (also referred to as electron-catcher) which is typically on a 1 kV potential with respect to the ion source. Due to the rather high work function of LaB_6, in particular in comparison to typical EA values, this source is most effective for halogens. In combination with the source geometry this leads to very pure ion beams of good quality. As an alternative to the pellet source, the negative ion source exists also in tubular geometry: Here, a tube with an internal diameter of 3 mm made of

LaB$_6$ or GdB$_6$ is inserted into the transfer line, centered by two rhenium supports. This increases the geometrical likelihood of neutral atoms interacting with the ioniser, but in turn increases the energy spread of the ions and has shown to be less reliable in offline tests [102, 169].

Developments of this source and investigations of different ionisation mechanisms will be discussed in chapter 5.

RILIS

The **R**esonance **I**onisation **L**aser **I**on **S**ource (RILIS) is ISOLDEs laser ion source, schematically shown in Figure 3.16. Here, a singly charged positive ion is created from an atom via step-wise laser excitation of its valence electron into the continuum, a Rydberg state or an auto-ionising state as shown in Figure 3.17. The utilisation of the unique energy levels of an atom in a multi-step laser scheme as shown in Figure 3.17 has the advantage that this ion source exhibits highest element selectivity.
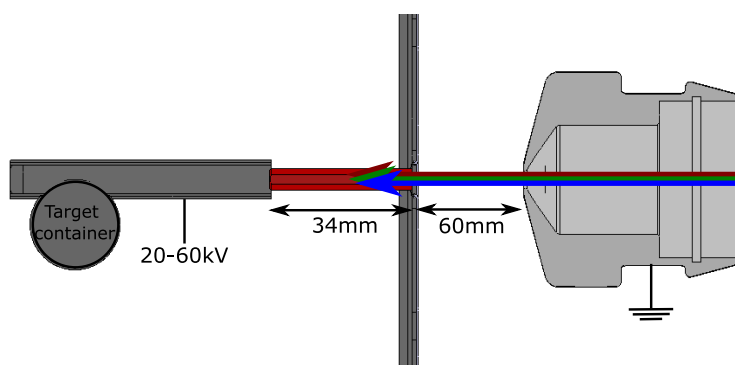
FIGURE 3.16: Working principle of the RILIS ion source. Laser beams are directed into the ion source, where they create singly charged positive ions via multi-step photoionisation.

The RILIS is usually constructed on the basis of the hot cavity surface ion source described in the previous section, which results in an unwanted surface ionised background. This can result in isobaric contaminants with orders of magnitude more intensity than the desired ion species, increasing experimental challenges. Hence, efforts are made to reduce the surface ionised ions e.g. by employing a low work function cavity, ion beam gating or by the de-

velopment and implementation of the LIST ion source, which will be briefly discussed later in this chapter.

By using a low work function surface in the hot cavity, the surface ionisation efficiency for the production of positive ions is significantly reduced according to Eq. 2.37. Beam gating utilises the time structure of the pulsed lasers to only extract ions produced during the time interval of laser ionisation [170, 171]. The laser beams are directed from the laser room through a window in the mass separator magnet and focused into the surface ion source over a path length of about 15 m through the ion source exit hole. RILIS has become the most used ion source at ISOLDE, applied for about 60 % of the ISOLDE operarion. More detailed information on RILIS, scheme development and the laser system can be found in the thesis of K. Chrysalidis [172] as well as in further publications [173, 174, 175, 176].
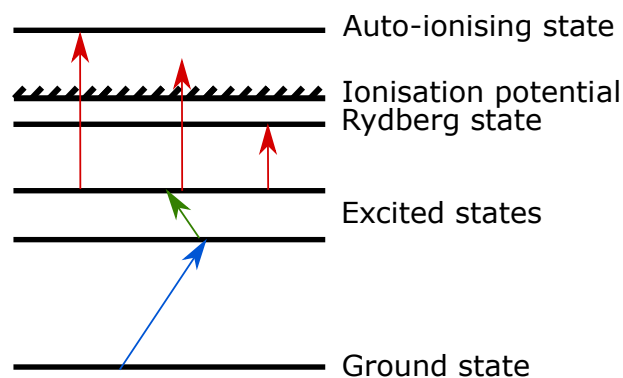
FIGURE 3.17: Ionisation schemes employed by RILIS. An electron is excited from the ground into a higher excited state in a multi-step process. From there, the atom is ionised either via a final optical transition into an auto-ionising state, directly into the continuum or via population of a Rydberg state from which the atom can easily be ionised through black body radiation, collisions or a further laser photon.

FEBIAD type ion sources - VADIS and VADLIS

The **V**ersatile **A**rc **D**ischarge **I**on **S**ource (VADIS) [177] is the ISOLDE version of a **F**orced **E**lectron **B**eam **I**nduced **A**rc **D**ischarge (FEBIAD) ion source [178], shown in Figure 3.18. Electrons are created by resistive heating of a cathode typically made out of tantalum and then accelerated through a grid

with about 50 %-70 % transparency into an anode volume by applying a potential of typically 100 V-200 V to the anode. The incoming electrons scatter in-elastically on the neutral gas atoms inside the anode volume, creating positively charged ions, which then can be extracted.

For low temperatures, the emitted electron current density j_e is described by the Richardson law Eq. 3.14. For high temperatures, when reaching the space-charge limit, it is given by the Child-Langmuir equation [179]

$$j_e = \frac{4}{9}\epsilon_0 \sqrt{\frac{2e}{m_e}} \frac{U^{3/2}}{d^2},$$ (3.17)

where ϵ_0 is the dielectric constant in vacuum, e the elementary charge, m_e the electron mass, U the anode potential and d the distance between anode and cathode. In order to optimize the ionisation efficiency, a tuneable magnetic field is supplied by an electromagnet, additionally shaping the electron trajectories in the anode volume.
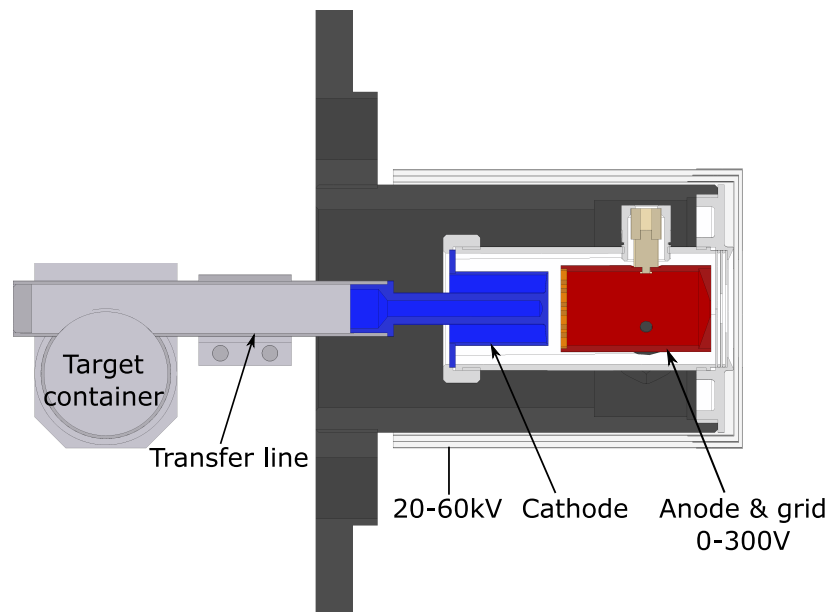
FIGURE 3.18: The VADIS ion source. Electrons emitted from a hot tantalum cathode (blue) are accelerated through a grid (orange), biased with 100 V-300 V, into the anode volume (red) where they create positively charged ions by collision with neutral gas atoms.

An initial model for the VADIS ion source efficiency supported by experimental investigations as well as simulations was developed in the thesis of

L. Penescu [180]. There, it is shown that the efficiency of the VADIS source can be estimated by the expression:

$$\epsilon_{\text{is}} = 2.33 \cdot 10^4 \cdot f \cdot A_{\text{R}} \cdot V_{\text{source}} \cdot \exp \frac{-\Phi}{k_{\text{B}}T} \cdot l_{\text{N}} \cdot \frac{\ln \frac{U}{\text{IP}}}{U \cdot \text{IP}} \cdot \frac{\sqrt{m \cdot T}}{S_{\text{out}}}, \qquad (3.18)$$

where V_{source} is the ion source volume, IP is the ionisation potential in eV, A_{R} the Richardson constant as described in Eq. 3.14, Φ the cathode work function in eV, T the temperature in K, k_{B} the Boltzman constant, l_{N} the number of electrons in the valence shell, U the anode Voltage, m the mass of the element to be ionised in u and S_{out} the area of the extraction hole in cm^2. The parameter f is an adjustment factor for fitting to experimental data, encompassing effects from ion survival and extraction efficiency.

In addition to the normal VADIS operation, there are different variants of the transfer line of the VADIS: One, referred to as VD7, is used for the ionisation of volatile components such as noble gases and certain molecules. Here, the tantalum transfer line is replaced by a water-cooled copper block, creating a cold spot between target container and ion source, where non-volatile elements condense. Another operation mode is the so-called VADLIS, the **L** standing for Laser [181, 182]. Instead of electron impact ionisation, the anode voltage is reduced down to a few volts and selective resonance laser ionisation inside the anode volume is used. In this version, an additional pair of extraction plates is mounted on the source, shaping the potential inside the anode volume to benefit laser ion extraction, similar to the MK3 ion source, a predecessor of the VADIS, where two anodes are employed [183].

Recently, there have also been investigations to use a laser to create photo-electrons instead of using thermal emission. This results in a narrow energy distribution of the electrons produced in a low temperature environment, which might be beneficial for production of volatile molecular ions which decompose easily at high temperature. In addition, it was proposed to utilise the electrons created with well defined energy as a possible way towards the determination of ionisation potentials of superheavy elements [184], similar to the approach of Sato *et al.* [185]. In the work presented in this thesis, the

VADIS was also tested for negative ion extraction, which will be discussed in chapter 5.

The VADIS with its different operational modes has generally high ionisation efficiencies for a broad range of elements and molecules. However, due to its complexity it is more prone to failure, e.g. by insulator breakdown, and does offer almost no element selectivity.

LIST

The **L**aser **I**on **S**ource and **T**rap (LIST) was initially developed at the Johannes Gutenberg-University Mainz to suppress surface ionised species in preparation of a clean laser ionised beam [169, 186, 187]. Here, ions produced by the hot surface ioniser tube are suppressed by an electrostatic repelling potential. However, neutral atoms can effuse out of the surface ion source and into a radio frequency quadrupole which is mounted downstream of the surface ion source. There, the neutral atoms are laser ionised using the RILIS method, while the quadrupole provides a guiding field for laser ion extraction.
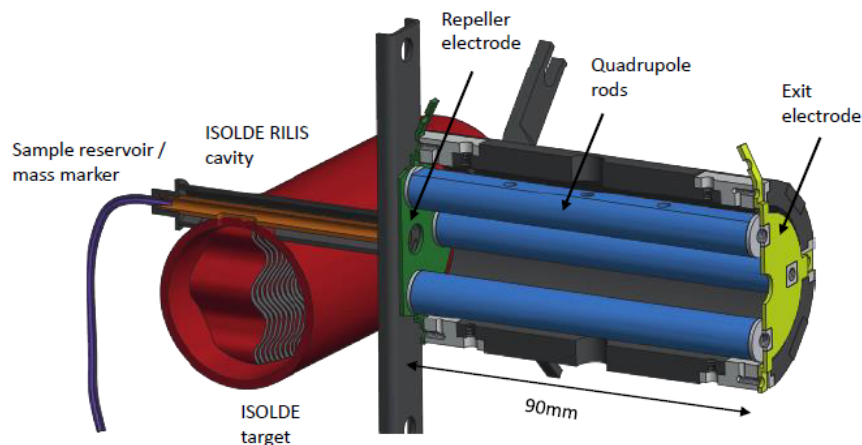
FIGURE 3.19: LIST ion source combined with ISOLDE target (red). Positive ions from the tubular surface ion source (orange) are blocked by a repeller electrode (green), neutral atoms entering the LIST volume are laser ionised and guided out of the LIST by the potential of the exit electrode (light green) and a RF guiding field provided by the quadrupole rods (blue). Figure courtesy of R. Heinke [187].

In its initial design, described in the thesis of K. Wies[188], it was also foreseen to use the LIST as a cooler buncher, employing buffer gas for cooling as well as a trapping potential at the exit of the LIST geometry to trap and bunch the ions. However, for the use as a source for radioactive ion beams at ISOLDE, the initial concept was adapted. At ISOLDE, the LIST is not used as a longitudinal trap, but purely employed in its function to suppress unwanted surface ionised contaminants and provide a laser ionisation volume with a guiding field generated by the quadrupole rods. In addition, it can be used in an "ion-guide" mode, where ions are guided through the LIST volume without any suppression potentials. A schematic view of the ISOLDE version of the LIST is shown in Figure 3.19. The latest LIST developments and further details are discussed in the thesis of R. Heinke [187].

KENIS

The **K**inetic **E**jection **N**egative **I**on **S**ource (KENIS) was developed at Oak Ridge National Lab for the production of negative fluorine beams [189, 190]. It uses a similar approach as the caesium sputter sources described in chapter 2, however in this case adapted to atoms in gas phase in contrast to the solid cathodes using macroscopic amounts of material. As shown in Figure 3.20, neutral gas atoms diffuse through a resistive heated hot tantalum transfer line and collide with a conical cathode at the exit of the ion source. An additional, heatable tantalum tube is located within the transfer line, supplying caesium vapour from a reservoir. The caesium atoms are then positively ionised at the end of the transfer line by means of a 50 % porosity tungsten ioniser which is usually held at about 1200 °C.

Subsequently, the Cs^+ ions are accelerated onto the conical aperture by a molybdenum acceleration grid with 90 % transparency biased to about $-200\,V$ in respect to the transfer line. As in a caesium sputter source, the caesium ion beam kinetically ejects attached atoms and breaks up molecules into their constituents.

In addition, a surface layer of neutral caesium acts as an electron donor, increasing the negative ion yield. In order to re-direct backwards-deflected

ions towards the extraction potential, the grid is held in a slightly more negative potential then the ioniser cone.
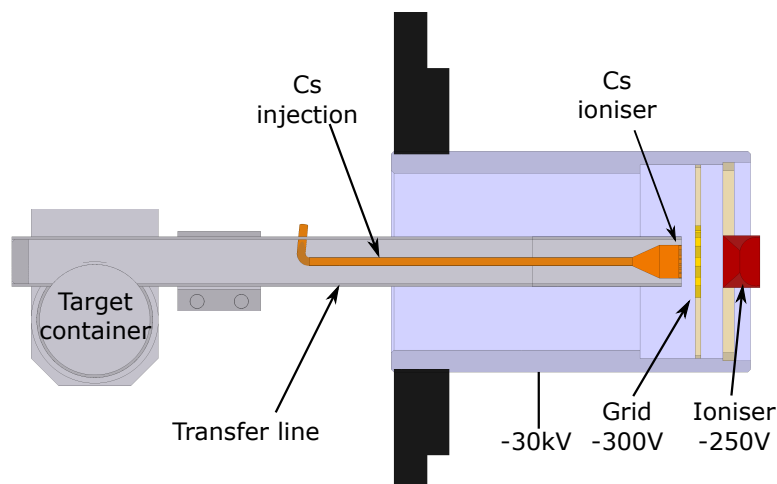
FIGURE 3.20: The KENIS ion source. Neutral gas atoms diffuse through a transfer line (grey) onto the ioniser (red), which is biased to $-250\,\text{V}$. Cs is fed through a heated injection line at the end of which it is ionised positively by a tungsten ioniser (orange). A grid (yellow) biased to about $-300\,\text{V}$ then accelerates the positive Cs ions onto the conical ioniser ejecting the condensed species as negative ions.

In the work presented in this thesis, the KENIS was rebuilt to investigate its suitability for negative ion beam production of fluorine as well as other elements outside of the halogen group, which are currently not efficiently produced with the existing surface ion source.

Aside from the gained beam purity in using negative ions, e.g. negative oxygen beams are of interest for the PUMA project [36]. In addition, oxygen is expected to have a similar EA as polonium, making it a suitable analogue to study production efficiencies offline. The results of these studies are discussed in chapter 5.

3.3.3   ISOLDE thermal calibration stand

Before a target and ion source system is coupled to one of the ISOLDE Frontends, it undergoes several procedures for quality control. After assembly, the first tests are carried out at the designated ISOLDE thermal calibration

stand, shown in Figure 3.21. Here, a target unit can be coupled to a DN100 5-way vacuum cross and evacuated to pressures around 1×10^{-7} mbar. Subsequently, target container and transfer line are resistive heated to perform a step-wise temperature calibration via a pyrometer, measuring electric heating power against temperature. In addition, this process ensures vacuum tightness under operating conditions.

Furthermore, outgassing of the targets can be monitored via a residual gas analyzer (RGA). A second version of this test stand, referred to as "carburization stand" is used in ISOLDEs Class A laboratory to produce specifically actinide target materials such as uranium carbide. In addition to the standard quality control procedure, this test stand is frequently used for temperature studies of target and ion source prototypes as well as other experiments that do not require the extraction of an ion beam from the source.

FIGURE 3.21: Image of the ISOLDE thermal calibration stand.

3.3.4 ISOLDE Offline separators

The technical team responsible for target delivery and ISOLDE infrastructure operates two offline mass separators, referred to as "Offline 1" and "Offline 2". Offline 1, shown in Figure 3.22 has two main purposes. First it is used for quality control to ensure the functionality of target units prior to delivery to ISOLDE for on-line use. Second, it is used as a test bed for target and ion

source development, where efficiency and reliability of prototype targets are investigated. Both separators consist of a Frontend similar to the ISOLDE ones, where an ISOLDE target unit can be coupled and subsequently an ion beam extracted with energies of up to 60 keV by biasing the Frontend. Focussing and guiding ion optical elements such as electrostatic steerers and an Einzel lens or quadrupole triplet inject the ion beam into a mass separating magnet after which several detection devices such as Faraday cups and single ion counting detectors can be mounted. Offline 1, described by J. Lettry [191], was used for the ion source studies in this thesis.
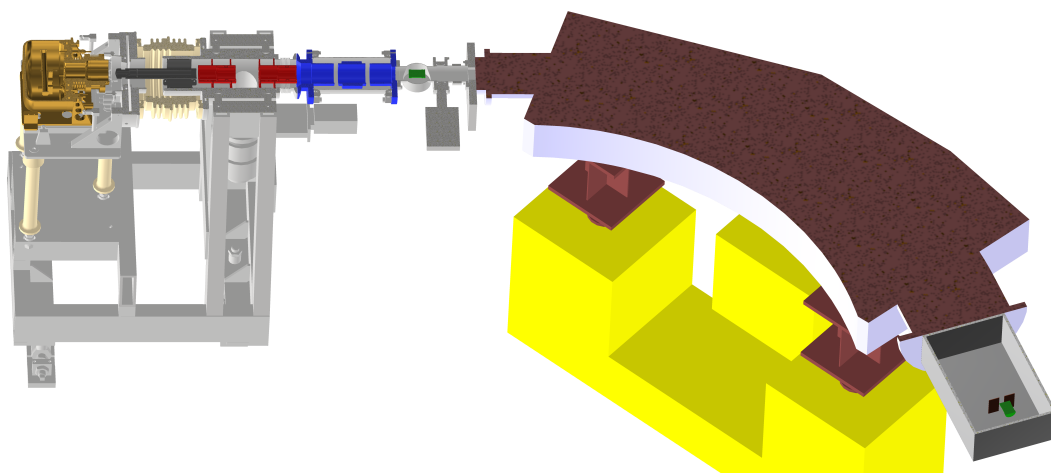
FIGURE 3.22: The ISOLDE Offline 1 facility. The target unit (brass) is coupled to the frontend and electrically insulated by ceramic insulators (beige). Ions are extracted by a 30 keV potential difference between target unit and extraction electrode (dark grey). The ions are then focused into a separating magnet (brown) by x- and y- steerers (red) and an Einzel lens (blue). The ion beam intensity before and after the mass separator can be measured with FCs (green).

Following the extraction electrode, the beam is focused into the mass separating magnet with an Einzel lens which can be operated with up to 20 kV. The magnetic field of the magnet is controlled with a power supply delivering up to 150 A of current to the magnet. Upon exiting the magnet, the ion beam is guided into a detector box, where slits and a wire scanner are employed in front of two interchangeable current detecting devices, typically a Faraday cup and a multi channel plate (MCP) or MagneTof detector [192].

Additionally, a window in the separator magnet enables laser ionisation scheme developments or other spectroscopic in-source studies. These tasks can now be shared with the newly build Offline 2, which has some additional features, the main being a radio frequency cooler-buncher (RFQcb) downstream of the mass separator, as is the case at ISOLDEs HRS separator [158, 157, 193]. This enables in-depth testing of working modes of this device as well as studies of e.g. molecular breakup in the RFQ. A detailed description of Offline 2 is given in the paper by S. Warren [194] and the thesis of A. Ringvall-Moberg [195].

Chapter 4

Experimental methods

4.1   GANDALPH

The **G**othenburg **AN**ion **D**etector for **A**ffinity measurements by **L**aser **PH**oto-detachment (GANDALPH), shown in Figure 4.1 is a detector built for the measurement of electron affinities of radioactive isotopes. The first version of GANDALPH was built at the University of Gothenburg and CERN. It was successfully used to perform the first electron affinity measurement of a radioactive isotope, utilising laser photodetachment threshold spectroscopy of ^{128}I [50]. In order to minimise the background resulting from collisional detachment, a differential pumping section is placed at the entrance of GANDALPH, which allows pressures as low as 5×10^{-10} mbar in the interaction region, despite e.g. the ISOLDE beamline generally being at pressures between 1×10^{-7} mbar and 1×10^{-6} mbar.

A negative ion beam enters GANDALPH at an angle of 35° and is deflected by two electrostatic steerers into an interaction region, defined by two apertures with 6 mm diameter placed at a distance of 0.5 m. Here, the ions are overlapped collinearly with a laser beam, resulting in photodetachment as described in chapter 2. Following the interaction region, residual charged particles are electrostatically deflected into either a *Detech XP-2334* channel electron multiplier (CEM) for low intensity beams, or a Faraday cup for beam intensities greater than approximately 1 pA. Neutral atoms continue on their straight trajectory and enter the neutral particle detector, shown in Figure 4.2 where they impinge on a target, creating secondary electrons. Subsequently,
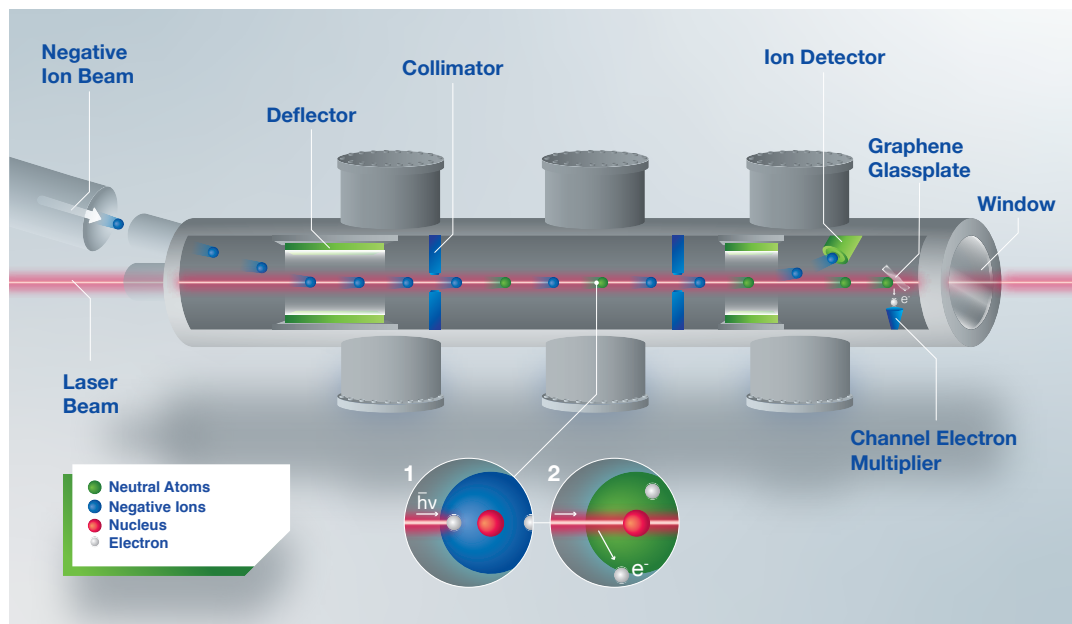
FIGURE 4.1: Schematic diagram of the GANDALPH detector. From left to right: A beam of negative ions is guided into GANDALPH, where it is overlapped with a frequency tune-able laser beam in the interaction region in either co- or counter-propagating geometry. By absorbing a photon (Inset 1), an electron can gain enough energy to be ejected from the ion, thereby creating a neutral atom (Inset 2). After the interaction region, charged particles are deflected into an ion detector, while neutralised atoms continue moving straight to the graphene-coated glass plate downstream and create secondary electrons, which are detected by a channel electron multiplier. Figure taken from Publication C.

these electrons are deflected into an off-axis CEM (*Detech XP-2334*) and registered via a *SRS400, Stanford Research Systems* photon counter.

In order to avoid any electric charging of the target as well as to permit the transmission of laser light, the target has to be both transparent and conductive. D. Hanstorp designed a detector using targets made of quartz coated with a layer of indium tin oxide (ITO), providing a good compromise of conductivity and transparency [196]. The transparency of ITO is relatively constant with about 80 % in the visible and infrared range, however for wavelengths below 400 nm it decreases rapidly [197]. Additionally, with increasing photon energy, the creation of photoelectrons by the laser pulse passing through the ITO target creates very large background in the detector. Hence, the ITO layer was exchanged with a target consisting of a quartz plate coated

with graphene. This plate was successfully used during the campaign to measure the EA of astatine, described in publication C. Graphene is reported to be almost 100 % transparent down to wavelengths of 200 nm [197]. The graphene layer on a quartz plate substrate was produced by the company Graphenea utilising chemical vapour deposition (CVD) and installed in the neutral particle detector as shown in Figure 4.2.
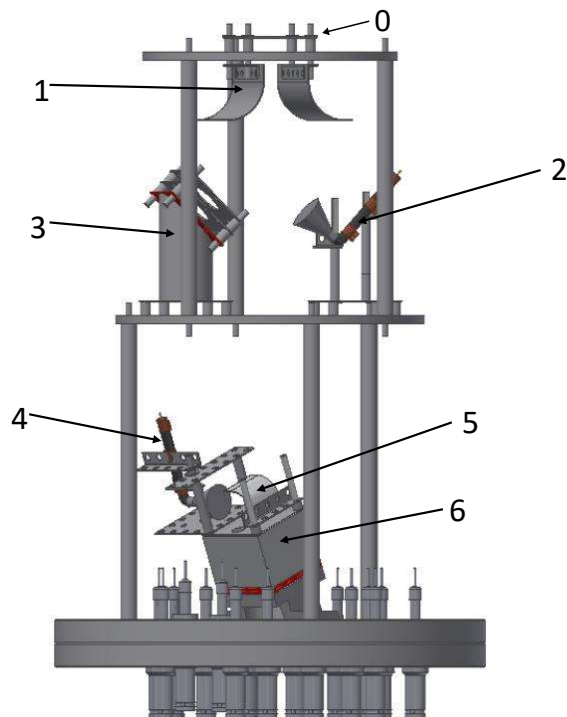
FIGURE 4.2: The neutral particle detector in GANDALPH. Charged particles enter through an aperture (0) and are deflected by electrostatic deflectors (1) either into a FC (3) or a CEM (2). Neutral particles enter the "box" (6) in which the graphene coated quartz plate is mounted (red). Secondary electrons are guided into a second CEM (4) by an electric deflector (5).

Initial tests were performed at the **G**othenburg **U**niversity **N**egative **I**on **L**aser **LA**boratory (GUNILLA) [92] using negative ruthenium ions and laser wavelengths as short as 230 nm while achieving a reduced background from photoelectrons in comparison to ITO due to the high transmission and an electrostatic suppression via a biased grid in front of the CEM. Further details of these tests are given in publication B. For GANDALPH, the CEM for

secondary electron detection was placed off-axis to avoid influence by decay products of radioactive species implanted on the quartz plate.

In addition to the improvements in the neutral particle detector, GANDALPH underwent several upgrades to improve ion beam tuning and data acquisition, detailed in publication B. A LabView based control system for the twenty high voltage channels necessary for the ion optical elements was developed utilising a twenty-four channel voltage control instrument build by L. Bengtsson [198]. Additionally, segmented aperture plates were added on the neutral particle detector and at the exit of the differential pumping section as part of the authors master thesis [103]. In combination with a four channel picoampere meter, this facilitates the determination of the direction and the readjustment of any possible beam misalignment. Finally, for the measurement of the EA of alpha emitting elements such as astatine and polonium, an alpha spectroscopy setup was added to GANDALPH, shown in Figure 4.3. An Ortec Alpha Aria spectrometer with a *BU-024-600-AS* detector was mounted on top of the GANDALPH chamber such that the detector is placed out of the line of sight of laser and ion beam. Neutral atoms are implanted on an aluminium plate which is descended into the beam utilising
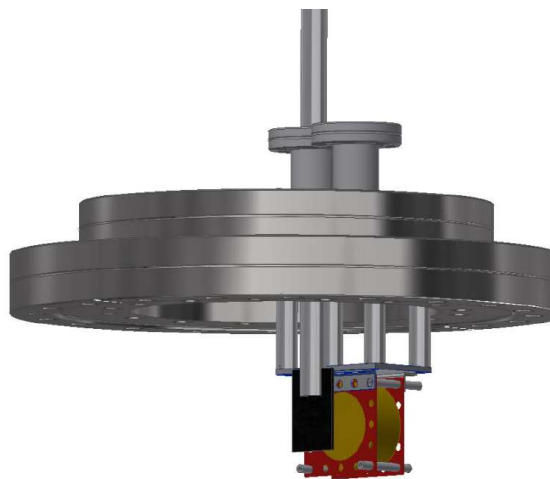
FIGURE 4.3: Alpha spectroscopy setup for GANDALPH. An aluminium plate (black) can be lowered into the beam line via a pneumatic feedthrough. After the ion beam is implanted on the plate, it is retracted back to face the alpha detector to detect the collected activity (red-gold). Image taken from publication A.

a pneumatic feedthrough. Subsequently, the plate is retracted and positioned in front of the alpha detector for measurements. The mechanism is controlled using a self-developed LabView software, allowing measurement sequences to be programmed.

4.2 Multi-Reflection Time of Flight devices

Multi-Reflection Time of Flight (MR-ToF) devices [199] consist of a combination of mirror electrodes with a drift section in between to reflect and essentially trap ion bunches. As mentioned in chapter 3, this can be used to mass separate ions by trapping them for thousands of revolutions, effectively increasing the flight path significantly. Using this method, MR-ToFs can reach mass-resolving powers $\frac{m}{\Delta m}$ of several hundred thousand [200, 201]. The disadvantage is that no continuous beam but rather ion bunches are required to be injected into the MR-ToF, which demands low longitudinal and transversal emittance with specifically short pulse widths. As a result, continous beams (or bunched beams with high emittance or long pulse lengths) require cooling and bunching prior to injection. Consequently, ions can be lost during capture and trapping, in addition to losses when the trap's space charge limit is reached, giving an upper limit of the number of ions allowed in the trap. In addition to its use as a mass spectrometer, the MR-ToF can be used for collinear laser spectroscopy, e.g. by placing a photomultiplier in the field-free region to detect fluorescence photons [202].

The MR-ToF used in this work is part of the **M**ulti **I**on **R**eflection **A**pparatus for **C**ollinear **L**aser **S**pectroscopy (MIRACLS) proof-of-principle experiment [202], shown in Figure 4.4, which serves as a benchmark tool for the development of such a specific MR-ToF operated with a beam energy of up to 30 keV [203]. The setup consists of an electron impact ion source used at the moment mainly to produce positive magnesium ions, which are accelerated to beam energies of up to 450 eV and injected into a linear Paul trap used as radio frequency cooler-buncher filled with helium buffer gas, where the ions are cooled and bunched.
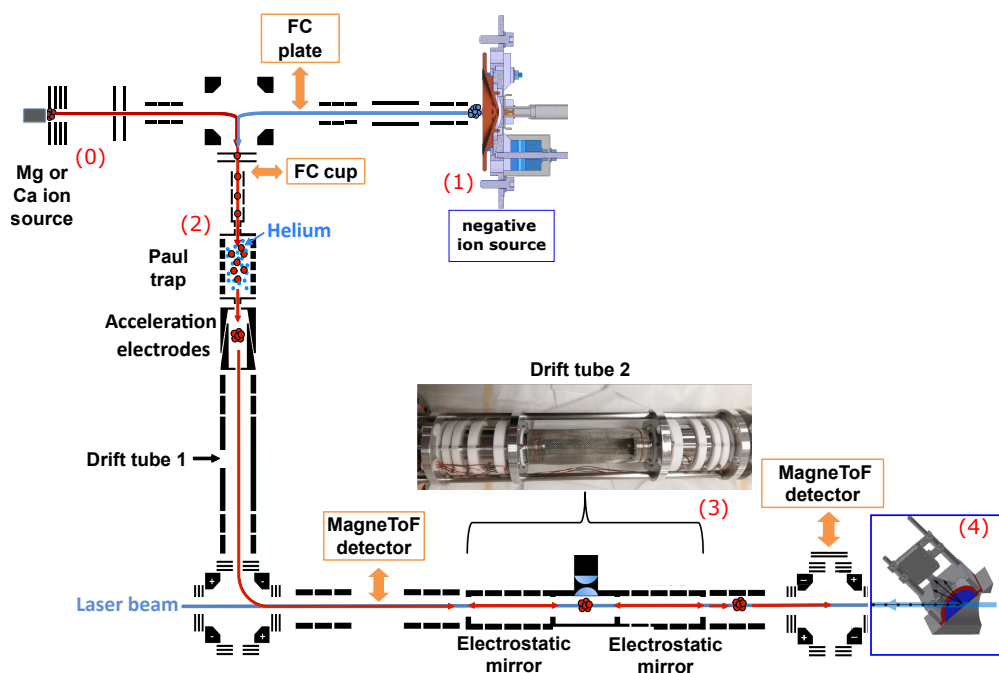
FIGURE 4.4: MIRACLS setup adapted for both positive and
negative ion studies. An ion beam produced by either the pos-
itive (0) or negative (1) ion source is guided into a Paul trap (2),
where it is cooled and bunched using helium buffer gas. The
ion bunch is then accelerated into the MR-ToF (3), consisting
of four elecrostatic mirrors. After a set number of reflections,
the ion bunch is released and detected with a MagneToF detec-
tor. Neutral atoms created in a photodetachment process can
be detected with a neutral particle detector (4) at the end of the
beamline. Graphic adapted with permission from F. Maier *et al.*
[204].

The bunched beams are then re-accelerated by an acceleration electrode
and a pulsed drift tube (drift tube 1) [205], reaching an energy of 2 keV. The
ions are then trapped between a set of four mirror electrodes on each side,
using the in-trap technique described by R. Wolf *et al.* [206]. Here, the ion
beam energy is reduced to 1.3 keV utilising a second pulsed drift tube, drift
tube 2, situated in the center of the MR-ToF, while the mirror electrodes pro-
vide electrostatic potentials for reflecting and focussing the ion bunch. Drift
tube 2 consists of two electrodes connected to a metallic mesh, thereby also
providing a field free region with optical transparency for fluorescence mea-
surements utilising a photomultiplier placed on top. Alternatively, ions can

be trapped utilising the mirror-switching technique, where the potential of the mirror electrodes is altered to allow the capture, trapping and release of the ion bunch [206]. In order to transmit the ion bunch without trapping, drift tube 2 is kept on a constant potential of about 620 V. To trap ions in the MR-ToF, it is switched to ground once the ion bunch is in the center of the drift tube. More detailed information on the MIRACLS proof-of-principle setup can be found in articles by S. Sels [202] and F. Maier [204], as well as severel theses [207, 208, 209].

For the negative ion work, the setup was supplemented by an additional beam-line with a negative ion source and a neutral particle detector downstream of the MR-ToF, as shown within the blue frames in Figure 4.4. In addition, the MagneToF detector in front of the Paul trap was exchanged by a Faraday cup and the two MagneToF detectors before and after the MR-ToF were equipped with an AC-coupler, floating the detector and therefore enabling both positive and negative ion detection.

The development of the negative ion source beamline as well as the adaptation of the neutral particle detector is discussed in detail in chapter 6.

4.3 Lasers

The Laser, an acronym for **L**ight **A**mplification by **S**timulated **E**mission of **R**adiation, is a coherent light source first built by T.H. Maiman in 1960 [210]. Since then, it has become one of the most important tools in research, industry, communication and numerous other applications.

Stimulated emission is the process of inducing the emission of a photon from a medium due to the presence of another photon [13]. The emitted photon has the same polarisation, energy and direction as the initial one. Usually, absorption exceeds stimulated emission due to the atoms of the medium being in a lower lying or ground state $|1\rangle$ of the laser transition in the gain medium. Hence, amplification of the initial photon can only be achieved when an excited state $|2\rangle$ is more populated than $|1\rangle$, which is called population inversion. In a laser, this is achieved by an external power source

(e.g. electrical or optical) referred to as the pump. A common method to provide pump power is via the second harmonic of a Nd:YAG laser, which are commercially readily available.

However, population inversion can not be achieved in a simple two level system, since the competition of absorption and emission processes allows equal population at most. Hence, the simplest laser system employs a three-level scheme such as the ruby crystal (Al_2O_3:Cr) used by Maiman [210]. In a three-level system, the electron is excited into a higher lying state $|3\rangle$ by the pump, then decays into a lower lying excited state $|2\rangle$ and finally back to the ground state $|1\rangle$ via the laser transition. Here, the lifetime of the intermediate state $|2\rangle$ has to be longer than that of $|3\rangle$ in order to achieve population inversion between state $|1\rangle$ and $|2\rangle$. Most modern lasers, such as e.g. the Nd:YAG, consist of a gain medium with a four level system, where an additional intermediate level $|2\rangle$ is utilised. In this scheme, electrons are excited from the ground state $|1\rangle$ into the highest of the four participating states, $|4\rangle$, from which they decay into a lower lying state $|3\rangle$. The laser transition via stimulated emission occurs then between the intermediate states $|3\rangle$ and the state $|2\rangle$, situated below. The benefit of the additional intermediate state $|2\rangle$ in comparison with the three-level scheme is the increased feasibility of creating population inversion: If the decay from $|2\rangle$ into $|1\rangle$ is fast, the population of $|2\rangle$ is low, thereby strongly facilitating the creation of a population inversion between $|2\rangle$ and $|3\rangle$ for the laser transition. Both three- and four level lasing schemes are shown in Figure 4.5. In any case, the amplification is enhanced by an optical resonator surrounding the gain medium, resulting in the photons travelling either back and forth or in a closed loop in the laser cavity, depending on the chosen geometry of the cavity.

For many spectroscopic studies, i.e. photodetachment experiments, where the laser wavelength is tuned across the photodetachment threshold, it is necessary to utilise a gain medium with a broad emission spectrum instead of only a distinct line. One of the most commonly used gain media for visible light is the titanium-doped sapphire crystal (Ti^{3+}:Al_2O_3, titanium:sapphire or short "Ti:Sa"), where the lasing transition takes place between two vibra-

tional states broadened by the sapphire crystal field, enabling a laser output wavelength in the range of 650 nm to 1050 nm. This range can be extended by second, third or fourth harmonic generation [211, 13] using a non-linear optical medium such as a β-barium borate (BBO) crystal which exhibits a double refraction to allow for phase matching of the first and the higher order harmonics.
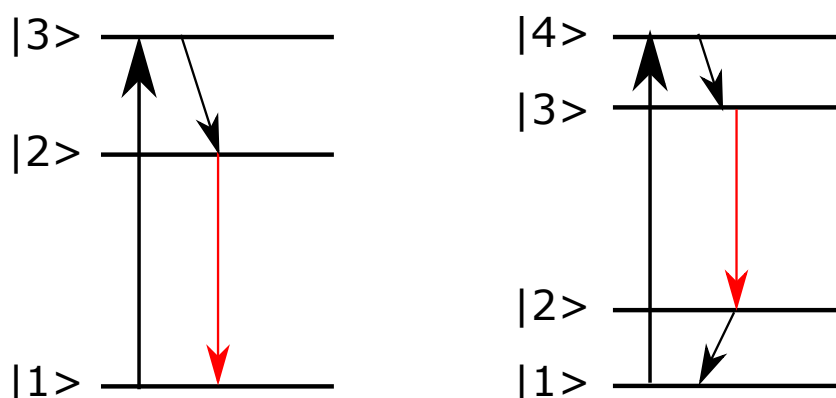
FIGURE 4.5: Three (left) and four (right) level laser scheme. The arrow in red marks the laser transition.

An alternative to solid state lasers such as the Ti:Sa is the dye laser, which historically was the first laser with a broadly tuneable wavelength range. Here, the gain medium consists of a liquid solution of fluorescent organic molecules. The wavelength range of a dye laser is limited by the fluorescence of the available dye solution, but it is easily exchangeable. Dye lasers also utilise a four-level scheme, where the transitions occur between two electronic levels with a range of vibrational and rotational states, leading to broad absorption and emission bands. A drawback however is the bleaching of the dye, leading to losses in power over time and the necessity to frequently change the dye solution. Dye lasers are operated in the visible to the infrared range, depending on the chosen dye.

The laser system used for the determination of the EA of astatine in this thesis is part of the ISOLDE RILIS (see chapter 3), as discussed in detail in publication C. For the photodetachment measurement, a commercial dye laser (*Credo Dye, Sirah Laser- und Plasmatechnik GmbH*) operated with an etha-

nol solution of Coumarin 503 dye was used to produce laser light in the range of 490 nm to 520 nm with an output power of 20-30 mW measured at the exit of GANDALPH.

The dye laser was pumped by the third harmonic output (355 nm) of a pulsed Nd:YAG INNOSLAB laser (*CX16III-OE, EdgeWave GmbH*) with a 10 kHz pulse repetition rate. Typical values of the spectral bandwidth and pulse duration emitted by the dye laser were 12 GHz and 7 ns, respectively. The photon energy of the laser radiation was measured using a wavelength meter (*WS7, HighFinesse/Ångstrom*) which is regularly calibrated by a single-mode helium-neon laser.

For the isotope shift of the EA of chlorine at the MIRACLS proof-of-principle setup, the continuous wave laser system of the MIRACLS group was used, which is discussed in detail by S. Sels [202]. It consists of a *Sirah MATISSE* dye laser, pumped by a *Spectra Physics Millenia* Nd:YAG laser with up to 20 W output power. Second harmonic generation of the cw output of the MATISSE can be provided by a *Spectra Physics Wavetrain* frequency doubler.

4.4 Material characterisation techniques

4.4.1 X-ray and ultraviolet photoelectron spectroscopy

In X-ray photoelectron spectroscopy (XPS), a sample is exposed to electromagnetic radiation in the soft X-ray range ($\approx$100 eV to 2 keV). The atoms in the sample absorb photons, resulting in the emission of an electron from a low atomic state e.g. the K shell. By measuring the kinetic energy of the released electron, its binding energy can be determined, which is characteristic for the atomic structure of the element from which it was released. In that way, XPS can be used to determine the atomic constituents of the surface of a sample. In addition, the work function of the sample can be determined by analysing the energy spectrum of the emitted electrons [212, 213, 214]. The energy of an emitted electron is given by

$$E = E_{\mathrm{ph}} - (E_{\mathrm{F}} - E_{\mathrm{B}}) - \Phi, \tag{4.1}$$

where E_{ph} is the photon energy, E_{F}, the Fermi level, E_{B} the binding energy in the sample referring to the Fermi level and Φ the work function.

The minimum energy E_{min} of an emitted electron is zero, while the maximum energy of an electron is given by $E_{\mathrm{max}} = E_{\mathrm{ph}} - \Phi$. Usually, a bias voltage is applied to the sample in order to deconvolute the surface work function from that of the spectrometer, thereby shifting the spectrum uniformly. Consequently, the work function of the sample is then given by

$$\Phi = E_{\mathrm{ph}} - (E_{\mathrm{max}} - E_{\mathrm{min}}). \tag{4.2}$$

In addition, if a conducting sample is in contact with a second conductor with known work function, the Fermi levels of those materials will equalise. Consequently, the work function can be determined by the difference in the secondary emission onsets [214].

Ultraviolet photoelectron spectroscopy (UPS) utilises the same method but photons in the UV regime ($\approx 3\,\mathrm{eV}$ to $100\,\mathrm{eV}$). Therefore, mainly the valence band of the material is probed. Furthermore, the penetration depth in comparison to X-rays is smaller, making UPS more sensitive to surface contamination. Additionally, the bandwidth of the light source is usually narrower compared to XPS, which increases the precision with which the work function can be determined. The setup used in this thesis is owned and operated by the TE-VSC-SCC section at CERN and is described in the thesis of V. Petit [215].

4.4.2 X-ray diffraction

An X-ray diffractometer consists of an X-ray source, a sample holder and detector, as shown in Figure 4.6. Most X-rays impinging on a crystal are transmitted without interaction, however a fraction is diffracted according to Bragg's law [216, 217]

$$n\lambda = 2d_1\sin(\theta), \tag{4.3}$$

where, λ is the wavelength of the X-ray photon, d_1 the lattice parameter, n a positive integer and θ the incident angle of the beam.
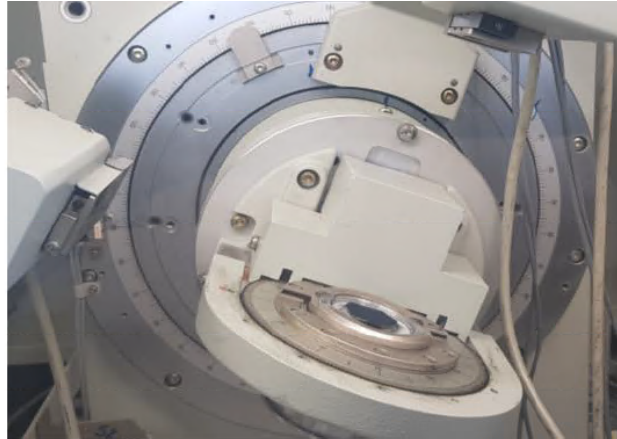
FIGURE 4.6: The X-ray diffractometer used for phase composition investigations. A sample (dark blue) is placed on a rotatable sample holder and irradiated by a X-ray source (left). The diffacted X-rays are measured by a move-able detector (upper right).

Therefore, the lattice parameter of a given crystal can be determined by varying the incident angle of the X-rays and detecting the diffracted beam, resulting in a diffractogram unique to the phase composition of the sample which can then be determined by comparing with a database of known samples. In order to ensure detection of all phases and crystal orientations, samples are ground to powder and prepared on a quartz plate, oftentimes by mixing with a drop of liquid to ensure the flatness of the surface. The X-ray diffractometer used in this thesis was the *Siemens Bruker D5000* owned and operated by the EN-MME-MM section at CERN.

Chapter 5

Negative ion source development

5.1 Low work function materials

Currently, the most commonly used material for surface ionisation in negative ion sources is LaB_6, as mentioned in chapter 2 and 3. With a work function of about 2.6 eV [100], LaB_6 yields good efficiencies for the halogen elements. However, issues with surface poisoning and temperature stability have been reported [59, 63, 218]. In addition, ionisation efficiencies are low for elements with lower EAs, i.e. elements outside of the group of halogens, as discussed in chapter 2.

Hence, other ioniser materials with lower work function and higher operating temperatures are desirable. Besides the hexaborides, oxide materials such as ThO, SrO or BaO are often utilised as coating on e.g. a tungsten filament to reduce the work function and thereby facilitate electron emission in cathode materials. These materials have also been investigated as low work function cavity for the suppression of positive surface ions when using resonance laser ionisation [102, 219]. However the chemical stability is poor above temperatures of $\approx 1200\,°C$ [219]. Two other candidates, the hexaboride GdB_6 and Ir_5Ce were previously employed at ISOLDE, however not resulting in a significant improvement of the ion source performance [102].

5.1.1 Strontium vanadate

Strontium vanadate, $SrVO_3$, is a perovskite material predicted to have a work function as low as 1.8 eV [220, 221]. It is a possible candidate for use as an

anode material in solid oxide fuel cells, but is reported to decompose in atmospheres with high oxygen partial pressure [222, 223, 224, 225].

Nevertheless, the prospect of the significant lower work function together with the potential to stabilise the material by metal doping [221], in order to achieve a similar operating temperature as LaB_6, make it a candidate for a new ioniser material. As a first step towards the study of $SrVO_3$, a campaign was started to produce and characterise a sample at ISOLDE, initiated already in my master thesis [103] and continued in the present work.

Strontium vanadate production

$SrVO_3$, shown in Figure 5.1, was produced by mixing powders of $SrCO_3$ and V_2O_5 so that the ratio of strontium to vanadium is $1:1$. The mixed powder was ground with a mortar for several minutes and subsequently pressed into a pellet using a manual hydraulic press with a pressure of about $196\,kPa$. The pellet was baked in air at $600\,°C$ for about $10\,h$, followed by a period of $10\,h$ at $800\,°C$ producing strontium vanadate phases with oxygen excess, i.e. $Sr_2V_2O_7$, $Sr_3V_2O_8$.
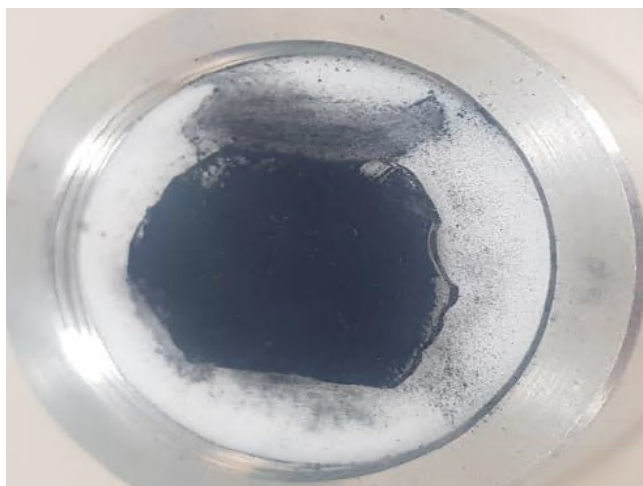
FIGURE 5.1: Strontium vanadate sample prepared for measurements with the X-ray diffractometer, with $SrVO_3$ being the dark powder.

Subsequently, the sample was placed inside a graphite tube and reduced in a flow of $2.5\,ml/min$ formier gas ($5\,\%$ hydrogen, $95\,\%$ nitrogen) at $1100\,°C$ in a *Carbolite Gero STF* tube furnace type oven. The phase composition was

determined using the X-ray diffractometer (XRD) described in chapter 4. The sample pellets were ground down and mixed with ethanol to create a flat surface of powder on a quartz substrate, as shown in Figure 5.1.

The resulting spectrum is shown in Figure 5.2, where the sample shown in Figure 5.1 was identified as cubic $SrVO_3$. The slight shift of the peaks likely results from a slight slope on the surface of the sample.
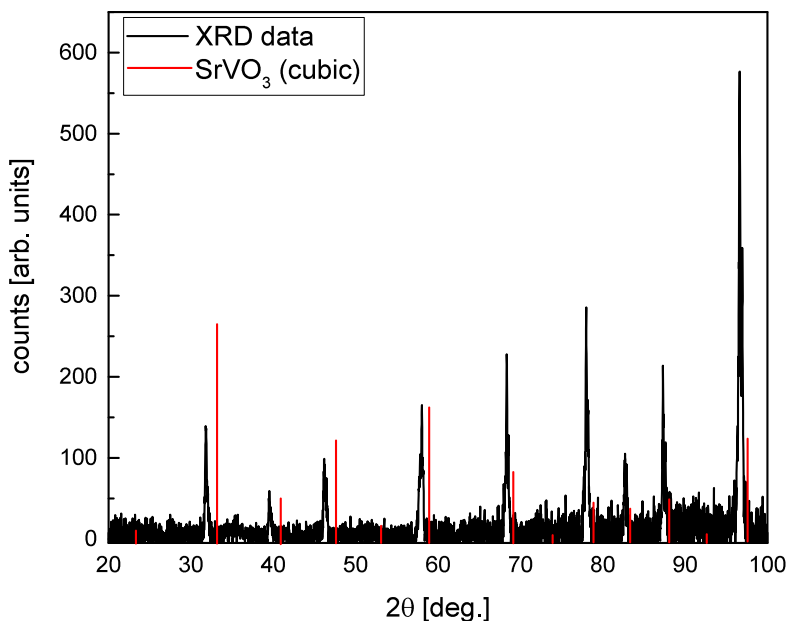
FIGURE 5.2: XRD spectrum of $SrVO_3$. The composition matches well with the cubic phase of $SrVO_3$, indicated by the red lines, taken from a crystallographic database provided by the *Bruker DIFFRAC.EVA* software.

Work function of $SrVO_3$

Work function determination via ultraviolet photoelectron spectroscopy (UPS, as described in chapter 4) was attempted. In order to confirm the suitability of the setup for powder pellets, an initial benchmark was performed using a purchased LaB_6 pellet at room temperature. The resulting UPS spectrum is shown in Figure 5.3.

Here, the work function for LaB_6, determined from the onset energy subtracted by the sample bias, resulted to about 4.65 eV, which is significantly higher than literature values. This is likely due to oxidation and contamination of the surface, resulting from sample handling and storage in air, as

shown by the determination of the surface composition by XPS, shown in
Figure 5.4. The surface consists of 18.0 % boron, 39.3 % carbon, 6.2 % lan-
thanum, 2.1 % nitrogen and 34.4 % oxygen.

Since it was not possible in this experimental setup to heat the sample
to the operating temperature necessary to activate or clean the surface and
to avoid contaminating the measurement chamber due to outgassing, it was
deemed not possible to accurately determine the work function using this
method. However, the chemical composition could be confirmed and typical
surface contaminants identified, as mentioned above.
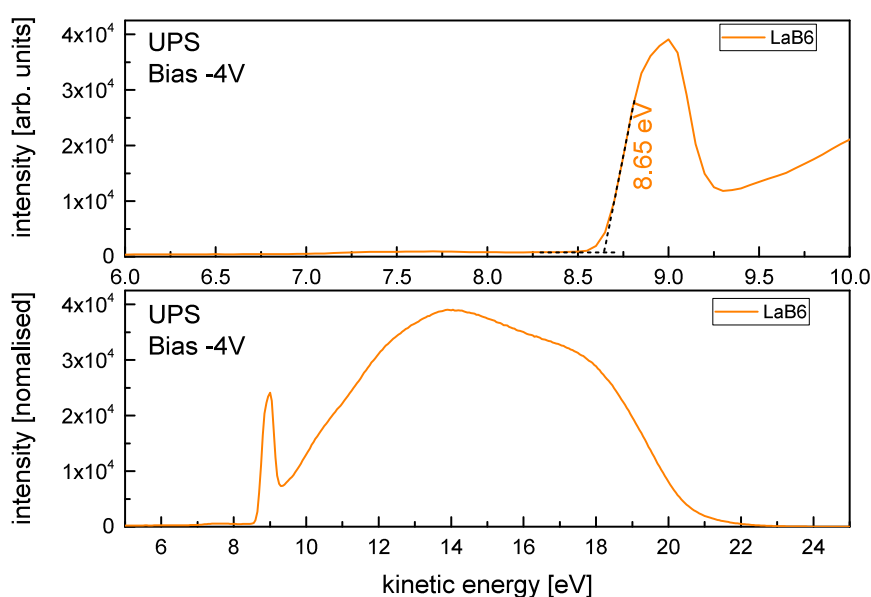
FIGURE 5.3: UPS spectrum of LaB_6. Top: Zoom in of the onset
region with extrapolated onset energy. Bottom: Complete spec-
trum. The kinetic energy of the electron at the onset subtracted
by the bias voltage corresponds to the work function.

Therefore, the work function of $SrVO_3$ was determined using thermal
emission at the thermal calibration stand (described in chapter 3). A sample
of $SrVO_3$ was prepared in form of an ioniser pellet in a MK4 negative surface
ion source as described in chapter 3. Temperature calibration of the surface
was performed using a disappearing-filament type optical pyrometer. Sub-
sequently, the electron emission current was measured in dependence of the
temperature using the pre-extraction plate of the MK4 as a collector for the
emitted electrons with the center hole closed by a copper plug. The pre-
extraction plate was biased with a positive potential of 0.5 kV, 1 kV or 1.6 kV,

and the resulting current to ground was recorded using a picoampere meter.

The work function can then in principle be determined by fitting the Richardson-Dushman equation, discussed in chapter **??**, to the data. However, there are several effects which have to be considered. The applied electric field reduces the work function of the material by $\Delta\phi = \sqrt{\frac{e^3 E_E}{4\pi\epsilon_0}}$, described by the Schottky effect, where $E_E \approx \frac{U}{d}$ is the electric field strength (shown in Figure 5.5 for a potential of $1\,\text{kV}$), U the potential, d the distance between pellet and pre-extraction plate, e the elementary charge and ϵ_0 the absolute dielectric permittivity in vacuum.
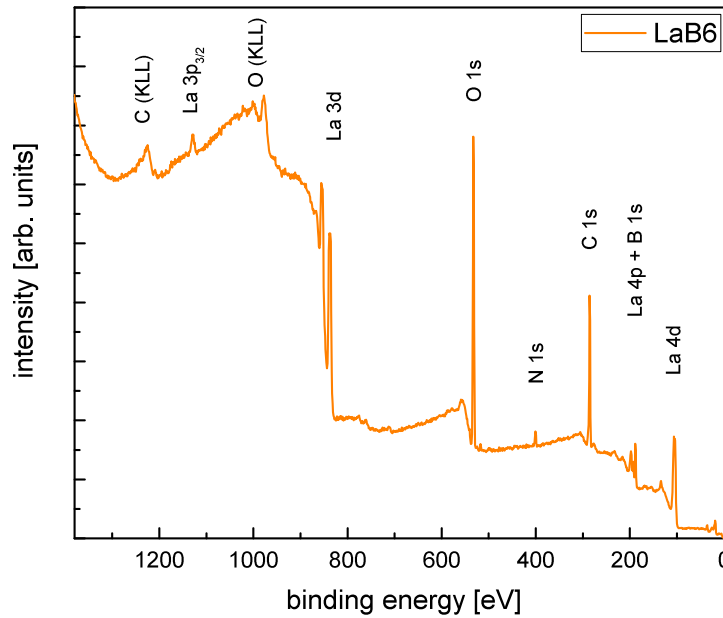
FIGURE 5.4: XPS spectrum of LaB$_6$. Besides lanthanum and boron, surface contaminants containing oxygen and carbon were identified.

The electron current I_e of the emitted electrons from a round surface with radius $r = 1\,\text{mm}$ is then given by

$$I_e = j_e \cdot \pi \cdot r^2 = A_0 \cdot \pi \cdot r^2 \cdot T^2 \cdot \exp \frac{-(\Phi - \sqrt{\frac{e^3 E}{4\pi\epsilon_0}})}{k_B T}. \tag{5.1}$$

However, Eq. (5.1) assumes a uniform surface and does not account for the temperature dependence of the work function.

In addition, the material-specific correction factor is omitted, resulting in the determination of an "apparent emission work function". Nevertheless,

similar measurements performed utilising LaB$_6$ samples in my master thesis yielded results in good agreement with literature values [103]. In order to determine the surface degradation, measurements with a 500 V bias were performed before and after ionisation efficiency measurements at the Offline 1 facility of ISOLDE.
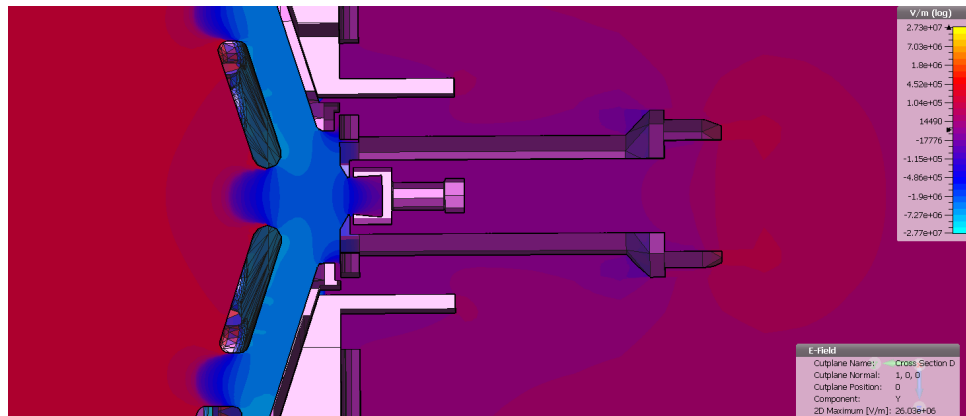
FIGURE 5.5: Electric field map of MK4 for an extraction potential of 1 kV calculated using CST studio suite. The field strength at the center of the ioniser is $\approx 500 \times 10^3$ V/m.

The electron emission for various measurement configurations, determined using Eq. (5.1) as fit function, is shown in Figure 5.6. The top graph shows the electron emission before the use as ion source at the Offline 1 facility with a plugged (red) and an open (black) pre-extraction plate, respectively. The measurement configuration with the plugged hole gave about four times higher electron emission at the same temperature, resulting in an apparant work function of 3.28 eV compared to 3.43 eV.

The increase in work function after the use as an ion source, shown in the bottom half of Figure 5.6, suggests a degradation of the surface over time. Consequently, the measurements performed at 500 V before and after ionisation measurements at the ISOLDE Offline 1 facility show an increase of the work function by 0.41 eV to 3.69 eV. Additionally, the apparent work function decreases with increasing extraction potential to a minimum of 3.49 eV, possibly caused by overcoming space charge effects or a deeper penetration of the extraction field to the ioniser. Uncertainties in the temperature calibration caused by the emissivity of the material were estimated to be smaller

than 10 meV using Gaussian error propagation.
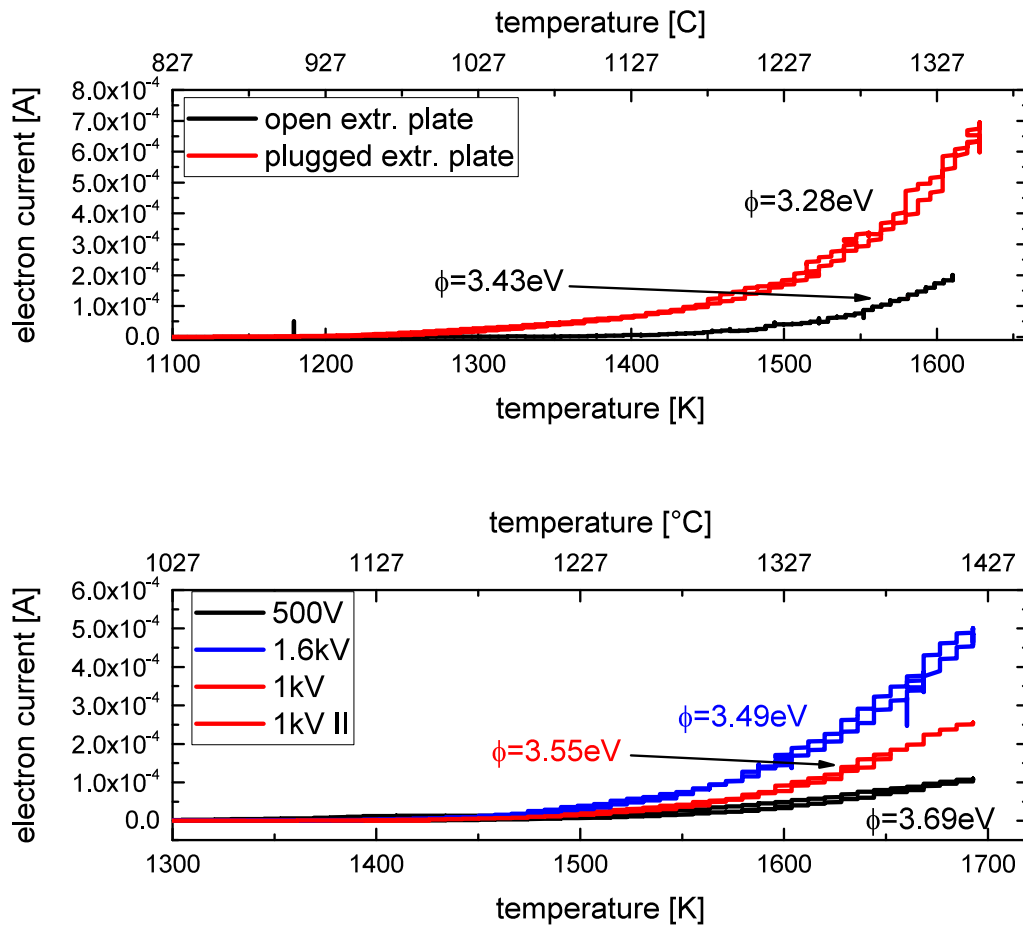
FIGURE 5.6: Electron emission of $SrVO_3$ acquired during a full heating and cooling cycle. Top: Electron emission of $SrVO_3$ at 500 V extraction potential with open (black) and plugged (red) pre-extraction plate before the use as ion source. Bottom: Electron emission with a plugged pre-extraction plate at 0.5 kV (black), 1 kV (red) and 1.6 kV (blue).

For potentials higher than 1.6 keV, sparking between pre-extractor and ion source was observed, prohibiting measurements with even higher extraction potentials. Electron emission from other parts of the ion source such as the transfer line made out of tantalum are unlikely to contribute substantially to the overall current density. This is due to the small area of the heated tantalum transfer line (with a work function above 4 eV [100]) that is exposed to the extraction field. Overall, the apparent work function of $SrVO_3$ can be estimated to be between 3.28 eV and 3.5 eV.

Ionisation efficiencies

Efficiency measurements of the MK4 using a SrVO$_3$ ioniser were performed for the halogens iodine, bromine and chlorine. All samples were prepared by placing a defined amount of solution onto an approximately 5 mm by 5 mm, 6 µm thick tantalum foil. Subsequently, the solvent was evaporated using a lamp as a heat source. The foil with the residual salt containing the halogen was thereafter inserted into a tantalum mass marker tube, which is connected to the transfer line of the ion source and can be resisitively heated independently from the ion source. By comparing the total charge of the respective element deposited in the FC after the separating magnet, the ionisation efficiency can be determined. The transport efficiency of the separator can be estimated by comparing the total beam current before the mass separator with an integrated beam intensity over a full mass spectrum.

In this case, the transport efficiency was estimated to be $\approx$ 100 %, as is common for negative surface ion sources at ISOLDE. In Figure 5.7, the integrated current over time is shown for the halogens chlorine, bromine and iodine, measured at two different occasions. During the first set of efficiency measurements of iodine and chlorine, the ion source was operated at a higher temperature, 1690 °C compared to 1340 °C, resulting in mechanical damage causing the pre-extraction plate to come in electrical contact with the target base. Therefore, the ion source was mounted on a different target base afterwards. In the bottom part of Figure 5.7, the integrated iodine current is shown, measured at 1690 °C of the ion source, where the mentioned ion source failure occurred after about 1.4 h of measurement.

In this case, an efficiency of 10.6 % was determined. In the top part of Figure 5.7, the result of the other ionisation efficiencies are shown and range between 0.1 % and 1.5 %, respectively. While the ioniser seemed intact upon visible inspection, it is suspected that the operation at 1690 °C caused a degradation of the SrVO$_3$ surface ioniser. This is supported by the electron emission measurements discussed above as well as the decrease in iodine and chlorine efficiency. The chlorine efficiency reduced by a factor four, however

it seems likely that chemical processes reduced the overall efficiency additionally, as even with a work function of 3.5 eV an efficiency greater than 1 % is expected.
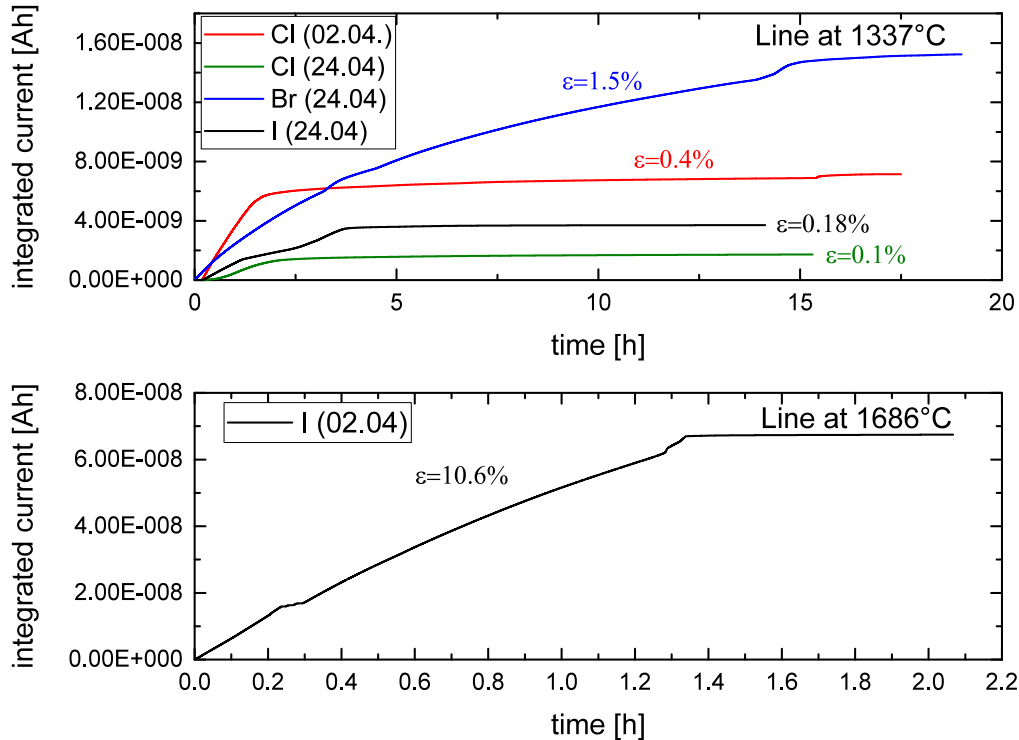
FIGURE 5.7: Integrated current of halogens ionised by a SrVO$_3$ ioniser with measurement dates indicated in brackets. Top: Integrated current for chlorine, bromine and iodine at ion source temperatures of 1340 °C and corresponding efficiencies. Bottom: Integrated current of iodine, measured at 1690 °C.

For bromine and iodine, this seems the case to a lesser degree. Assuming an effective work function of 3.55 eV as determined from the electron emission measurements at a potential of 1 kV (as applied during efficiency measurements) at a temperature of 1337 °C and accounting for a geometrical factor of one third, efficiencies of 2 % for bromine and 0.23 % for iodine are expected, respectively. Those values are in good agreement with the measurement results. In order to reach an efficiency of 10 % for iodine at an ion source temperature of 1690 °C, an effective work function of about 3 eV at 1 kV would be expected, which is about 0.28 eV lower than the work function determined from electron emission at an extraction potential of 500 V.

Overall, it seems possible to reach ionisation efficiencies for halogens comparable to an LaB$_6$ ioniser. However, further investigations of improving the temperature stability e.g. by metal doping as suggested by Jacobs *et al.* [221] might facilitate the use of SrVO$_3$ as surface ioniser. In addition, the production of an ioniser with a defined crystal orientation might further lower the work function of SrVO$_3$, as would be the case for LaB$_6$. However, in terms of stability, efficiency and availability, LaB$_6$ remains the superior choice as surface ioniser for negative ions at this point.

5.2 Alternatives to surface ionisation

5.2.1 VADIS- negative ion operation mode

The VADIS source also known as FEBIAD (**F**orced **E**lectron **B**eam **I**nduced **A**rc **D**ischarge) [178] ion source, described in chapter 3, was originally conceived for the creation of positive ions by electron impact. However, due to the similarity in geometry as well as the rapid availability of the source at ISOLDE, a VADIS source was tested as possible candidate for sputter type generation of negative ions with the production of fluorine beams as a first goal. Instead of accelerating electrons into the anode volume, a VADIS ion source (type VD5) was equipped with a caesium dispenser consisting of caesium chromate (Cs$_2$CrO$_4$).

The transfer line was typically operated at 2000 °C to ensure ionisation as well as to reduce the adsorption of caesium atoms. In order to accelerate caesium ions into the anode volume and facilitate the extraction of negative ions, the anode grid was biased negatively. Atomic species were injected either in molecular form as NF$_3$ via a calibrated leak or from a mass marker tube prepared as described previously. In Figure 5.8, two mass spectra are shown using an iodine mass marker and NF$_3$ gas injection, respectively, to supply precursors for the negative ion species. In case of the iodine mass marker, mainly iodine as well as chlorine and fluorine ions (both likely residuals from previous tests) are visible in the mass spectrum. In the case of

NF$_3$ injection, there are mainly fluorine, but also chlorine and oxygen ions produced in small quantities.
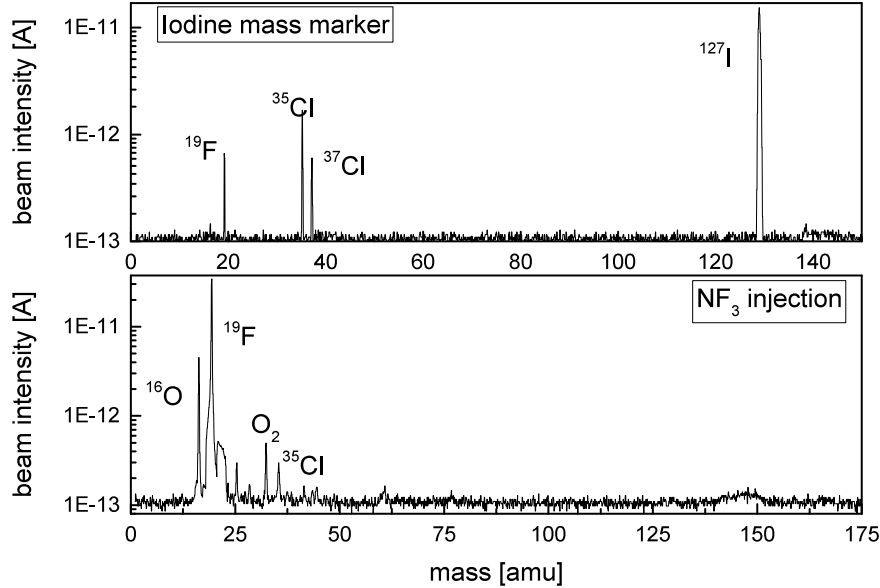
FIGURE 5.8: Mass spectra of the VADIS ion source in negative ion mode with iodine mass marker (top) and NF$_3$ gas injection (bottom). In the top spectrum, mainly halogens are visible with iodine dominating. In the bottom graph, where NF$_3$ was injected, there is additionally oxygen visible as well as a broad peak around 128 u and 147 u, possibly MoOF and MoO$_2$F, respectively.

Additionally, there is a broad peak visible around mass 147 u, likely a fluoride or oxide molecule. The ionisation efficiency was determined by

$$\epsilon_{is} = \frac{I_{ion}}{\epsilon_{transp} \cdot I_{atom}}, \tag{5.2}$$

where I_{ion} is the measured beam intensity, ϵ_{transp} the transport efficiency and I_{atom} the total particle current into the ion source determined by pressure applied to the calibrated leak with a given leak rate, or by the amount of atoms placed into the mass marker tube, respectively.

The transport efficiency was determined by comparing the total ion beam current measured in a Faraday cup before the mass separator with the integrated intensity of a mass spectrum measured in a Faraday cup after the mass separator. For fluorine, which was injected in the form of NF$_3$ through

a calibrated leak with a leak rate of 1×10^{-5} mbar l/s, the efficiency could be determined to be $\approx 2.8 \times 10^{-4}$ % at most.

Overall, although negative ions were successfully generated, the achieved efficiency was below the values typically reached with the surface ion source. Generally, the ion source behaviour was relatively unstable with general trends which were hard to determine. However, high caesium currents as well as ion source temperatures seemed to generate the maximum beam intensity. Furthermore, the ion source settings for maximum efficiency were achieved when biasing the anode grid positive with 2 V, as shown in the top part of Figure 5.9 which indicates that the majority of negative ions were created inside the caesiated transfer line, while the grid potential and ion source magnet only provided a guiding field to optimise the extraction of negative ions.

For the caesium injection, in general two trends were observed, examples of which are shown in the bottom part of Figure 5.9.
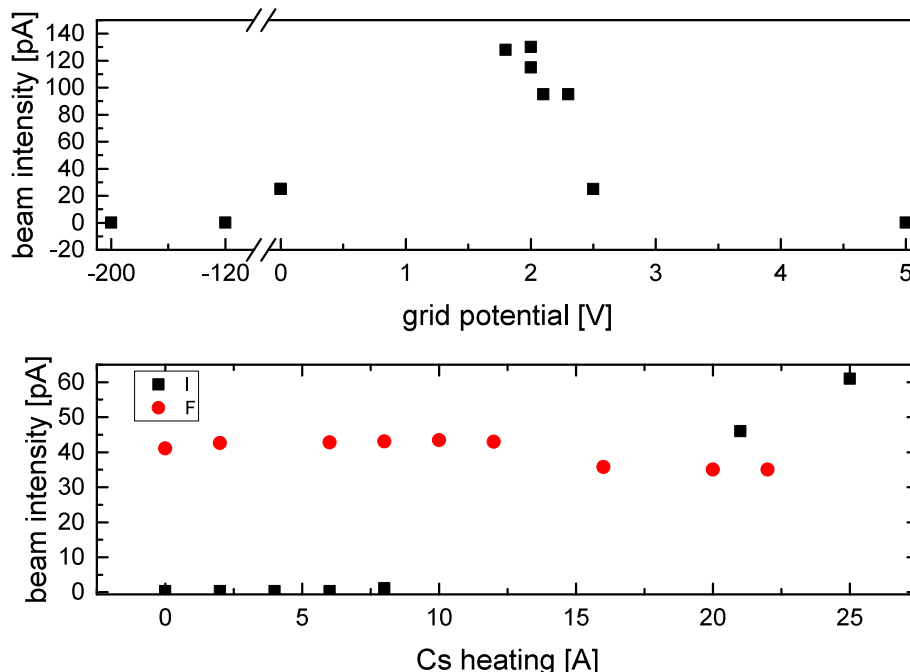
FIGURE 5.9: Top: negative ion beam intensity in dependence of the anode potential. The maximum beam intensity was reached with a small positive bias of about 2 V. Bottom: beam intensity in dependence of caesium dispenser heating. For iodine, the intensity starts to increase at around 10 A, while for fluorine increased caesium diminishes the beam intensity slightly.

In the case of iodine, where the ion source had been mostly free of caesium, the injection of caesium facilitates negative ion production. However, if the maximum of negative ion production is reached, the addition of further caesium to the ion source diminishes the negative ion production, as is shown in the case of fluorine. This might be caused by a saturation of the ion source surface with caesium or increased layer thickness, resulting either in surplus caesium in gas phase changing the gas load and plasma potential in the ion source or an increase in work function of the surface, respectively.

In conclusion, the KENIS ion source seems more promising for the sputter-like generation of negative ions, while surface ion generation on a caesiated tantalum surface does not require a VADIS geometry and can rather be investigated utilising a surface ion source, as discussed in the next section.

5.2.2 Tantalum surface source with Cs oven

Caesium is often used in negative ion sources to contribute by lowering the work function of a surface and thereby increase the production of negative ions. Such is the case for many negative hydrogen ion sources [226, 227] as well as in the sputter ionisation process, as discussed in chapter 2. Measurements utilising the injection of alkalide metals such as sodium and potassium were performed in the 1980s and nineties at ISOLDE yielding no satisfactory results.

Alton *et al.* reported the development of a dual purpose ion source capable of creating positive and negative ions on a metal or caesiated surface respectively, however without reporting on negative ion production efficiencies. In addition, the injection of caesium vapour in tubular hexaboride surface sources has been tested in order to improve the plasma sheath generated by the electrons emitted from the ion source walls [102]. Consequently, the feasibility of a negative surface ion source using cesium vapour injection as an alternative to solid low work function ionisers for the production of negative ions was investigated. An ISOLDE MK1 surface ion source was mounted on a negative ion source target base including pre-extraction plate and per-

manent magnet for electron deflection (for a detailed description of both ion sources see chapter 3). An image of the assembly is shown in Figure 5.10.
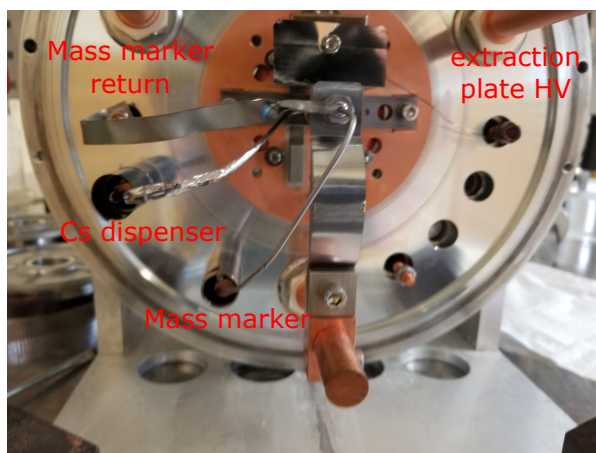
FIGURE 5.10: Caesium surface ion source. Mass marker and electrical return for the heating current are connected in the back of the transfer line, while the caesium dispenser is connected to the front.

The ion source was equipped with a caesium dispenser made of Cs_2CrO_4 connected perpendicular to the extraction end of the ion source capillary. In the top part of Figure 5.11, the negative ion beam intensity is shown in dependence of the heating current of the caesium dispenser. Here, the negative ion beam intensity clearly correlates with the caesium beam intensity and levels off around a heating current of 50 A. In the bottom part of Figure 5.11, the beam intensity in dependence of the ion source heating is shown for two measurements, where the intensity increases with rising temperature.

Two efficiency measurements were performed using bromine mass markers with a charge of 1010 nAh and 1996 nAh, respectively. The transport efficiency was estimated to be 100 % based on a comparison of the total beam current with the integrated current of a full mass spectrum from 1 u to 300 u, with no bromine present before mass marker heating.

The pre-extraction plate was put on a potential of 100 V in order to ensure beam extraction without sparking due to the high gas load of caesium. The integrated current over time is shown in Figure 5.12. After accounting for background transport efficiency, the resulting efficiencies were 8×10^{-3} %

and 0.06 %, respectively. In general, the ion beam was very unstable and beam intensities of negative ions and caesium could not be maintained for a longer duration and ion source and caesium heating had to be readjusted frequently.
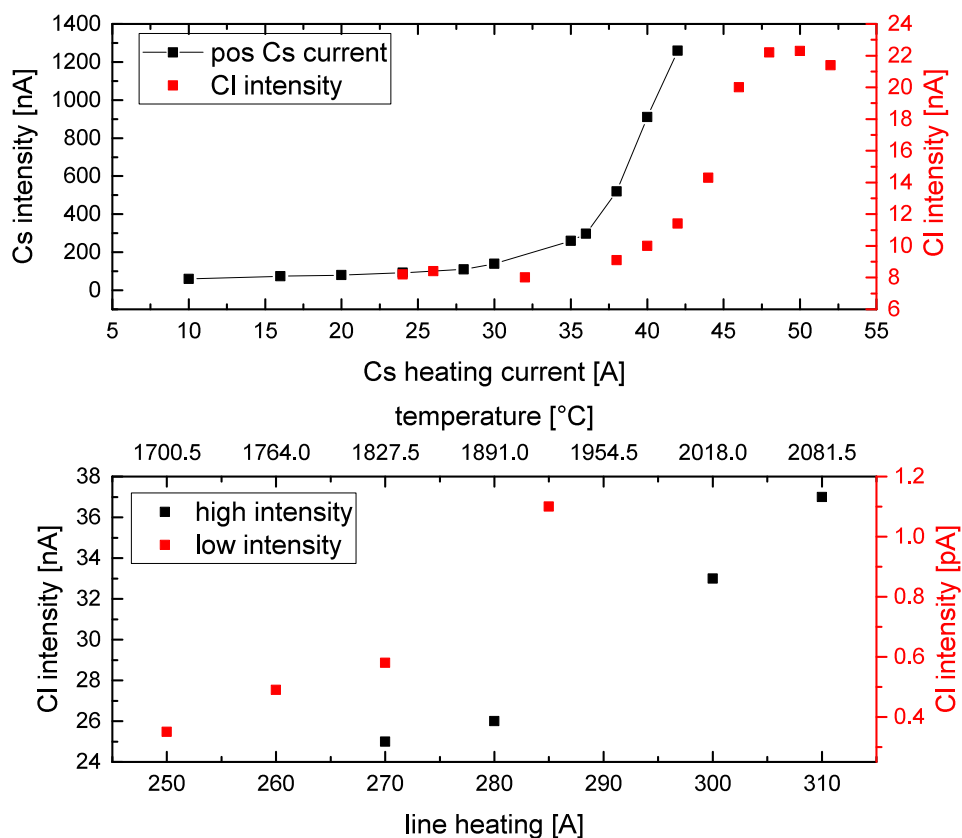
FIGURE 5.11: Top: Intensity of positive caesium ions and negative chlorine ions in dependence of the heating current of the caesium dispenser. Bottom: chlorine beam intensity in dependence of ion source temperature for low and high beam intensities.

This likely contributed to the disparity in the two efficiency measurements and results from the complex interplay of caesium release and adsorption at the tantalum surfaces, where about one monolayer of caesium has been reported to yield optimal performance in terms of lowering the surface work function [228, 229]. In addition, chemical reactions of caesium and other compounds in the ion source capillary such as oxygen released from the caesium dispenser can diminish negative ion production, similarly to the experiments using a VADIS ion source as discussed above.
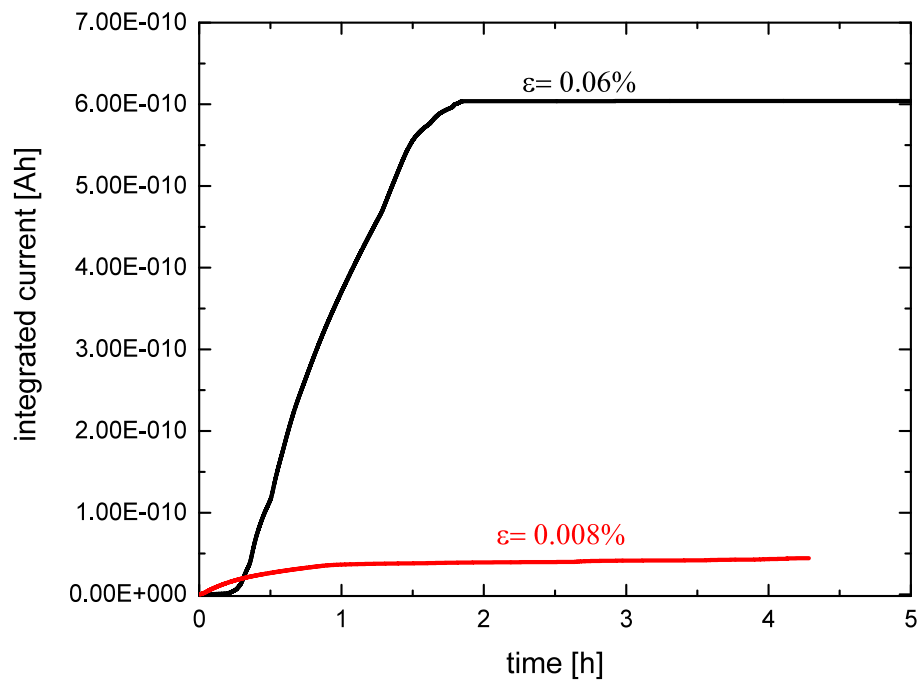
FIGURE 5.12: Integrated beam current in dependence of time
for two bromine efficiency measurements.

5.2.3   KENIS

The KENIS, described in chapter 3, is a sputter type ion source developed
at Oak Ridge National Laboratory for the efficient delivery of negative fluo-
rine beams. The source underwent some initial tests at ISOLDE in the 2000s
where an efficiency of about 1.3 % for fluorine was achieved [230]. However,
no detailed documentation of these tests or the exact ion source configuration
were available. Hence, the KENIS was refurbished once more with the aim to
re-install it to efficiently deliver negative fluorine beams as well as to investi-
gate negative ion production of other elements such as sulphur and oxygen.
Initial tests were performed with caesium delivered to the center of the trans-
fer line via a caesium-dispenser consisting of Cs_2CrO_4. Fluorine gases were
delivered through a calibrated leak with a leak rate of 1.5×10^{-6} mbarl/s
onto which usually around 1200 mbar pressure was applied. In order to de-
liver atomic fluorine, SF_6 and CF_4 seemed favourable in comparison to NF_3
due to higher temperature stability. Additionally, offline tests with the KE-
NIS at Oak Ridge were performed using SF_6, which has the benefit of also

delivering sulphur.

As a first result using the caesium dispenser, a maximum fluorine beam of 240 nA was achieved for a short duration using SF_6, corresponding to an efficiency of 0.6 %. This is reasonably close to the 1.3 % achieved previously at ISOLDE. However, the beam intensity varied strongly and could not be stabilised at these intensities, likely due to similar reasons as observed in the VADIS and tantalum surface ion source tests. In addition, the decomposition of Cs_2CrO_4 in the transfer line resulted not only in the delivery of the caesium necessary for the negative ion production but also in the production of large oxygen beams, as shown in the mass spectrum in Figure 5.13.
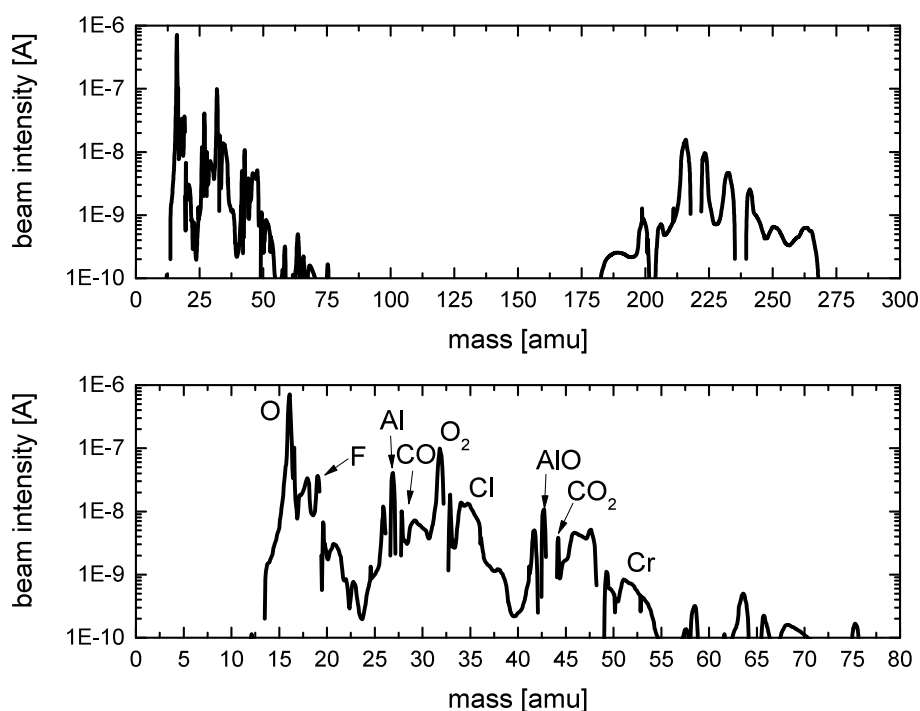
FIGURE 5.13: Top: KENIS mass spectrum in the full mass range using a Cs_2CrO_4 dispenser, where a range of molecular compounds are visible between 180 u and 270 u. Bottom: Zoom in for masses 1 u to 80 u. About 700 nA oxygen beam resulting from the caesium dispenser mask masses of interest, e.g. sulphur as molecular oxygen beam, while about 35 nA atomic fluorine are produced here.

There, about 730 nA of oxygen are produced and about 94 nA on mass 32 u, likely O_2 and sulphur, while the fluorine intensity is only around 35 nA. In addition, a large variety of molecular compounds, i.e. tantalum fluorides

are observed in the mass range of 180 u to 270 u. Especially due to the large beam intensities of oxygen resulting from the caesium dispenser, accurate efficiency measurements of sulphur and oxygen were not feasible in this ion source configuration.

Hence, an alternative method of caesium delivery was designed in form of an external reservoir containing pure metallic caesium mounted to the target as shown in Figure 5.14. The reservoir contains a glas ampoule with 1 g of pure caesium acquired from Sigma Aldrich GMBH. A three-way valve connects the reservoir either to a pre-vacuum pump or a tantalum tube which is connected to the transfer line of the ion source via a feedthrough into the target.

Both the reservoir and the external tantalum tube are heated independently, the reservoir indirectly by a heating coil, the tube resistively, reaching temperatures up to 130 °C.

FIGURE 5.14: KENIS ion source with external caesium reservoir
mounted on the target.

The temperature is limited by the materials used in the reservoir valve as well as the gasket connecting the injection line to the vacuum side of the target unit. On the target base, the injection is electrically insulated from the

target base by a boron nitride insulator to avoid additional current loops. Once target and reservoir are evacuated, the caesium ampoule is crushed by turning a screw. The temperature of the reservoir and external tube are monitored with two K-type thermocouples connected to two multimeters, respectively.

In the top part of Figure 5.15, the beam intensity in dependence of the caesium injection temperature is shown, while on the bottom part the resulting positive caesium beam is depicted. As expected, the negative ion beam intensity initially rises with increasing caesium current. However, in this case the maximum beam intensity as observed in the tantalum surface ion source (see Figure 5.11) does not seem to have been reached yet.
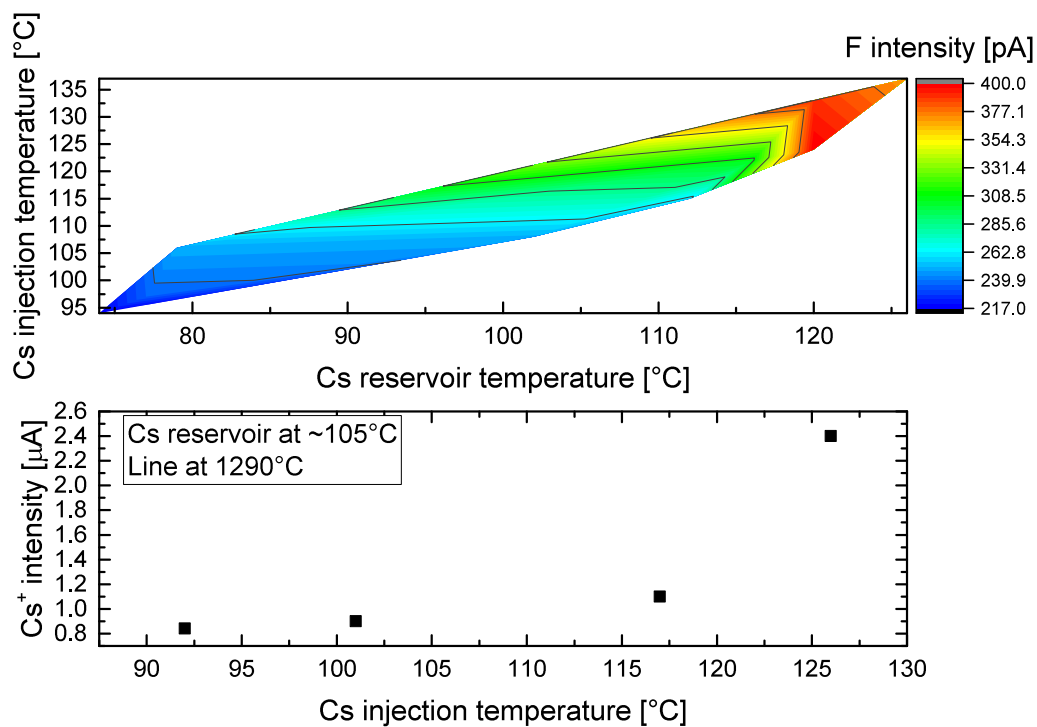
FIGURE 5.15: Top: negative fluorine beam intensity in dependence of caesium reservoir and injection temperature. Bottom: positive caesium beam intensity in dependence of the injection line temperature.

In addition, it was not possible to reach fluorine intensities of more than a few nanoamperes, as shown in Figure 5.16. Although, the ion beam intensity was observed to be more stable as when using the caesium dispenser. Additionally, the drain current on the acceleration grid, which is mainly caused by

caesium ions, was observed to be of the order of a few hundred µA, where usually tens of mA were seen at Oak Ridge [231]. Overall, this indicates that the temperature limit of the external reservoir and injection line in combination with the cold spot at the water cooled target base prohibits the transmission of the necessary amount of caesium. However, the beam intensities seemed more stable in comparison to using the caesium dispenser and the fluorine to oxygen ratio is significantly improved in comparison to the use of the caesium dispenser (see Figure 5.13 for comparison).
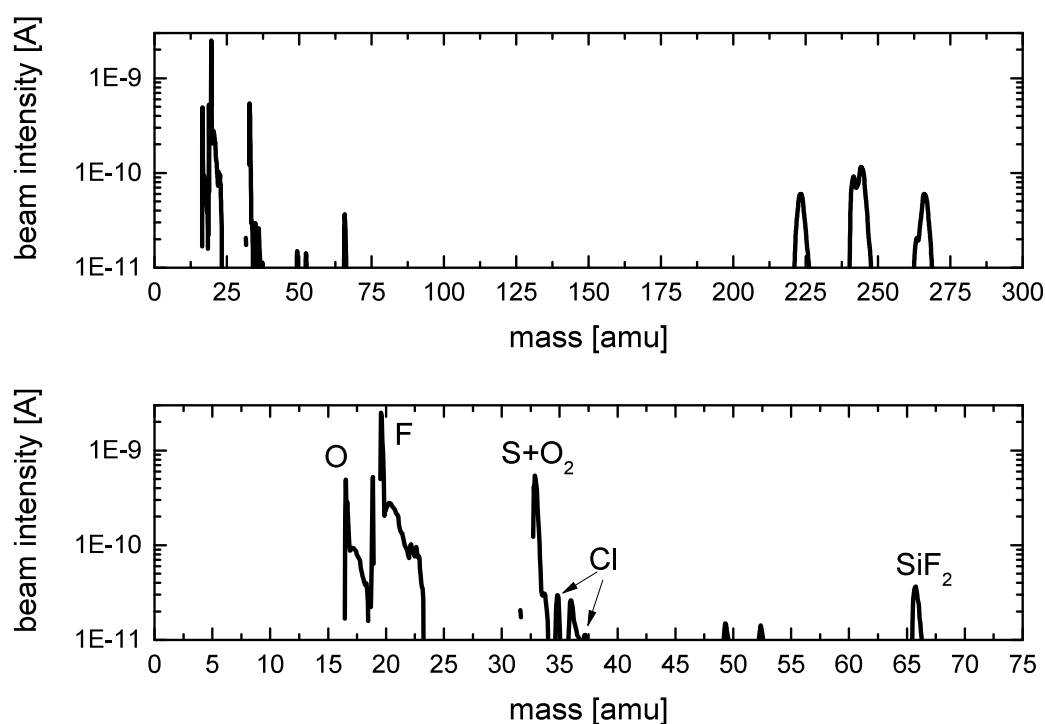
FIGURE 5.16: Mass spectra of the KENIS utilising the external caesium reservoir with SF_6 injection. Fluorine is the dominant component, while also oxygen is produced as well as several molecular species at masses above 220 u, likely comprised of fluoride, oxide and sulfide compounds.

Figure 5.17 shows the negative ion beam intensity in dependence of the caesium beam energy, where the maximum is reached at around 300 V, after which it stagnates or even decreases slightly. The optimum ion current was then found using a -300 V bias on the acceleration grid and -250 V on the ioniser cone, respectively. Overall, these ion source parameters were found to be similar to those reported [189, 190]. The lifetime of the KENIS seems

to be mainly limited by the circular insulators used to mount the acceleration grid and the ioniser cone, which are in line of sight of the gas flow and coated usually after about three weeks of extensive use of the KENIS source, resulting in a short circuit.
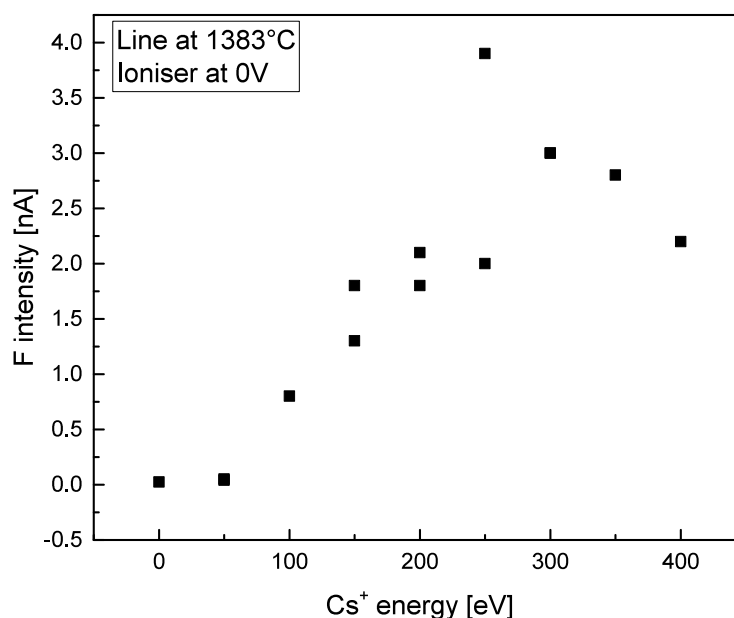
FIGURE 5.17: Fluorine beam intensity in dependence of the accelerator grid voltage. The beam intensity rises to a maximum at a potential of 300 V, after which the intensity drops slightly with one outlier at 250 V.

Furthermore, it was discovered that a new batch of calibrated leaks used for the injection of the reactive fluoride gases clogged over time, reducing the transmitted gas load by an unknown factor until no gas was transmitted.

This was discovered during the tests of the KENIS source as well as the VADIS source and applied to all gas leaks, where fluoride compounds where injected. Hence, tests using CO_2 injection at that stage were inconclusive since it is not clear if low ionisation efficiency, breakup or gas transmission were responsible for the lack of a measurable effect. In addition, efficiencies values determined using these leaks must be considered as lower limits, especially after longer usage of the ion source.

In Figure 5.18, scanning electron microscope images of a used and a new gas leak cut open vertically, are shown.
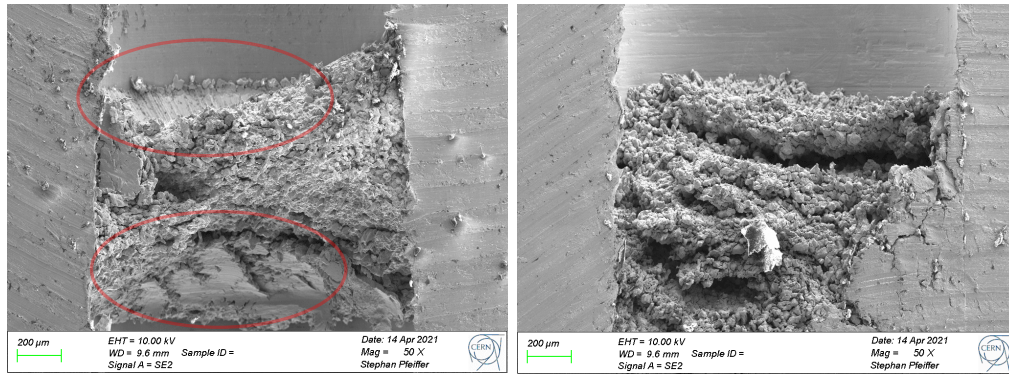
FIGURE 5.18: Left: clogged leak used for NF_3 injection. Right: new, unused leak. The smooth surfaces indicated by red marking might indicate sintering, while the new leak shows a higher porosity. Courtesy of S. Stegemann and S. Pfeiffer.

The smooth surfaces of the used gas leak could suggest a sintering of the powder used in the gas leak. This is likely caused by either unwanted heat conductance from the ion source heating or a breakdown of the boron nitride insulator resulting in a current resistively heating the gas leak or other reaction products being deposited onto the leak.

For future tests, an increased temperature limit on the caesium reservoir and injection should yield higher caesium currents and in consequence higher fluorine efficiency. This, would then also allow further investigation of the ionisation efficiencies of other elements such as sulphur, oxygen and carbon, which currently can not be delivered as negative ions at ISOLDE. With the KENIS now being re-established, these studies are expected to take place in the near future.

Chapter 6

Photodetachment threshold spectroscopy

6.1 The electron affinity of astatine

The determination of the electron affinity of astatine at CERN-ISOLDE by means of laser photodetachment threshold spectroscopy (described in chapter 2) is reported in publication C. In the following, the main results of this work [51] are summarised.

Astatine, element 85, is the rarest naturally occurring element on earth [232], for which the half-life of its longest lived isotope , ^{210}At, is about 8.3 h. The naturally occurring isotopes ^{215}At and $^{217-219}$At are produced via the β-decay of radium, which in turn results from the natural alpha decay chains of uranium ($_{92}$U) and thorium ($_{90}$Th) [233]. Together with the super-heavy element tennessine ($_{117}$Ts), astatine is one of two elements in the group of the halogens for which the EA had not been experimentally determined, with theoretical predictions pointing to an EA of astatine around 2.4 eV, as shown in table 6.1. In addition, isotope ^{211}At is of considerable interest as an agent for targeted alpha therapy in cancer treatment [234, 235, 236, 237]. Knowledge of the fundamental properties of astatine such as the EA, and the first ionisation potential (IP), for which a value was reported for the first time in 2013 [238], are important benchmarks for computational chemistry to predict its chemical behaviour within compounds.

The determination of the EA of astatine was performed at CERN-ISOLDE,

TABLE 6.1: Overview of the calculations of the EA of At utilising different methods. In the last row the experimental value determined in this work is given for comparison.

Method	EA [eV]	Ref.
CBS-DC-CCSDT(Q)+Breit+QED	2.414(16)	[51]
MCDHF+SE corr.[a]	2.38(2)	[239]
MCDHF	2.416	[240]
DC-CCSD(T)+Breit+QED	2.412	[241]
MCDHF+Extrap.+Breit+QED [b]	2.3729(46)	[242]
CBS-DC-CCSD(T)+Gaunt+QECBS-DC-CCSD(T)+Gaunt+QEDD	2.423(13)	[243]
Experiment	2.41578(7)	this work

[a]Multiconfigurational Dirac-Fock (MCDF) results corrected using experimental data.
[b]MCDF results extrapolated to complete active space limit

where the GANDALPH photodetachment detector was coupled to the GLM beamline. Both ISOLDE and the GANDALPH detector are discussed in detail in chapters 3 and 4, respectively. For this work, astatine isotopes were produced through proton-induced nuclear spallation reactions of ^{232}Th nuclei, and were subsequently ionised in an ISOLDE type MK4 negative surface ion source as described in chapter 3. According to the Saha-Langmuir equation, the expected ionisation efficiency of astatine utilising an ioniser material with a 2.6 eV to 2.7 eV work function is in the range of 3.5 % to 7 %. Combined with a geometrical efficiency of about 30 % in the source, the expected ionisation efficiency is of the order of 2 %.

The measured yield of astatine isotopes is shown in the inset of Figure 6.1 together with a predicted in-target production, produced by J.P. Ramos using the FLUKA 2017 Version 1.0. It is to be noted that the in-target production only accounts for the isotope inventory resulting from the cross section of the reaction of the 1.4 GeV proton projectiles with the target material. Hence, transport, diffusion and ionisation efficiency have to be taken into account to compare with the measured beam intensity. The released fraction of astatine isotopes in dependence of the half-life, shown in Figure 6.1 indicates that for isotopes with a half-life lower than 100 s the release drops sharply, while it increases to up to 3 % for elements with longer lifetimes. For those long-lived isotopes, the combined release and ionisation efficiency can be estimated to

be around 2 %, indicating a 100 % release efficiency for those isotopes when taking into account the expected ionisation efficiency of around 2 %.
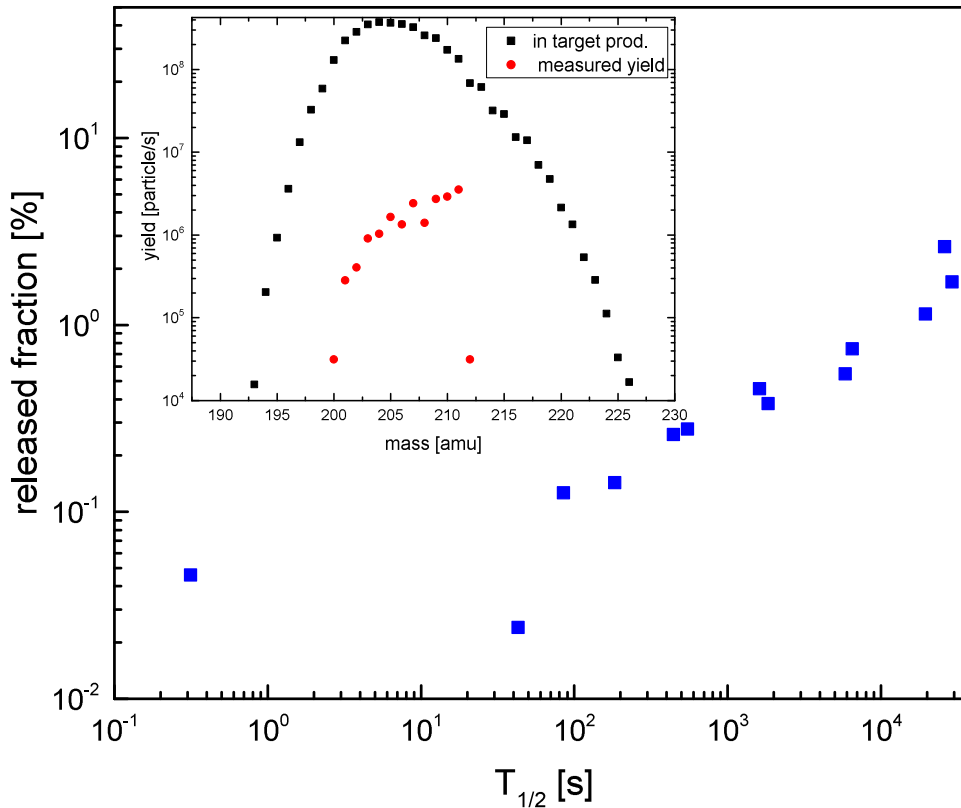
FIGURE 6.1: Fraction of measured particles per second compared to predicted in-target production as a function of the half-life of the respective isotope. Inset: Theoretical in target production yields predicted via FLUKA and extracted particles per second measured on a Faraday cup. Simulation values courtesy of J.P. Ramos.

The beam of ^{211}At anions was transported into the GANDALPH detector, where laser photodetachment threshold spectroscopy as described in chapter 2 was performed in co- and counter-propagating geometry. The photon energy was scanned over the range of 2.384 eV to 2.53 eV (490 nm to 520 nm) with a bandwitdth of typically 12 GHz.

In At$^-$, as in all halogens, the electron is detached from a p-state, here $6p^6\,^1S_0$, where no term splitting or excited states are present due to the closed atomic shell. Close to the threshold, the angular momentum of the outgoing electron will then be $l = 0$ due to the selection rules ($\Delta l = \pm 1$) and the centrifugal barrier preventing the emission of a d-wave electron ($l = 2$), as

discussed in chapter 2. However, the ground state $6p^5\ {}^2P_{3/2}$ of the ^{211}At atom with a total angular momentum of $J = 3/2$ and nuclear spin $I = 9/2$, is split into four hyperfine levels, which were measured with high precision by Cubiss *et al.*[244].

With this information, the energy dependence of the cross section for photodetachment of astatine near the threshold can be described by

$$\sigma(E_{\mathrm{ph}}) = a + b \sum_{F=3}^{6} (2F+1)\sqrt{E_{\mathrm{ph}} - (\mathrm{EA} + E_{\mathrm{hfs},F})}\ \Theta\big(E_{\mathrm{ph}} - (\mathrm{EA} + E_{\mathrm{hfs},F})\big)$$

(6.1)

where $\Theta(E - (\mathrm{EA} + E_{\mathrm{hfs},F}))$ is the Heaviside function and $E_{\mathrm{hfs},F}$ is the energy of the hyperfine levels of the ^{211}At atomic ground state, differing by less than 23 µeV between the contributing levels. Figure 6.2 shows the measured neutralisation cross section $\sigma(E_{\mathrm{ph}})$ as a function of the photon energy, corrected for the Doppler shift, for the sum of all threshold scans with co-propagating ion and laser beams. The data analysis was performed using Python Spyder 2.3.8. Data obtained from the scans of co- and counter-propagating laser and ion beams were binned with a bin width of about 60 µeV. This value is in the order of the laser bandwidth. The binned data points were subsequently fitted using Eq. 6.1. Variations in the bin width and selected data range were investigated and resulted in changes in the final EA value smaller than the statistical error. The experimental data and python script used for the final data analysis can be found at https://zenodo.org/record/3924371. The statistical error of the measurement is dominated by the laser bandwidth of 12 GHz, corresponding to 50 µeV. The contribution to the statistical uncertainty from all other effects are smaller than 0.1 µeV, and can hence be neglected. Systematic errors arise due to instabilities of the ion beam energy and the determination of the photon energy.

The combined systematic error of photon energy and beam energy is estimated to be smaller than 20 µeV by comparing two reference measurements of stable ^{127}I which were performed before and after the experiment on astatine, under the same experimental conditions. Including both systematic and statistical errors, the resulting value of EA(At), calculated by the geometric
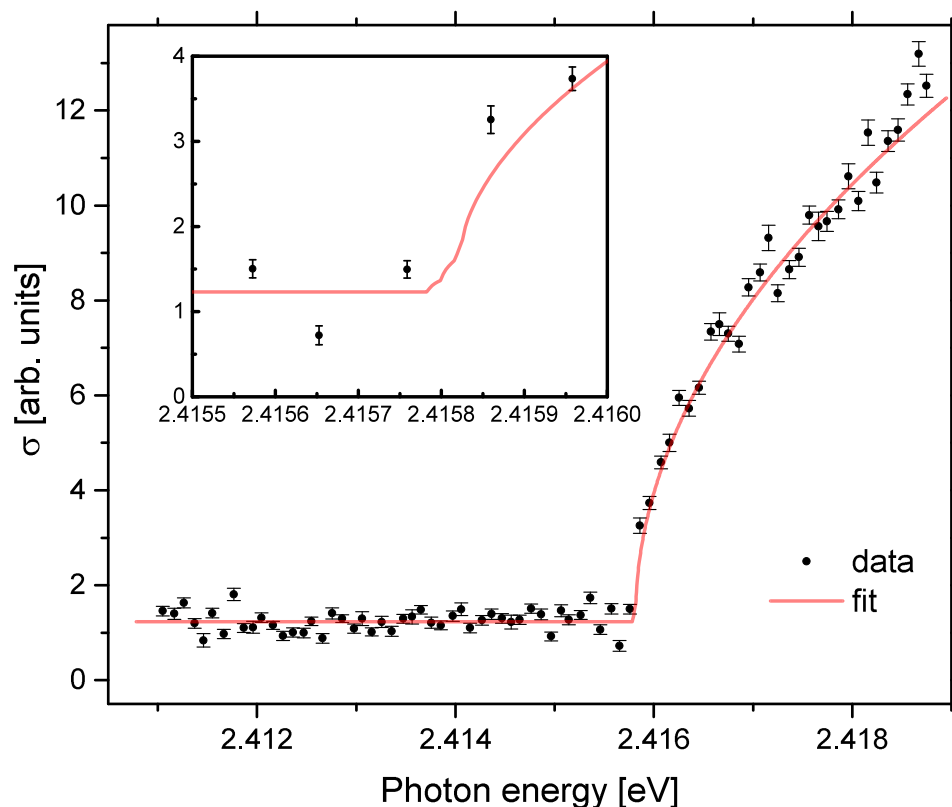
FIGURE 6.2: Threshold scan of the photodetachment of astatine. The neutralisation cross section is measured as a function of the photon energy. The data points are the experimental measurements with one standard error represented with error bars, and the solid line is a fit of Eq. 6.1. The onset corresponds to the EA of ^{211}At. The inset shows the threshold region, where the onsets correspond to the individual hyperfine levels of the groundstate of the neutral atom, which are not resolved here due to the bandwidth of the laser.

mean of the photodetachment thresholds measured in the co- and counter-propagating geometries, was determined to be 2.415 78(7) eV.

In addition to the measurements, state-of-the-art calculations of the electron affinities of astatine and of its lighter homologue, iodine (^{127}I) were carried out by the group of A. Borschevsky of the Van Swinderen Institute for Particle Physics and Gravity at the University of Groningen. The results for iodine were used as a benchmark and agreed with the experimentally determined value of 3.059 046 3(38) eV [245] within 0.004 eV. For astatine, an EA of 2.414(16) eV was predicted, which is in excellent agreement with the experiment. The calculations were carried out with the DIRAC15 program package [246] using the single reference coupled cluster approach in the framework

of the Dirac-Coulomb Hamiltonian (DC-CCSD(T)), thereby performing a full relativistic many-body treatment that also includes Breit and QED effects.

From the EA, a better understanding of astatine's chemistry can be derived through the deduction of the electronegativity, softness, hardness, and the electrophilicity index, which are shown in table 6.2, together with their respective definitions.

TABLE 6.2: Values and definitions of chemical properties of astatine derived from the EA and IP.

Property	Definition	Value
Electron affinity	EA	$2.415\,78(7)\,\mathrm{eV}$
Ionization energy	IP	$9.317\,51(8)\,\mathrm{eV}$[238]
Electronegativity	$\chi_\mathrm{M} = \frac{\mathrm{IP+EA}}{2}$	$5.866\,65(7)\,\mathrm{eV}$
Hardness	$\eta = \frac{\mathrm{IP-EA}}{2}$	$3.450\,87(7)\,\mathrm{eV}$
Softness	$S_\mathrm{M} = \frac{1}{2\eta}$	$0.144\,89(2)\,\mathrm{eV}^{-1}$
Electrophilicity	$\omega_\mathrm{e} = \frac{\chi_M^2}{2\eta}$	$4.986\,80(16)\,\mathrm{eV}$

As ^{211}At is a promising candidate for targeted alpha therapy, these properties have direct implications for its use in cancer treatments. Most of ^{211}At-radiopharmaceuticals suffer from *in vivo* release of astatide (At$^-$) and the development of radiosynthetic procedures so far is severely hampered by the limited knowledge of the chemical properties of this element. Hence, the new information about astatine's chemical properties will be of great importance in the development of innovative radio-labelling protocols.

6.2 Novel techniques for the investigation of negative ions

The measurements of the electron affinities of ^{128}I [50] and At (see publication C) successfully demonstrated that laser photodetachment threshold spectroscopy is a viable method for the determination of EAs of radioisotopes. However, for future measurement campaigns, e.g. the determination

of the EAs of the actinides and super-heavy elements, it is desirable to increase the efficiency of the method in anticipation of low production yields.

Isotope shift of the electron affinity of chlorine.

As discussed in chapter 2, the isotope shift in the electron affinity, in particular the specific mass shift, can serve as a sensitive benchmark for theoretical models describing electron correlation in atoms. In 1995, Berzinsh *et al.* experimentally determined the isotope shift of the electron affinity in the two stable chlorine isotopes (^{35}Cl and ^{37}Cl) to be 0.22(14) GHz; a value of similar size but opposite sign as the theoretical prediction provided in the same publication [70]. Carette *et al.* [247] resolved this discrepancy using an multi-configuration Hartree-Fock (MCHF) approach, resulting in an isotope shift of 0.203(72) GHz, with a precision which significantly exceeds the experimental accuracy.

Hence, the measurement of the isotope shift in the EA of chlorine was proposed at ISOLDE, utilising the capability to investigate an extended range of chlorine isotopes, limited only by the negative ion yields of the respective isotopes, with high precision (see proposal D). As detailed in the proposal E, in order to achieve the necessary experimental accuracy, a laser with a bandwidth in the order of 100 MHz at a wavelength of 345 nm is required. This laser radiation will be produced by a cw-seeded pulsed dye amplifier. The negative ion production efficiency via the MK4 negative surface ion source is expected to be around 10 %, while chlorine yields from a niobium foil target are expected to be in the order of 1×10^7 ions/µC for the radioisotopes ^{38,39}Cl [248]. This measurement campaign has been endorsed by the **I**solde and **N**eutron **T**ime-of-flight **C**ommittee (INTC) and is listed as experiment IS643, but can not be scheduled before 2022 due to infrastructure upgrades at ISOLDE prohibiting experiments using negative ions [249].

The electron affinity of polonium

The measurement of the EA of polonium was originally proposed in combination with the determination of the EA of astatine [250], however it has not

been realised yet. Since the EA of polonium is predicted to be around $1.4\,\mathrm{eV}$ [251], the negative surface ionisation efficiency for polonium is not expected to be sufficient for this measurement with about two to three orders of magnitude lower yields than in the case of astatine. However, yields of up to about $2 \times 10^7\,\mathrm{ions/\mu C}$ have been reported from UC_x targets for beams of the positive isotope $^{204}Po^+$ [252]. Hence, negative ions of polonium are planned to be produced by a charge exchange process as described in chapter 2, utilising the charge exchange cell at the **C**ollinear **R**esonance **I**onisation **S**pectroscopy (CRIS) setup [52]. The negative ion yield of the charge exchange process for polonium will be tested in a series of off-line experiments using oxygen or tellurium as homologous of polonium. This study has been approved as a Letter of intent (see proposal F) by the INTC with six shifts recommended during CERNs Run 3 [117].

Photodetachment spectroscopy in an MR-ToF device.
Generally, one of the disadvantages of laser photodetachment with sparsely produced radioisotopes is the loss of all ions which are not photodetached, since those are deflected into a Faraday cup or CEM. Hence, for radioactive negative ions, the use of an MR-ToF device was proposed, where negative ions can in principle be trapped with little losses for thousands of revolutions corresponding to tens of miliseconds trapping time, mainly limited by collisions with residual gas. This not only increases the photodetachment yield by allowing multiple laser-ion interactions but also enables alternative measurement approaches such as ion depletion measurements, similar to methods used in storage rings [253].

Consequently, a measurement campaign was initiated during CERN's long shutdown 2 (LS2) to demonstrate the feasibility of performing high precision photodetachment spectroscopy in an MR-ToF device. As a first proof-of-principle experiment, the measurement of the isotope shift of the EA of chlorine is envisioned, additionally demonstrating the capability of performing this measurement with high precision in anticipation of the on-line experiment at ISOLDE (see proposal E), which are expected earliest in 2022 [249].

Apart from demonstrating the technique, the experimentally known isotope shift of the stable isotopes ^{35}Cl and ^{37}Cl shall be determined with higher precision than the value of $0.22(14)$ GHz achieved by Berzinsh *et al.*[70]. Furthermore, a sample of the long-lived isotope ^{36}Cl has been prepared, the foreseen use of which will be discussed in section 6.2.3.

6.2.1 GANDIS

In order to enable negative ion experiments in a MR-ToF, a negative ion source was designed and coupled to the MIRACLS proof-of-principle setup, as mentioned in chapter 4. Initially planned for the purpose of testing the GANDALPH detector in my master thesis [103], the **GAND**ALPH **I**on **S**ource (GANDIS) was adapted and enhanced for direct connection to the MIRACLS setup. GANDIS, shown in Figure 6.3 consists of an ISOLDE target unit coupled to a beamline for ion extraction and transport.

The target unit is placed on a coupling table and then connected to a vacuum cross via an adapted DN100 CF vacuum flange. In order to electrically insulate the target unit, the coupling table is mounted on plastic rods and insulated against the vacuum chamber via a *Lesker CFT60V4006A* vacuum tube with a ceramic spacer. The target unit is a negative surface ion source (MK4) with a tubular LaB$_6$ ioniser, as described in chapter 3. The ion source is heated up to $1500\,^{\circ}$C by a DC $15\,$V$/400\,$A power supply, biased to the extraction potential of up to $-450\,$V. The extraction voltage is limited to $500\,$V by the insulation of the heating supplies and the biasing capability of the Paul trap in the MIRACLS setup but can easily be extended with the integration of a separation transformer.

The element of interest, here chlorine, is prepared in a tantalum capillary ("mass marker") in which a sample of stable isotopes is placed in the form of KCl salt and evaporated by resistively heating the capillary with two DC $52\,$V$/30\,$A power supplies operated in parallel. The ion beam extraction is performed via the pre-extraction plate of the MK4 ion source, which is set to a potential of $700\,$V in order to increase the extraction efficiency. Following
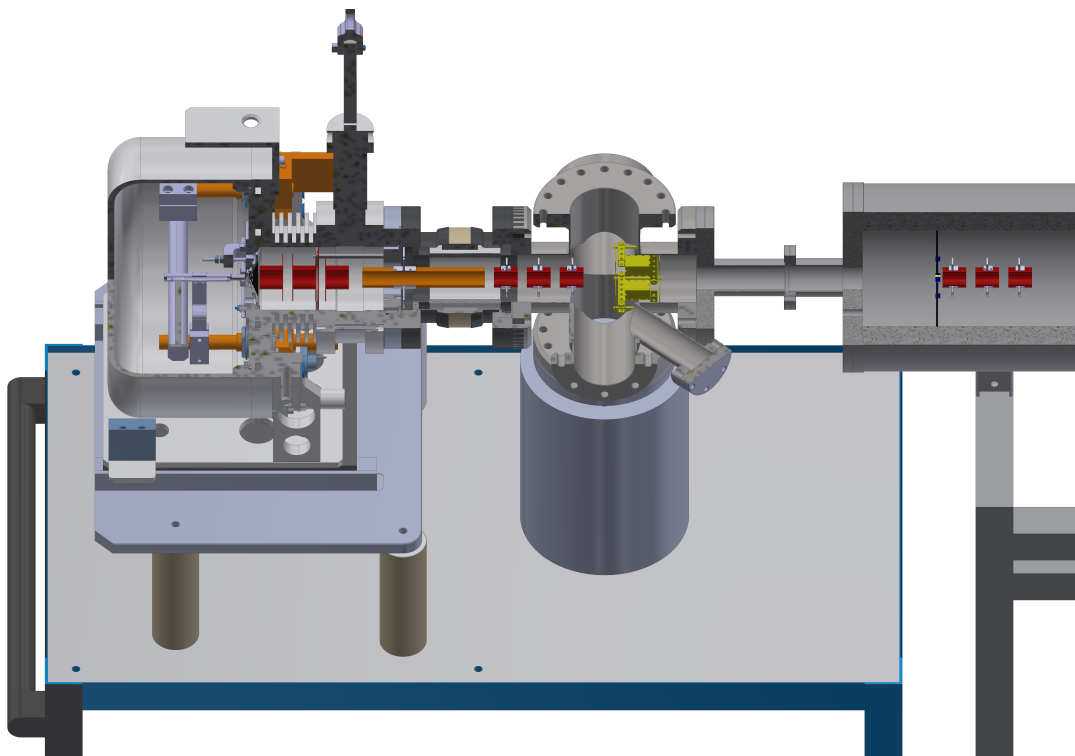
FIGURE 6.3:   GANDIS ion source and beamline without
quadrupole mass filter (QMF). The target unit is insulated
against the laboratory ground using plastic and ceramic insu-
lators (beige). Negative ions are extracted from the target util-
ising its pre-extraction plate (black). Following the extraction,
the ion beam is transported towards the MIRACLS beamline
utilising three Einzel lenses (red), a drift tube (orange) and an
x-y steerer (yellow).

the extraction, the ions pass through several ion optical elements including

two Einzel lenses separated by a drift tube. The drift tube is placed at the

coupling point between target and vacuum chamber in order to shield the

ion beam from a focussing effect resulting from the flange to which the ion

source is coupled. Following the second Einzel lens, a pair of electrostatic

steerers in the x- and y- directions is placed just before the beam enters a sec-

ond vacuum chamber, where a QMF necessary for the separation of ^{36}Cl is

installed together with injection and extraction optics, as discussed in section

6.2.3. For the initial phase of negative ion tests at MIRACLS, the QMF was

foreseen to be left out for parallel testing. Hence, simulations were carried

out with only one additional Einzel lens mounted after an aperture in the

second vacuum chamber, as shown in Figure 6.3, while excluding the QMF.

Design and simulations of the beamline was performed using Autodesk In-

ventor to create the 3D CAD model and SIMION 8.1.1.32-2013-05-20 [254] for the ion trajectory simulation.

The starting conditions for the ions were determined by benchmarking the simulation using the ion source emittance at an extraction potential of 30 keV. By comparing with simulations presented in R. Heinke's thesis [187], where an an emittance around $2\,\pi$ mm mrad was determined with the same source geometry, the initial ion beam conditions in the GANDIS ion source were adjusted to achieve an emittance of $1.92\,\pi$ mm mrad at 30 keV. Subsequently, the ion beam energy was reduced to the value of 450 eV, as used in the experiment.

The GANDIS simulations were then run with these particle properties, shown in table 6.3 and the potentials detailed in table 6.4 for the injection into the MIRACLS beamline.

TABLE 6.3: SIMION parameters for the particle creation in GANDIS.

Property	Distribution	Value
Mass	single value	35 u
Charge	single value	-1 e
Source position	cylinder distribution	$r = 1.75$ mm, length= 1 mm
Azimuth angle	Gaussian distribution	Mean: 270°, St. dev.: 37.79°
Elevation angle	Gaussian distribution	Mean: 37.79°, St. dev.: 37.79°
Kinetic energy	uniform distribution	0.001 eV to 1 eV

In Figure 6.4, the beam trajectory through the GANDIS beamline is shown where about 60 % of the beam is transmitted. The main contribution to the ion loss in GANDIS is due to stripping at apertures, resulting from the humble emittance of the ion beam which in turn is caused by the low beam energy. In addition, the vacuum chamber that will house the QMF was left empty and acted as a 400 mm long drift section. Higher transmission could have been achieved if additional focusing elements were placed in here. The optimised potentials resulting from the simulations are given in table 6.4. The resulting beam exiting the GANDIS beamline was then used as a starting point to determine the injection efficiency of the negative ion beam into

the Paul trap, as shown in Figure 6.5.
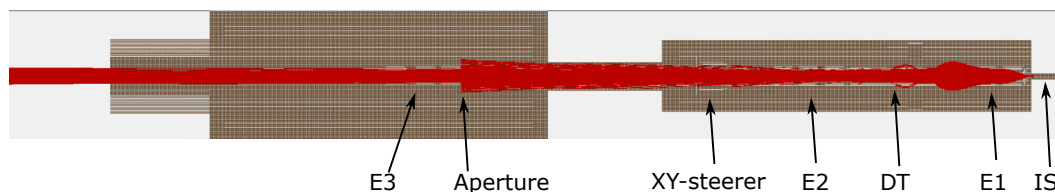
FIGURE 6.4: Simulation of GANDIS extraction. Ions are created at the exit of the ion source capillary (far right) and then transported towards the end of the beamline (left) via Einzel lenses and a steerer box.

As in the case of GANDIS, most ion losses occur at apertures or ion optics with small diameter, as a consequence of the beam size. The total ion beam
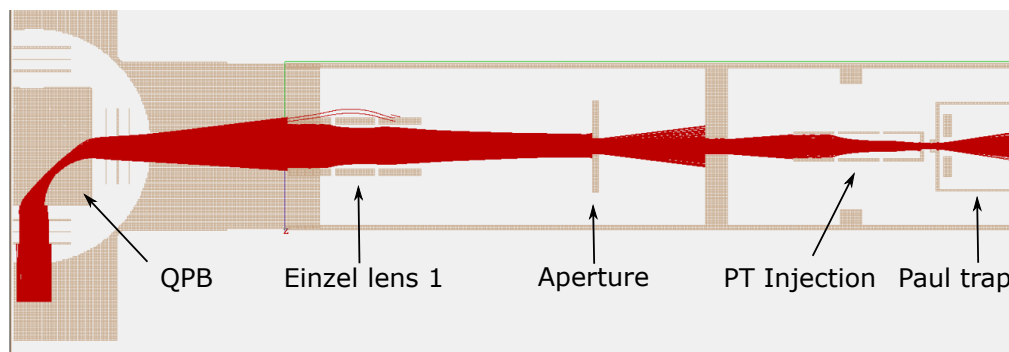
FIGURE 6.5: Simulation of Paul trap injection. Ions coming from the GANDIS beamline (bottom left) are bent by a quadrupol bender (QPB), where they are focussed into the Paul trap using an Einzel lens and additional injection optics.

transmission from GANDIS into the Paul trap was assessed to be around 30 %. For the initial trapping and transmission tests, it was ultimately decided to further shorten the ion source beamline to simplify the setup in the laboratory space and facilitate parallel testing of the QMF in its designated vacuum chamber. In turn, a lower ion beam transmission and tuning capability due to reduced ion optical elements was accepted and it was attempted to compensate this loss by increasing the ion beam intensity. In this simplified version, shown in Figure 6.6, the steerer box was left out and another DN100 vacuum T-chamber was connected directly, leaving only the two first Einzel lenses to ensure beam transport into the MIRACLS beamline. In this

second chamber, a pneumatically retractable plate was installed and used as a simple FC to measure the ion beam intensity.

TABLE 6.4: Simulated potential values for GANDIS compared to values used in testing.

Electrode	Simulation	actual
Ion source bias (IS)	$-450\,\text{V}$	$-450\,\text{V}$
Extractor (EX)	$700\,\text{V}$ or $0\,\text{V}$	$700\,\text{V}$
Einzel lens 1 (E1)	$1020\,\text{V}$	$1035\,\text{V}$
Drift tube (DT)	$0\,\text{V}$	$0\,\text{V}$
Einzel lens 2 (E2)	$60\,\text{V}$	$121\,\text{V}$
XY-steerer	$0\,\text{V}$	not used
Einzel lens 3 (E3)	$230\,\text{V}$	not used

The ion source was usually operated in a way that a beam intensity of tens of nanoampere was measured on the FC plate, resulting in a beam intensity of about $1\,\text{nA}$ measured in the FC before the Paul trap. This corresponds to
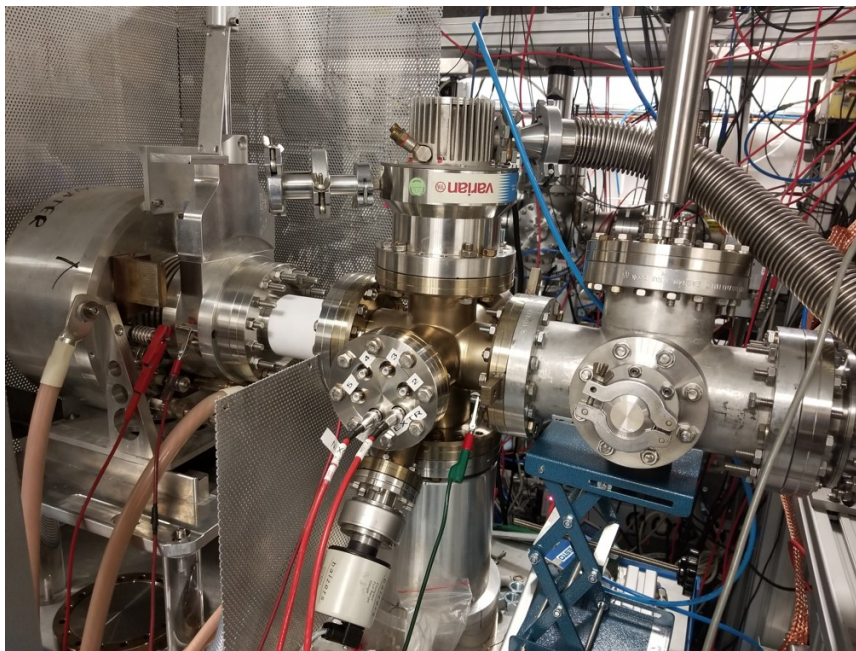
FIGURE 6.6: GANDIS ion source and beamline in the MIRACLS laboratory.

a transmission of typically 1 % to 10 % between the two FCs, while the same
beam intensity was injected into the Paul trap when using the positive elec-
tron impact ion source of MIRACLS. The injection and trapping efficiency of
the Paul trap was estimated to be in the order of 0.1 %, as discussed in the
thesis of L. Fischer [209].

Initial tests of the GANDIS beamline in this configuration were performed
using a positive potassium ion beam, by coupling a positive potassium sur-
face ion source (described in chapter 3) to the GANDIS beamline. After suc-
cessfully transmitting the potassium beam to the end of the MIRACLS beam-
line, the setup was configured for negative ion beams by switching polarity
of the ion optical elements and installing the negative ion source in its basic
version described above. Subsequently, negative chlorine ions were injected
into the setup and successfully transmitted up to the front of the MR-ToF, as
shown in a time of flight spectrum in Figure 6.7.
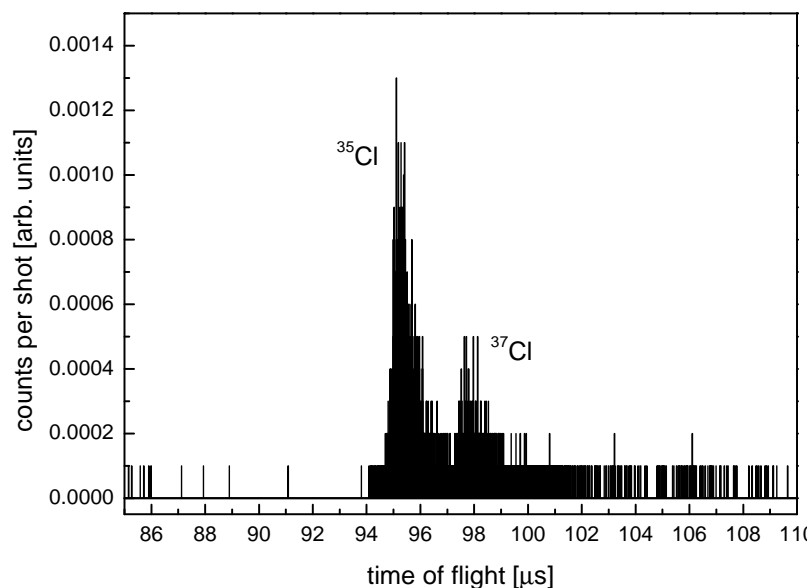
FIGURE 6.7: Time of flight spectrum of negative chlorine iso-
topes, ^{35}Cl and ^{37}Cl.

However, this was achieved by simply chopping the beam via switch-
ing of an electrostatic deflector. The cooling and bunching in the Paul trap
proved to be challenging due to repeated failures of power supplies, ion op-
tics and vacuum devices in and around the Paul trap, which are yet to be

fully resolved.

6.2.2 Neutral particle detection at MIRACLS

In order to perform photodetachment spectroscopy, a neutral particle detector similar to the one used in GANDALPH has to be placed downstream of the MR-ToF device. Consequently, further SIMION simulations of the injection into the MR-ToF and the neutral particle detection were carried out by F. Maier of the MIRACLS collaboration using a code developed for simulations of collinear laser spectroscopy [204, 207].

In this case, the neutralisation of the negative ion beam injected from the Paul trap was assumed to take place on a plane at the center of the MR-ToF after about fifty revolutions with a trapping efficiency of 98 %. The distribution of neutral particles at the position of the neutral particle detector is shown in Figure 6.8. Hence, with a target diameter of about 6.5 mm as used
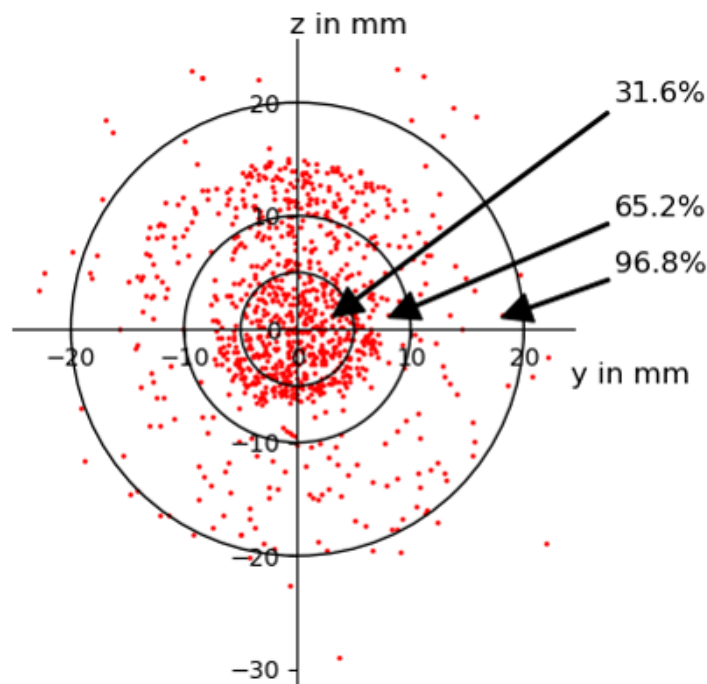
FIGURE 6.8: Neutral particle spread at the position of the detector. Figure courtesy of F. Maier.

in the neutral detector of GANDALPH, only about one third of the neutral atoms would be detected 100 cm from the center of the MR-ToF, assuming

a 100 % detection efficiency. The geometrical detection efficiency versus the detector distance from the center of the MR-ToF is shown in Figure 6.9 for three different detector sizes.
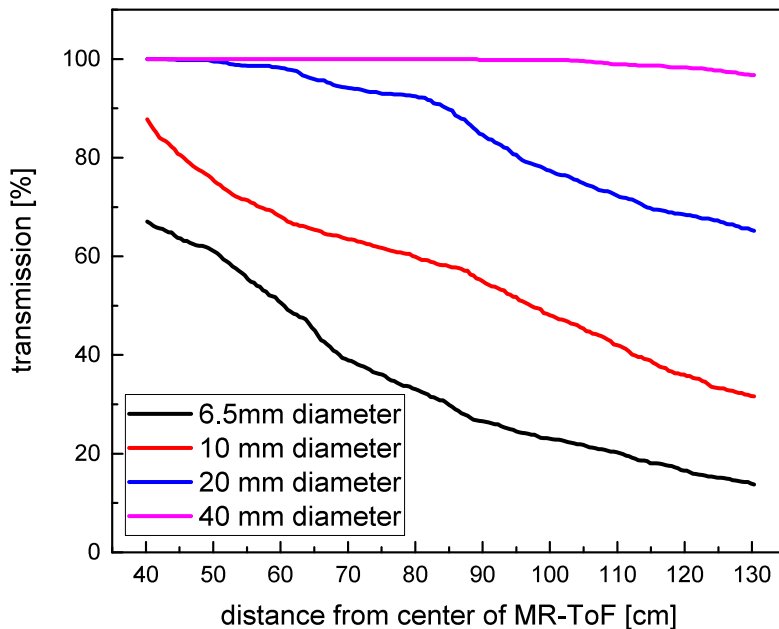
FIGURE 6.9: Neutral particle detection efficiency for different target diameters. Figure courtesy of F. Maier.

Detector targets with a diameter of 40 mm or larger are expected to detect almost 100 % of the neutral atoms created, while for detectors with smaller
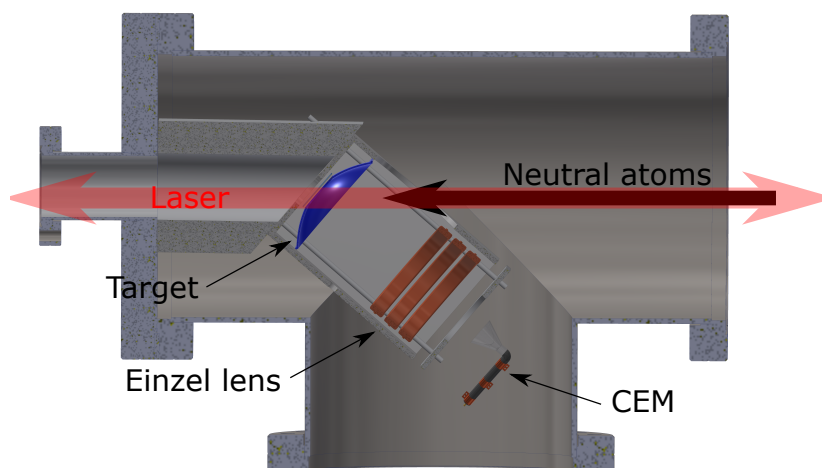
FIGURE 6.10: Neutral particle detector for MIRACLS. Neutral atoms arriving from the right impinge on the conical target (blue) and create secondary electrons, which are guided into a CEM by use of an electrostatic potential and an focussing Einzel lens (orange). Courtesy of J. Warbinek.

target areas, the detection efficiency decreases somewhat linearly with increasing distance. Therefore, a larger surface area for the neutral particle detector was necessary, ideally to be placed as close as possible to the MR-ToF. The design, shown in Figure 6.10 and the testing of the new neutral particle detector was performed by J. Warbinek and M. Nichols, who are both part of the GANDALPH collaboration.

6.2.3 Preparation of ^{36}Cl

In order to obtain ^{36}Cl, a sample of 29.4 mg $MgCl_2$ was filled into two quartz tubes under helium atmosphere. The ampoules, one of which is shown in Figure 6.11, were then sealed by melting the glass and sent to the Institute Laue-Langevin, where it was irradiated for seven days in a high neutron flux reactor with up to 1.5×10^{15} neutrons$/(s \cdot cm^2)$, overseen by U. Köster. The expected composition of the sample one year after irradiation is shown in table 6.5.

FIGURE 6.11: $MgCl_2$ sample prepared for irradiation at the Institute Laue-Langevin. The $MgCl_2$ sample is filled into a quartz tube under helium atmosphere.

In order to reduce the activity caused by ^{35}S and facilitate sample handling, a chemical purification method was proposed in collaboration with P. Thoerle and colleagues from the nuclear chemistry department of the Johannes Gutenberg-Universität Mainz. There, the $MgCl_2$ sample is converted into AgCl utilising a precipitation process where about ninety percent of the sulphur is removed from the sample.

In order to ensure the feasibility of using the AgCl compound in terms of decomposition and ionisation in the ion source, efficiency measurements of both AgCl and $MgCl_2$ were performed at the ISLDE Offline 1 facility using

TABLE 6.5: Expected content of radioactive species of the 29.4 mg $MgCl_2$ sample 365 days after irradiation, after all short-lived isotopes have decayed.

Isotope	Activity [Bq]	number of atoms
^{36}Cl	6.8×10^5	9.2×10^{17}
^{35}S	5×10^8	5.59×10^{15}
^{33}P	9×10^1	2.7×10^8

a tubular LaB_6 ioniser in a negative surface ion source. Both samples were prepared within a tantalum tube "mass marker" and subsequently vaporised by resistive heating. The integrated ion beam current of the separated beam was measured over time and corrected for background determined by a mass scan before the heating of the chlorine mass marker. The transmission efficiency was estimated to be 100 % by comparing the integrated separated beam of a full mass scan (1 u to 300 u) to the total beam of the ion source before the separator magnet.

The resulting efficiencies of AgCl vs. $MgCl_2$ were 0.04 % and 0.17 %, respectively. The low absolute efficiency can be explained by the source being extensively used in previous experiments, resulting in some mechanical disalignment and reduced surface ioniser quality. However, in this case, only the relative efficiency between the two samples is of relevance, which is within a factor of four. With the amount of ^{36}Cl available, this is an acceptable loss to perform the planned experiment.
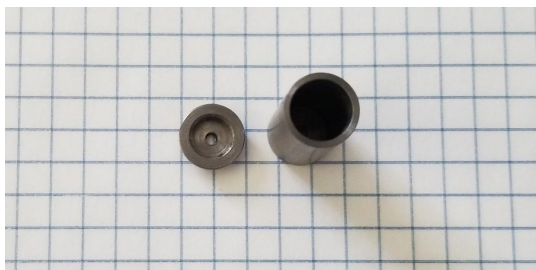
FIGURE 6.12: Tantalum oven to be filled with AgCl and connected to the ion source via a tantalum tube which in turn is connected to the hole in the lid.

Due to the macroscopic sample size, the ^{36}Cl will be prepared in a new

tantalum oven instead of the standard tantalum capillary. This "molecular beam oven" was initially developed within the SY-STI-RBS section for the creation of molecular compounds via e.g. fluorination of a sample placed within the tantalum container, shown in Figure 6.12, which is then connected to the ion source via a tantalum tube. However, the sample mostly contains the stable chlorine isotopes, with the ratio of the stable chlorine isotopes to ^{36}Cl in the sample being about 1:1000. Due to the space charge limitations in the Paul trap allowing only about 1×10^3 ions to be trapped in the Paul trap before space charge effects are noticeable [209], this would result in about only one ^{36}Cl ion present at a given time in the Paul trap. Consequently, it is necessary to mass separate the ion beam before injection into the Paul trap.

This can be achieved by the installation of a quadrupole mass filter (QMF) in the GANDIS beamline. A QMF (*ABB Extrel 150 QC (Merlin)*) was acquired from the AG LARISSA at the Johannes Gutenberg-Universität Mainz, previously used for resonance ionisation mass spectrometry in work by S. Raeder, K. Blaum and others [144, 255].

The QMF will be integrated into the GANDIS beamline with a dedicated vacuum chamber with injection and extraction optics. The control of the QMF was upgraded from a Windows NT based system to a LabView compactRIO device, controlling all DC and RF voltages on the quadrupole itself as well as the mass command via a 0 V to 10 V input. Injection and extraction optics are supplied by separate high voltage supplies. The mounting pieces of the QMF in the vacuum chamber were designed using Inventor and are comprised of a combination of the *Thorlabs* 60 mm cage system and 3D printed parts made out of polylactic acid (PLA).

The final design, shown in Figure 6.13 and SIMION simulation was performed by M. Reponen (University of Jyväskylä) based on initial designs and simulations created by the author of this thesis. In these simulations, negative ^{35}Cl and ^{37}Cl ions were created inside the GANDIS ion source with a uniform beam energy distribution of 0.5 eV-1.5 eV and extracted by a -450 V potential. In order to achieve ion beam energies at which a mass resolution can be achieved, as discussed in chapter 3, the QMF was also biased to the

extraction potential of $-450\,\mathrm{V}$. The potentials of the ion optical elements are given in table 6.6.
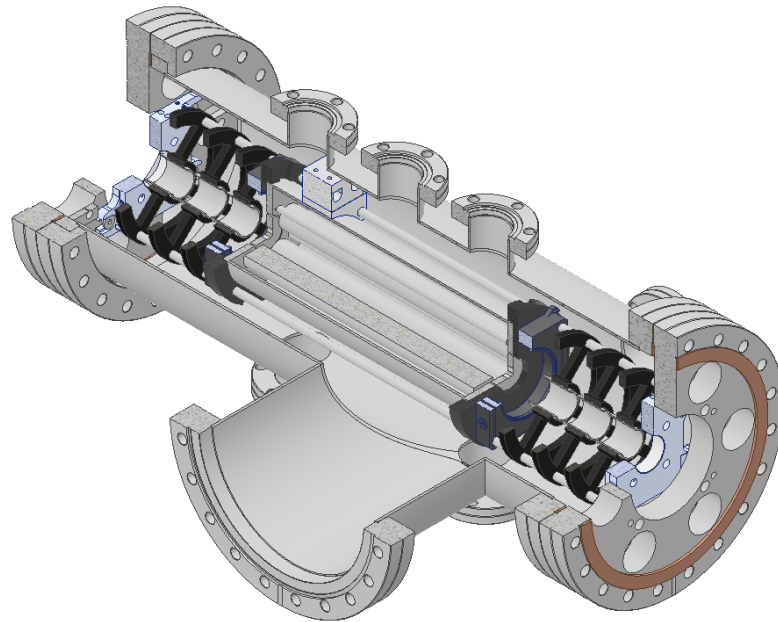
FIGURE 6.13: QMF mount and ion optics. The mounting system comprises a combination of 3D printed parts (black) to mount Einzel lenses and a Thorlabs cage system. The ions are injected and extracted utilising Einzel lenses.

The QMF was scanned across A/q values between -32 and -38 and the transmission recorded at various locations as indicated in Figure 6.14. The injection from the ion source into the QMF housing is achieved with about $85\,\%$ transmission efficiency, resulting from deflection of ions by the $-450\,\mathrm{V}$ potential of the QMF as well as losses seen in previous simulations of the GANDIS beamline. Most ion losses occur during the mass separation process in the QMF as well as during the extraction and re-acceleration process. The overall transmission through the QMF to the end of the beamline for the two chlorine isotopes was about $15\,\%$-$20\,\%$, as shown in Figure 6.14 with a mass peak width of about 0.6, corresponding to a mass resolving power of 60. This would overall yield a transmission efficiency of about $10\,\%$ from GANDIS into the Paul trap.

However, these results are to be verified experimentally. Currently, the QMF hardware is connected to an electron impact ion source in order to investigate the mass resolving power and confirm proper hardware operation

before connecting it to the GANDIS beamline.

TABLE 6.6: Potentials used for the simulation of the ion beam transmission through the QMF.

Electrode	Value
Ion source bias	$-450\,\text{V}$
Extractor	$0\,\text{V}$
Einzel lens 1	$1000\,\text{V}$
Drift tube	$0\,\text{V}$
Einzel lens 2	$20\,\text{V}$
X-steerer left	$0\,\text{V}$
X-steerer right	$0\,\text{V}$
X-steerer up	$-5\,\text{V}$
X-steerer down	$0\,\text{V}$
Einzel lens 3	$-300\,\text{V}$
QMF outer cylinder	$-445\,\text{V}$
QMF entrance aperture	$-446\,\text{V}$
QMF support rods	$-445\,\text{V}$
QMF frequency	$1.3\,\text{MHz}$
QMF effective radius	$8.33 \times 10^{-3}\,\text{m}$
QMF exit aperture	$-444\,\text{V}$
Einzel lens 4	$-290\,\text{V}$

In case the QMF is not operational with acceptable efficiencies and mass resolution, the sample of ^{36}Cl could be further purified for instance at the ISOLDE Offline 1 facility where the isotope could be implanted into a sample foil in the detector chamber after the dipole magnet, before being inserted in the mass marker of the GANDIS at MIRACLS.
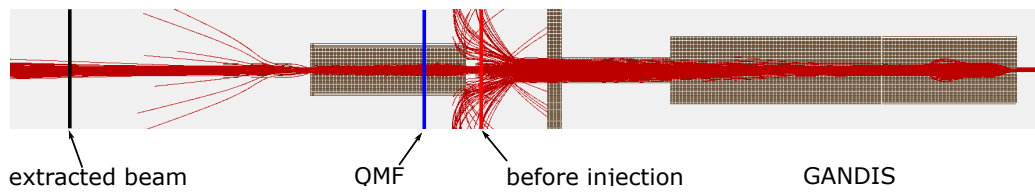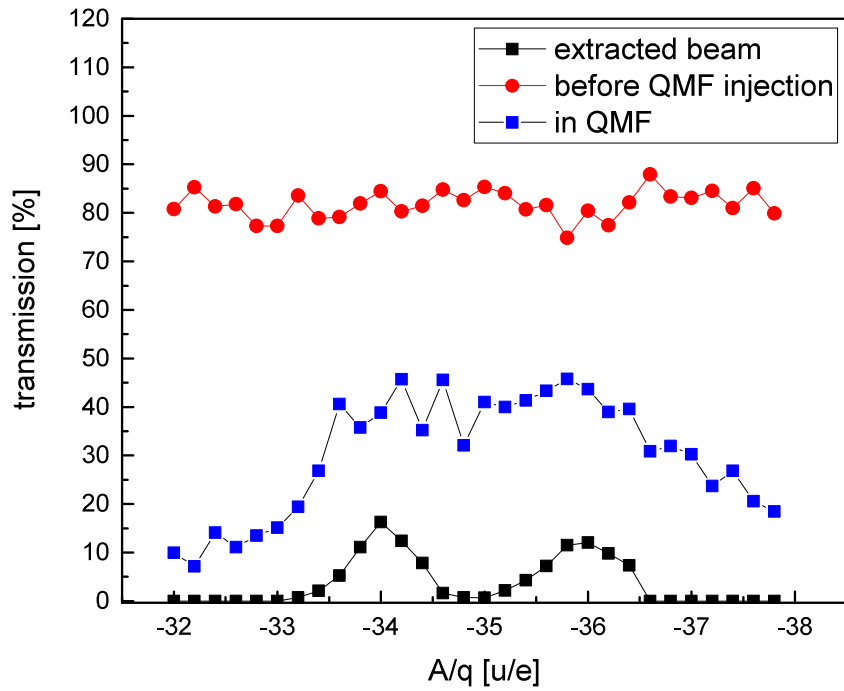
FIGURE 6.14: QMF transmission simulation. Top: Ion beam transmission before (red), in (blue) and after the last Einzel lens (black). Bottom: Trajectories of the ion beam with planes for transmission measurements indicated in red, blue and black, respectively.

Chapter 7

Conclusion and Outlook

Due to the small binding energy (EA) of the additional electron, negative ions are fragile quantum systems, for which in most cases any optical transition leads into the continuum, creating a neutral atom and a free electron. However, negative ions are not only of fundamental interest in probing electron correlation effects but play a role in many other applications and fields of physics [47, 49, 228, 40, 36, 37, 15]. The work presented in this thesis aims towards experimental investigations of specific radioactive elements, e.g. astatine, as well as the advancement of their production at on-line facilities like ISOLDE.

A major result of this thesis is the determination of the electron affinity of astatine utilising collinear photodetachment spectroscopy. This represents an outstanding accomplishment in the sensitive study on rare negative ions and paves the way for future studies of other radioisotopes such as polonium or heavy and in the remote future eventually super-heavy elements. The measurement was performed utilising the GANDALPH detector, which beforehand underwent substantial upgrades in anticipation for this and future measurement campaigns. The upgrades encompass improvements in ion beam steering, detection and data acquisition. As a specific breakthrough, the target material for the neutral particle detector was changed from an ITO to a graphene coated quartz plate, reducing the photoelectron background substantially and extending the transmissible photon energy into the UV range. The determined experimental value for the EA of astatine, $2.41578(7)$ eV, is in excellent agreement with the theoretical prediction of

2.414(16) eV. Overall, this measurement not only marks a milestone in the investigation of radioactive elements that need to be artificially produced to be studied, but also facilitates the development of astatine radiopharmaceuticals in targeted alpha therapy by revealing fundamental chemical properties such as the electronegativity, electrophilicity and hardness.

Experimentally, the refinement of the collinear laser photodetachment technique by utilising an MR-ToF device was prepared for future applications. This step has the potential to greatly facilitate future investigations on negative ions of radioisotopes concerning e.g. isotope shifts in the EA, specifically bringing radioactive elements and eventually super-heavy elements, where the latter are produced only at an atom at a time rate, into reach. As a first demonstration of laser photodetachment in an MR-ToF device, the measurement of the isotope shift of the electron affinity of the stable chlorine isotopes, as well as the long-lived radioactive ^{36}Cl was prepared. Therefore, a dedicated ion source and beamline has been designed and commissioned which can deliver negative ions to the MIRACLS proof-of-principle experiment. The transmission of negative ions through the setup has been demonstrated. However, technical issues with the trapping and cooling in the Paul Trap of the MIRACLS experimental setup prohibited first photodetachment experiments, which are expected to take place once these issues have been resolved.

With the investigation tools of radioisotopes being readily established at ISOL facilities, the measurement of the isotope shift of the EA of chlorine is expected to take place in the upcoming online period at ISOLDE (LHC Run 3), for which eight shifts were granted by the INTC (see proposal D, status report E and minutes of the INTC [256]). Furthermore, the determination of the EA of polonium was proposed and six shifts were granted (see letter of intent F and minutes of the INTC [117]), marking not only a further step in the investigation of negative ions, but additionally probing the conversion efficiency of positive to negative ions in a charge exchange cell as supplementary production pathway for negative ions with lower EA.

In order to increase ionisation efficiency and broaden the availability of

negative ion beams at ISOLDE, production methods other than the currently used LaB_6 surface ioniser were investigated. As an alternative surface ioniser material, $SrVO_3$ was produced and characterised utilising X-ray diffraction. The work function of $SrVO_3$, determined by thermal electron emission, was measured to be around 3.28 eV. Measurements at 1630 °C yielded an efficiency of 10.6 % for iodine. However, the ioniser surface was damaged at these temperatures, resulting in a non-recoverable decrease in ionisation efficiency as well as an increase in work function to 3.69 eV. In future studies, the thermal stabilisation and decrease of the work function of $SrVO_3$ will be investigated utilising doping with e.g. molybdenum or barium. In addition, a different production approach generating a determined crystal orientation of the material might result in a reduced work function of the surface ionisers in general. However, at the current stage, LaB_6 remains the superior choice as surface ioniser in terms of stability, efficiency and availability.

As an alternative approach to solid surface ionisers, negative ion production utilising the injection of caesium either for surface or sputter-type negative ion production was investigated. Using a FEBIAD type ion source with caesium injection via a Cs_2CrO_4 dispenser material, negative fluorine ions were produced with an efficiency of 2.8×10^{-4} % using NF_3 as precursor. However, negative ions were primarily produced in the caesiated transfer line instead of via sputter generation through accelerated positive caesium ions, while the acceleration voltage primarily served as an extraction and guiding potential for the surface ionised negative ions. Therefore, the geometry was analysed to be not optimal neither for sputter type production nor for surface ionisation.

As a consequence, surface ionisation utilising a caesiated tantalum surface was investigated. Using this approach, it was possible to produce negative ions, however, efficiencies below 0.1 % were measured for bromine. In addition, the source behaviour was very unstable, likely caused by the fragile balance between caesium injection, surface adsorption and chemical reactions in the source. Hence, this approach does not seem to be an improvement upon the current LaB_6 surface ioniser.

For sputter-type generation of negative ions, the KENIS ion source was refurbished and characterised utilising two methods of caesium delivery. The use of a caesium dispenser compound resulted in an efficiency of about 0.6 % for fluorine, however the stability of the ion beam was poor. Additionally, negative oxygen ion beams as intense as 700 nA, released from the Cs_2CrO_4 dispenser, prohibited the investigation of ionisation efficiencies for other species of interest such as sulphur and oxygen on the same mass channels. Consequently, an external caesium reservoir and injection line was developed. As a result, the oxygen contamination was reduced significantly and the ion source stability was improved. However, the amount of caesium delivered into the source was found to be insufficient, likely due to the temperature limitation of mechanical parts in the caesium injection line or a cold spot on the water cooled target base, respectively. Furthermore, it was discovered that the calibrated gas leaks used for the injection of fluoride gases clogged over time likely due to sintering caused by exposure to heat, further complicating accurate efficiency measurements. With these technical issues resolved, the KENIS ion source is expected to be capable of delivering negative fluorine beams efficiently at ISOLDE. In addition, the production of negative oxygen and sulphur ion beams seems promising.

In conclusion, for the production of radioactive negative ions, the KENIS ion source is a promising tool to broaden the negative ion beam availability of ISOLDE by delivering beams of fluorine as well as elements such as oxygen and sulphur. Supplementary investigations of $SrVO_3$ and alternative surface ioniser materials may facilitate this further.

Appendix A

Publication 1 - Upgrades of the GANDALPH photodetachment detector

Contribution: I planned, designed, implemented and comissioned the upgrades to the GANDALPH detector and have written the first draft and am main author of the paper. The picoamperemeter and control for the voltage supplies were provided in collaboration with Lars Bengtsson of the University of Gothenburg.

Article removed due to copyright. It can be found under https://doi.org/10.1016/j.nimb.2019.05.015.

Appendix B

Publication 2- A graphene-based neutral particle detector

Contribution: I took part in the initial discussion and planning of the project as well as the experiment and data acquisition. In addition, I wrote the first draft of the manuscript together with the first author, Jessica Warbinek.

Article removed due to copyright. It can be found under https://doi.org/10.1063/1.5080517.

Appendix C

Publication 3- The electron affinity of astatine

Contribution: I tested and prepared the GANDALPH detector for the experiment, was part of the group leading the setup and operation of the experiment and participated in data taking. Additionally, I performed the independant data analysis in parallel with Julia Karls, wrote the initial draft and prepared the manuscript with the core writing group.

Appendix D

Proposal to the INTC-Measurement of shifts in the electron affinities of chlorine isotopes

Contribution: As a part of the GANDALPH collaboration, I was part of the planning of this experiment and preparation of the proposal. The proposal was endorsed by the INTC and was awarded eight shifts [257, 256].

Article removed due to copyright.

Appendix E

Status report- Measurement of shifts in the electron affinities of chlorine isotopes

Contribution: As a part of the GANDALPH collaboration, I was part of the planning of this experiment and preparation and writing of this status report.

Article removed due to copyright.

Appendix F

Letter of Intent - electron affinity of polonium

Contribution: I was part of the planning of this experiment and the initial proposal. In addition, I took part in the writing of this letter of intent. The letter of intent was endorsed by the INTC and awarded with six shifts [117].

Article removed due to copyright.

Bibliography

[1] J. J. Thomson. "XL. Cathode Rays". In: *The London, Edinburgh, and Dublin Philosophical Magazine and Journal of Science* 44.269 (1897), p. 293. DOI: 10.1080/14786449708621070.

[2] NobelPrize.org. *The Nobel Prize in Physics 1906*. URL: https://www.nobelprize.org/prizes/physics/1906/summary/.

[3] E. Goldstein. "Ueber eine noch nicht untersuchte Strahlungsform an der Kathode inducirter Entladungen". In: *Annalen der Physik* 300.1 (1898), pp. 38–48. DOI: https://doi.org/10.1002/andp.18983000105.

[4] W. Wien. "Untersuchungen über die electrische Entladung in verdünnten Gasen". In: *Annalen der Physik* 301.6 (1898), pp. 440–452. DOI: https://doi.org/10.1002/andp.18983010618.

[5] Sir J.J. Thomson. "XLII. Ionization by moving electrified particles". In: *The London, Edinburgh, and Dublin Philosophical Magazine and Journal of Science* 23.136 (1912), pp. 449–457. DOI: 10.1080/14786440408637241.

[6] J. J. Thomson. "Bakerian Lecture: Rays of positive electricity". In: *Proceedings of the Royal Society of London. Series A, Containing Papers of a Mathematical and Physical Character* 89.607 (1913), pp. 1–20. DOI: 10.1098/rspa.1913.0057.

[7] Max Planck. "Ueber das Gesetz der Energieverteilung im Normalspectrum". In: *Annalen der Physik* 309.3 (1901), pp. 553–563. DOI: https://doi.org/10.1002/andp.19013090310.

[8] A. Einstein. "Über einen die Erzeugung und Verwandlung des Lichtes betreffenden heuristischen Gesichtspunkt". In: *Annalen der Physik* 322 (1905), pp. 132–148. DOI: 10.1002/andp.19053220607.

[9]   N. Bohr. "I. On the constitution of atoms and molecules". In: *The London, Edinburgh, and Dublin Philosophical Magazine and Journal of Science* 26.151 (1913), pp. 1–25. DOI: 10.1080/14786441308634955.

[10]   Werner Heisenberg. "Ueber den anschaulichen Inhalt der quantentheoretischen Kinematik und Mechanik". In: *Zeitschrift für Physik* 43.3 (1927), pp. 172–198. ISSN: 0044-3328. DOI: 10.1007/BF01397280.

[11]   E. Schrödinger. "An Undulatory Theory of the Mechanics of Atoms and Molecules". In: *Physical Review* 28.6 (Dec. 1926), pp. 1049–1070. DOI: 10.1103/PhysRev.28.1049.

[12]   P. A. M. Dirac. "The quantum theory of the electron". In: *Proceedings of the Royal Society of London. Series A, Containing Papers of a Mathematical and Physical Character* 117.778 (1928), pp. 610–624. DOI: https://doi.org/10.1098/rspa.1928.0023.

[13]   W. Demtröder. *Atoms, molecules and photons*. Vol. 3. 7. Springer, 2010. ISBN: 978-3-642-10298-1.

[14]   T. Andersen. "Atomic negative ions: structure, dynamics and collisions". In: *Physics Reports* 394.4 (2004), pp. 157–313. ISSN: 0370-1573. DOI: https://doi.org/10.1016/j.physrep.2004.01.001.

[15]   C. W. Walter et al. "Candidate for Laser Cooling of a Negative Ion: Observations of Bound-Bound Transitions in La⁻". In: *Phys. Rev. Lett.* 113 (6 2014), p. 063001. DOI: 10.1103/PhysRevLett.113.063001.

[16]   C. W. Walter et al. "Infrared photodetachment of Ce⁻: Threshold spectroscopy and resonance structure". In: *Phys. Rev. A* 76 (2007), p. 052702. DOI: 10.1103/PhysRevA.76.052702.

[17]   René C. Bilodeau and Harold K. Haugen. "Experimental Studies of Os⁻: Observation of a Bound-Bound Electric Dipole Transition in an Atomic Negative Ion". In: *Phys. Rev. Lett.* 85 (3 2000), pp. 534–537. DOI: 10.1103/PhysRevLett.85.534.

[18] Rulin Tang et al. "Candidate for Laser Cooling of a Negative Ion: High-Resolution Photoelectron Imaging of Th⁻". In: *Phys. Rev. Lett.* 123 (20 2019), p. 203002. DOI: 10.1103/PhysRevLett.123.203002.

[19] David J Pegg. "Structure and dynamics of negative ions". In: *Reports on Progress in Physics* 67.6 (2004), pp. 857–905. DOI: 10.1088/0034-4885/67/6/r02.

[20] Lewis M. Branscomb and Stephen J. Smith. "Experimental Cross Section for Photodetachment of Electrons from H⁻ and D⁻". In: *Phys. Rev.* 98 (4 1955), pp. 1028–1034. DOI: 10.1103/PhysRev.98.1028.

[21] Lewis M Branscomb and WL Fite. "Photodetachment of the hydrogen negative ion". In: 93.3 (1954), pp. 651–651.

[22] H. S. W. Massey. *Negative ions*. Cambridge University Press, 1938.

[23] H. Hotop and W. C. Lineberger. "Binding Energies in Atomic Negative Ions: II". In: *J. Phys. Chem. Ref. Data* 14.3 (1985), pp. 731–750. DOI: http://dx.doi.org/10.1063/1.555735.

[24] H. Hotop and W. C. Lineberger. "Binding energies in atomic negative ions". In: *Journal of Physical and Chemical Reference Data* 4.3 (1975), pp. 539–576. DOI: 10.1063/1.555524.

[25] T. Andersen et al. "Binding Energies in Atomic Negative Ions: III". In: *Journal of Physical and Chemical Reference Data* 28.6 (1999), pp. 1511–1533. DOI: 10.1063/1.556047.

[26] Xiaoxi Fu et al. "Electron affinity measurements of lanthanide atoms: Pr, Nd, and Tb". In: *Phys. Rev. A* 101 (2 2020), p. 022502. DOI: 10.1103/PhysRevA.101.022502.

[27] Christophe Blondel, Christian Delsart, and François Dulieu. "The Photodetachment Microscope". In: *Phys. Rev. Lett.* 77 (18 1996), pp. 3755–3758. DOI: 10.1103/PhysRevLett.77.3755.

[28] C. Blondel et al. "High-resolution determination of the electron affin-
      ity of fluorine and bromine using crossed ion and laser beams". In:
      Phys. Rev. A 40 (7 1989), pp. 3698–3701. DOI: 10.1103/PhysRevA.40.
      3698.

[29] A. O. Lindahl et al. "Threshold Photodetachment in a Repulsive Po-
      tential". In: *Phys. Rev. Lett.* 108 (3 2012), p. 033004. DOI: 10.1103/
      PhysRevLett.108.033004.

[30] O. Windelius et al. "A collinear angle-resolved photoelectron spec-
      trometer". In: *Nuclear Instruments and Methods in Physics Research Sec-
      tion B: Beam Interactions with Materials and Atoms* 410 (2017), pp. 144–
      152. ISSN: 0168-583X. DOI: https://doi.org/10.1016/j.nimb.2017.
      08.028.

[31] Mikael Eklund et al. "Tomography of photoelectron distributions pro-
      duced through strong-field photodetachment of Ag$^-$". In: *Phys. Rev.
      A* 102 (2 2020), p. 023114. DOI: 10.1103/PhysRevA.102.023114.

[32] K.G. Rensfelt et al. "Desiree–A Double Electrostatic Storage Ring". In:
      Proc. European Part. Acc. Conf., Lucerne, Switzerland. 2004. URL: https:
      //www.msi.se/desiree/epac04_tuplt124.pdf.

[33] H.T. Schmidt et al. "The lifetime of the helium anion". In: *Journal of
      Physics: Conference Series*. Vol. 388. 1. IOP Publishing. 2012, p. 012006.
      DOI: 10.1088/1742-6596/388/1/012006.

[34] M. K. Kristiansson et al. "Photodetachment Studies of Ir$^-$ Ions at DE-
      SIREE". In: *Journal of Physics: Conference Series* 1412 (2020), p. 132022.
      DOI: 10.1088/1742-6596/1412/13/132022.

[35] G. Cerchiari et al. "Ultracold Anions for High-Precision Antihydrogen
      Experiments". In: *Phys. Rev. Lett.* 120 (13 2018), p. 133205. DOI: 10.
      1103/PhysRevLett.120.133205.

[36] T Aumann et al. *PUMA: antiprotons and radioactive nuclei*. Tech. rep.
      CERN-SPSC-2019-033. SPSC-P-361. Geneva: CERN, 2019. URL: https:
      //cds.cern.ch/record/2691045.

[37] Frank Wienholtz. private communication. Nov. 17, 2020.

[38] D Field. "H_2 formation in space: a negative ion route?" In: *Astronomy and Astrophysics* 362 (2000), pp. 774–779. URL: https://ui.adsabs.harvard.edu/abs/2000A&A...362..774F.

[39] Teresa Ross et al. "The Search for H^- in Astrophysical Environments". In: *The Astrophysical Journal* 684.1 (2008), pp. 358–363. DOI: 10.1086/590242.

[40] Thomas J Millar, Catherine Walsh, and Thomas A Field. "Negative ions in space". In: *Chemical reviews* 117.3 (2017), pp. 1765–1795. DOI: 10.1021/acs.chemrev.6b00480.

[41] M. C. McCarthy et al. "Laboratory and Astronomical Identification of the Negative Molecular Ion C_6H^-". In: *The Astrophysical Journal* 652.2 (2006), pp. L141–L144. DOI: 10.1086/510238.

[42] RS Dabas. "Ionosphere and its influence on radio communications". In: *Resonance* 5.7 (2000), pp. 28–43. DOI: 10.1007/BF02867245.

[43] Douglass Edmund Post, K Borrass, and JD Callen. "ITER physics". In: *INIS* 22 (18 1991). URL: https://inis.iaea.org/collection/NCLCollectionStore/_Public/22/064/22064647.pdf?r=1.

[44] Yasuhiko Takeiri. "Negative ion source development for fusion application (invited)". In: *Review of Scientific Instruments* 81.2 (2010), 02B114. DOI: 10.1063/1.3274806.

[45] A. Simonin et al. "R&D around a photoneutralizer-based NBI system (Siphore) in view of a DEMO Tokamak steady state fusion reactor". In: *Nuclear Fusion* 55.12 (2015), p. 123020. DOI: 10.1088/0029-5515/55/12/123020.

[46] Lloyd A Currie. "The remarkable metrological history of radiocarbon dating [II]". In: *Journal of Research of the National Institute of Standards and Technology* 109.2 (2004), p. 185. DOI: 10.6028/jres.109.013.

[47] T.W. Linick et al. "Accelerator mass spectrometry: The new revolution in radiocarbon dating". In: *Quaternary International* 1 (1989), pp. 1–6. ISSN: 1040-6182. DOI: https://doi.org/10.1016/1040-6182(89)90004-9.

[48] Thomas A. Brown et al. "Radiocarbon dating of pollen by accelerator mass spectrometry". In: *Quaternary Research* 32.2 (1989), pp. 205–212. ISSN: 0033-5894. DOI: https://doi.org/10.1016/0033-5894(89)90076-8.

[49] R. Gillespie, R.E.M. Hedges, and J.O. Wand. "Radiocarbon dating of bone by accelerator mass spectrometry". In: *Journal of Archaeological Science* 11.2 (1984), pp. 165–170. ISSN: 0305-4403. DOI: https://doi.org/10.1016/0305-4403(84)90051-7.

[50] Sebastian Rothe et al. "Laser photodetachment of radioactive ^{128}I". In: *Journal of Physics G: Nuclear and Particle Physics* 44.10 (2017), p. 104003. DOI: 10.1088/1361-6471/aa80aa.

[51] David Leimbach et al. "The electron affinity of astatine". In: *Nature communications* 11.1 (2020), pp. 1–9. DOI: 10.1038/s41467-020-17599-2.

[52] Thomas Elias Cocolios et al. "The collinear resonance ionization spectroscopy (CRIS) experimental setup at CERN-ISOLDE". In: *Nuclear Instruments and Methods in Physics Research Section B: Beam Interactions with Materials and Atoms* 317 (2013), pp. 565–569. DOI: https://doi.org/10.1016/j.nimb.2013.05.088.

[53] B. Schinzler et al. "Collinear laser spectroscopy of neutron-rich Cs isotopes at an on-line mass separator". In: *Physics Letters B* 79.3 (1978), pp. 209–212. ISSN: 0370-2693. DOI: 10.1016/0370-2693(78)90224-1.

[54] Rainer Neugart et al. "High-Resolution Spectroscopy in Fast Atomic Beams". In: *Laser Spectroscopy III*. Berlin, Heidelberg: Springer Berlin Heidelberg, 1977, pp. 446–447. ISBN: 978-3-540-35968-5.

[55] D. Beck et al. "Direct mass measurements of unstable rare earth isotopes with the ISOLTRAP mass spectrometer". In: *Nuclear Physics A* 626.1-2 (1997), pp. 343–352. DOI: doi.org/10.1016/S0375-9474(97)00556-3.

[56] R. Catherall et al. "The ISOLDE facility". In: *Journal of Physics G: Nuclear and Particle Physics* 44.9 (2017), p. 094002. DOI: 10.1088/1361-6471/aa7eba.

[57] Y. Liu, D. W. Stracener, and T. Stora. "Production of negatively charged radioactive ion beams". In: *New Journal of Physics* 19.8 (2017), p. 085005. DOI: 10.1088/1367-2630/aa609c.

[58] Roy Middleton. *A Negative-Ion Cookbook*. Tech. rep. University of Pennsylvania, 1990. URL: http://www.pelletron.com/cookbook.pdf.

[59] Bernhard Wolf. *Handbook of Ion sources*. CRC Press, 1995. ISBN: 978-0367579708.

[60] Jan Heinemeier and Preben Hvelplund. "Production of 15-90 keV negative heavy ions by charge exchange with Mg vapour". In: *Nuclear Instruments and Methods* 148.1 (1978), pp. 65–75. ISSN: 0029554X. DOI: 10.1016/0029-554X(78)90337-3.

[61] B. Vosicki et al. "Intense beams of radioactive halogens produced by means of surface ionization". In: *Nuclear Instruments and Methods in Physics Research* 186.1 (1981), pp. 307 –313. ISSN: 0167-5087. DOI: https://doi.org/10.1016/0029-554X(81)90918-6.

[62] T. Stora et al. *First negative halogen beams produced at PSBooster-ISOLDE*. Tech. rep. Abstract only. URL: https://cds.cern.ch/record/1356484.

[63] H. E. Gallagher. "Poisoning of LaB$_6$ Cathodes". In: *Journal of Applied Physics* 40.1 (1969), pp. 44–51. DOI: 10.1063/1.1657092.

[64] C.J. Foot. *Atomic Physics*. Oxford Master Series in Physics. OUP Oxford, 2005. ISBN: 9780198506966.

[65] M. Weissbluth. *Atoms and molecules*. Elsevier, 2012. ISBN: 978 012 7444 505.

[66] Louis de Broglie. "XXXV. A tentative theory of light quanta". In: *The London, Edinburgh, and Dublin Philosophical Magazine and Journal of Science* 47.278 (1924), pp. 446–458. DOI: 10.1080/14786442408634378.

[67] A. D. McNaught and A. Wilkinson. *IUPAC. Compendium of Chemical Terminology (the "Gold Book")*. Blackwell Scientific Publications, 1997. DOI: 10.1351/goldbook.E01977.

[68] K. R. Lykke, K. K. Murray, and W. C. Lineberger. "Threshold photodetachment of H$^-$". In: *Phys. Rev. A* 43 (11 1991), pp. 6104–6107. DOI: 10.1103/PhysRevA.43.6104.

[69] A. Kramida et al. NIST Atomic Spectra Database (ver. 5.7.1), [Online]. Available: https://physics.nist.gov/asd [2020, March 25]. National Institute of Standards and Technology, Gaithersburg, MD. 2019.

[70] U. Berzinsh et al. "Isotope shift in the electron affinity of chlorine". In: *Physical Review A - Atomic, Molecular, and Optical Physics* 51 (1 1995), pp. 231–238. DOI: 10.1103/PhysRevA.51.231.

[71] Christophe Blondel. "Comment on "Measurement of the electron affinity of the lanthanum atom"". In: *Phys. Rev. A* 101 (1 2020), p. 016501. DOI: 10.1103/PhysRevA.101.016501.

[72] Donald R. Beck, Steven M. O'Malley, and Lin Pan. "Relativistic Configuration Interaction Calculations for Lanthanide and Actinide Anions". In: *Computational Methods in Lanthanide and Actinide Chemistry*. John Wiley Sons, Ltd, 2015. Chap. 1, pp. 1–21. ISBN: 9781118688304. DOI: https://doi.org/10.1002/9781118688304.ch1.

[73] Jeremy Felton, Manisha Ray, and Caroline Chick Jarrold. "Measurement of the electron affinity of atomic Ce". In: *Phys. Rev. A* 89 (3 2014), p. 033407. DOI: 10.1103/PhysRevA.89.033407.

[74] Z. Felfli, A. Z. Msezane, and D. Sokolovski. "Resonances in low-energy electron elastic cross sections for lanthanide atoms". In: *Phys. Rev. A* 79 (1 2009), p. 012714. DOI: 10.1103/PhysRevA.79.012714.

[75] Shi-Bo Cheng and AW Castleman. "Direct experimental observation of weakly-bound character of the attached electron in europium anion". In: *Scientific reports* 5.1 (2015), pp. 1–8. DOI: 10.1038/srep12414.

[76] Steven G. Bratsch and J.J. Lagowski. "Electron affinities of the actinides". In: *Chemical Physics Letters* 107.2 (1984), pp. 136–140. ISSN: 0009-2614. DOI: https://doi.org/10.1016/0009-2614(84)85687-0.

[77] V. T. Davis and J. S. Thompson. "Measurement of the electron affinity of thulium". In: *Phys. Rev. A* 65 (1 2001), p. 010501. DOI: 10.1103/PhysRevA.65.010501.

[78] Steven G. Bratsch. "Electron affinities of the lanthanides". In: *Chemical Physics Letters* 98.2 (1983), pp. 113–117. ISSN: 0009-2614. DOI: https://doi.org/10.1016/0009-2614(83)87108-5.

[79] Xiao-xi Fu et al. "Measurement of electron affinity of atomic lutetium via the cryo-SEVI Method". In: *Chinese Journal of Chemical Physics* 32.2 (2019), pp. 187–192. DOI: 10.1063/1674-0068/cjcp1812293.

[80] René C Bilodeau, Michael Scheer, and Harold K Haugen. "Infrared laser photodetachment of transition metal negative ions: studies on Cr$^-$, Mo$^-$, Cu$^-$ and Ag$^-$". In: *Journal of Physics B: Atomic, Molecular and Optical Physics* 31.17 (1998), pp. 3885–3891. DOI: 10.1088/0953-4075/31/17/013.

[81] Johan Rohlén. "Excited States in Negative Ions". PhD thesis. University of Gothenburg, 2014.

[82] H.S.W. Massey. "Negative Ions". In: *Advances in Atomic and Molecular Physics*. Ed. by David R. Bates and Benjamin Bederson. Vol. 15. Academic Press, 1979, pp. 1–36. DOI: https://doi.org/10.1016/S0065-2199(08)60293-6.

[83] David R. Bates. "Negative Ions: Structure and Spectra". In: *Advances In Atomic, Molecular, and Optical Physics*. Ed. by Sir David Bates and Benjamin Bederson. Vol. 27. Academic Press, 1990, pp. 1–80. DOI: 10.1016/S1049-250X(08)60148-2.

[84]   J. Franck and E. G. Dymond. "Elementary processes of photochemical reactions". In: *Trans. Faraday Soc.* 21 (February 1926), pp. 536–542. DOI: 10.1039/TF9262100536.

[85]   Melvin Lax. "The Franck-Condon Principle and Its Application to Crystals". In: *The Journal of Chemical Physics* 20.11 (1952), pp. 1752–1760. DOI: 10.1063/1.1700283.

[86]   Henning T. Schmidt et al. "DESIREE as a new tool for interstellar ion chemistry". In: *International Journal of Astrobiology* 7.3-4 (2008), pp. 205–208. DOI: 10.1017/S1473550408004229.

[87]   Eugene P. Wigner. "On the behavior of cross sections near thresholds". In: *Physical Review* 73.9 (1948), pp. 1002–1009. ISSN: 0031899X. DOI: 10.1103/PhysRev.73.1002.

[88]   T. F. O'Malley. "Effect of Long-Range Final-State Forces on the Negative- Ion Photodetachment Cross Section near Threshold". In: *Phys. Rev.* 137 (6A 1965), A1668–A1672. DOI: 10.1103/PhysRev.137.A1668.

[89]   John W. Farley. "Photodetachment cross sections of negative ions: The range of validity of the Wigner threshold law". In: *Phys. Rev. A* 40 (11 1989), pp. 6286–6292. DOI: 10.1103/PhysRevA.40.6286.

[90]   Gregory H. Wannier. "The Threshold Law for Single Ionization of Atoms or Ions by Electrons". In: *Phys. Rev.* 90 (5 1953), pp. 817–825. DOI: 10.1103/PhysRev.90.817.

[91]   Pontus Andersson. "Laser Photodetachment of Negative Ions Fundamental Research and Applications". PhD thesis. 2009.

[92]   Dag Hanstorp. "An ion beam apparatus for collinear photodetachment experiments". In: *Nuclear Instruments and Methods in Physics Research Section B: Beam Interactions with Materials and Atoms* 100.1 (1995), pp. 165–175. ISSN: 0168-583X. DOI: https://doi.org/10.1016/0168-583X(94)00656-3.

[93] S. L. Kaufman. "High-resolution laser spectroscopy in fast beams". In: *Optics Communications* 17.3 (1976), pp. 309–312. ISSN: 00304018. DOI: 10.1016/0030-4018(76)90267-4.

[94] J. Cooper and Richard N. Zare. "Angular distribution of photoelectrons". In: *The Journal of Chemical Physics* 48.2 (1968), pp. 942–943. DOI: 10.1063/1.1668742.

[95] Christophe Valli, Christophe Blondel, and Christian Delsart. "Measuring electron affinities with the photodetachment microscope". In: *Phys. Rev. A* 59 (5 1999), pp. 3809–3815. DOI: 10.1103/PhysRevA.59.3809.

[96] Yves Nievergelt. "Elementary Inversion of Radon's Transform". In: *SIAM Review* 28.1 (1986), pp. 79–84. DOI: 10.1137/1028005.

[97] G.D. Alton. "Negative-Ion Formation Processes and Sources". In: *Electrostatic Accelerators: Fundamentals and Applications*. Ed. by Ragnar Hellborg. Berlin, Heidelberg: Springer Berlin Heidelberg, 2005, pp. 222–273. ISBN: 978-3-540-27095-9. DOI: 10.1007/3-540-27095-7_20.

[98] Irving Langmuir, K. H. Kingdon, and Ernest Rutherford. "Thermionic effects caused by vapours of alkali metals". In: *Proceedings of the Royal Society of London. Series A, Containing Papers of a Mathematical and Physical Character* 107.741 (1925), pp. 61–79. DOI: 10.1098/rspa.1925.0005.

[99] M. J. Dresser. "The Saha-Langmuir Equation and its Application". In: *Journal of Applied Physics* 39.1 (1968), pp. 338–339. DOI: 10.1063/1.1655755.

[100] G.V. Samsonov V.S. Fomenko. *Handbook of thermionic properties*. Plenum Press Data Division, 1966. ISBN: 978-1-4684-7293-6.

[101] J. Pelletier and C. Pomot. "Work function of sintered lanthanum hexaboride". In: *Applied Physics Letters* 34.4 (1979), pp. 249–251. DOI: 10.1063/1.90769.

[102] M. Menna et al. "R & D for the development of negative ion beams of halogens". In: *Nuclear Instruments and Methods in Physics Research Section B: Beam Interactions with Materials and Atoms* 266.19 (2008). Proceedings of the XVth International Conference on Electromagnetic Isotope Separators and Techniques Related to their Applications, pp. 4391–4393. ISSN: 0168-583X. DOI: https://doi.org/10.1016/j.nimb.2008.05.064.

[103] D. Leimbach. "Negative Ion Source Development and Photodetachment Studies at ISOLDE". Presented 20 Dec 2017. 2017. URL: https://cds.cern.ch/record/2309565.

[104] Victor E. Krohn. "Emission of Negative Ions from Metal Surfaces Bombarded by Positive Cesium Ions". In: *Journal of Applied Physics* 33.12 (1962), pp. 3523–3525. DOI: 10.1063/1.1702439.

[105] Ming L. Yu. "Work-Function Dependence of Negative-Ion Production during Sputtering". In: *Phys. Rev. Lett.* 40 (9 1978), pp. 574–577. DOI: 10.1103/PhysRevLett.40.574.

[106] G. D. Alton. "An axial geometry cesium sputter negative ion source with continuous tungsten surface ionizer". In: *Nuclear Instruments and Methods in Physics Research Section A: Accelerators, Spectrometers, Detectors and Associated Equipment* 244.1-2 (1986), pp. 133–141. DOI: 10.1016/0168-9002(86)90754-0.

[107] R. Middleton and Charles T. Adams. "A close to universal negative ion source". In: *Nuclear Instruments and Methods* 118.2 (1974), pp. 329–336. ISSN: 0029-554X. DOI: https://doi.org/10.1016/0029-554X(74)90634-X.

[108] R. Middleton. "A versatile high intensity negative ion source". In: *Nuclear Instruments and Methods in Physics Research* 214.2 (1983), pp. 139–150. ISSN: 0167-5087. DOI: https://doi.org/10.1016/0167-5087(83)90580-X.

[109] G.T. Caskey et al. "A simple negative-ion sputter source". In: *Nuclear Instruments and Methods* 157.1 (1978), pp. 1–7. ISSN: 0029-554X. DOI: https://doi.org/10.1016/0029-554X(78)90581-5.

[110] G.D. Alton. "The sputter generation of negative ion beams". In: *Nuclear Instruments and Methods in Physics Research Section B: Beam Interactions with Materials and Atoms* 37-38 (1989), pp. 45–55. ISSN: 0168-583X. DOI: https://doi.org/10.1016/0168-583X(89)90134-1.

[111] G. D. Alton. "High-intensity, heavy negative ion sources based on the sputter principle (invited)". In: *Review of Scientific Instruments* 65.4 (1994), pp. 1141–1147. DOI: 10.1063/1.1145040.

[112] Yoshiharu Mori. "Negative metal ion sources (invited)". In: *Review of Scientific Instruments* 63.4 (1992), pp. 2357–2362. DOI: 10.1063/1.1142928.

[113] J. B. Hasted and Harrie Stewart Wilson Massey. "Inelastic collisions between ions and atoms". In: *Proceedings of the Royal Society of London. Series A. Mathematical and Physical Sciences* 212.1109 (1952), pp. 235–248. DOI: 10.1098/rspa.1952.0078.

[114] H.S.W. Massey. "Collisions between atoms and molecules at ordinary temperatures". In: *Reports on Progress in Physics* 12.1 (1949), pp. 248 – 269. DOI: 10.1088/0034-4885/12/1/311.

[115] Jan Heinemeier and Preben Hvelplund. "Production of 10-80 keV negative heavy ions by charge exchange in Na vapour". In: *Nuclear Instruments and Methods* 148.3 (1978), pp. 425–429. ISSN: 0029554X. DOI: 10.1016/0029-554X(78)91024-8.

[116] Sebastian Rothe. *Preparation of negative ion beams for the determination of the electron affinity of polonium and astatine by laser photodetachment*. Tech. rep. CERN-INTC-2013-037. INTC-I-148. Geneva: CERN, 2013. DOI: 10.17181/CERN.YJ9E.K5F5.

[117] *Minutes of the 66th meeting of the INTC held on Wednesday 3 and Thursday 4 February 2021*. Tech. rep. CERN-INTC-2021-022. INTC-066. Geneva: CERN, 2021. URL: https://cds.cern.ch/record/2751091.

[118] Pierre Radvanyi and Jacques Villain. "The discovery of radioactivity". In: *Comptes Rendus Physique* 18.9 (2017). Science in the making: The Comptes rendus de l'Académie des sciences throughout history, pp. 544 –550. ISSN: 1631-0705. DOI: https://doi.org/10.1016/j.crhy.2017.10.008.

[119] Frederick Soddy. "The Origins of the Conception of Isotopes". In: *Nature* 112.2806 (1923), pp. 208–213. ISSN: 1476-4687. DOI: 10.1038/112208a0.

[120] Gregory Choppin, Jan-Olov Liljenzin, and Jan Rydberg. *Radiochemistry and nuclear chemistry*. Butterworth-Heinemann, 2002. ISBN: 978-0-12-405897-2.

[121] Sóti, Zsolt, Magill, Joseph, and Dreher, Raymond. "Karlsruhe Nuclide Chart 10th edition 2018 ". In: *EPJ Nuclear Sci. Technol.* 5 (2019), p. 6. DOI: 10.1051/epjn/2019004.

[122] Wolfgang Horst. *Frontiers of Nuclear Medicine/Aktuelle Nuklearmedizin*. Berlin Heidelberg: Springer Science Business Media, 2012. ISBN: 978-364-2650-949.

[123] Paul Breeze. *Nuclear Power*. Academic Press, 2017. ISBN: 978-008-1010-433. DOI: 10.1016/B978-0-08-101043-3.00003-1.

[124] Michael Shermer. "Fat Man and Little Boy: On the 75th Anniversary of Nuclear Weapons, a Moral Case for Their Use in Ending WWII and the Deterrence of Great Power Wars Since, and a Call to Eventually Eliminate Them". English. In: *Skeptic (Altadena, CA)* 25 (2020). 4, pp. 7+. ISSN: 10639330.

[125] Detlef Filges and Frank Goldenbaum. *Handbook of Spallation Research*. Wiley VCH Verlag GmbH, Dec. 16, 2009. ISBN: 3527407146. URL: https:

//www.ebook.de/de/product/8603487/detlef_filges_frank_
goldenbaum_handbook_of_spallation_research.html.

[126]   J. Benlliure. "Spallation Reactions in Applied and Fundamental Re-
        search". In: *The Euroschool Lectures on Physics with Exotic Beams, Vol. II.*
        Ed. by Jim Al-Khalili and Ernst Roeckl. Berlin, Heidelberg: Springer
        Berlin Heidelberg, 2006, pp. 191–238. ISBN: 978-3-540-33787-4. DOI:
        10.1007/3-540-33787-3_5.

[127]   W G Lynch. "Nuclear Fragmentation in Proton- and Heavy-Ion- In-
        duced Reactions". In: *Annual Review of Nuclear and Particle Science* 37.1
        (1987), pp. 493–535. DOI: 10.1146/annurev.ns.37.120187.002425.

[128]   Cyriel Wagemans. *The nuclear fission process*. CRC press, 1991. ISBN:
        978-0849354342.

[129]   Markus Borlein. *Kerntechnik*. Vogel Buchverlag, 2011. ISBN: 978-383-
        4331-311.

[130]   Y. Blumenfeld, T. Nilsson, and P. Van Duppen. "Facilities and methods
        for radioactive ion beam production". In: *Physica Scripta* T152 (2013),
        p. 014023. DOI: 10.1088/0031-8949/2013/t152/014023.

[131]   J.S. Al-Khalili and Ernst Roeckl. *The Euroschool Lectures on Physics with
        Exotic Beams Vol. I*. Berlin Heidelberg: Springer Science Business Me-
        dia, 2004. ISBN: 978-3-540-22399-3. DOI: 10.1007/b98790.

[132]   Otto Møgens Kofoed-Hansen. "The birth of on-line isotope separa-
        tion". In: *3rd International Conference on Nuclei Far from Stability* (1976).
        DOI: 10.5170/CERN-1976-013.65.

[133]   M Lindroos. *Review of the ISOL Method*. Tech. rep. CERN-AB-2004-
        086. revised version submitted on 2004-09-28 17:19:32. Geneva: CERN,
        2004. URL: https://cds.cern.ch/record/793447.

[134]   Ragnar Hellborg and Harry J Whitlow. "Charged particle optics and
        beam transport". In: *The Electrostatic Accelerator*. 2053-2571. Morgan
        Claypool Publishers, 2019, 15–1 to 15–13. ISBN: 978-1-64327-356-3. DOI:
        10.1088/2053-2571/aaea76ch15.

[135] Miklos Szilagyi. *Electron and ion optics*. Springer Science & Business Media, 2012. ISBN: 978-1-4613-0923-9. DOI: 10.1007/978-1-4613-0923-9.

[136] Martin Reiser and Patrick O'Shea. *Theory and design of charged particle beams*. Vol. 312. Wiley Online Library, 1994. ISBN: 0471306169.

[137] Poul Dahl. *Introduction to electron and ion optics*. Elsevier, 1973. ISBN: 978-0-12-200650-0. DOI: 10.1016/B978-0-12-200650-0.X5001-6.

[138] Jean Buon. "Beam phase space and emittance; rev. version". In: (1992), 27 p. DOI: 10.5170/CERN-1994-001.89.

[139] J. Liouville. "Note on the Courant and Snyder Invariant". In: *J. Math. Pures. Appl* 16 (1837).

[140] Ernest D. Courant, M. Stanley Livingston, and Hartland S. Snyder. "The Strong-Focusing Synchroton—A New High Energy Accelerator". In: *Phys. Rev.* 88 (5 1952), pp. 1190–1196. DOI: 10.1103/PhysRev.88.1190.

[141] H. Wollnik. "Mass separators". In: *Nuclear Instruments and Methods in Physics Research Section A: Accelerators, Spectrometers, Detectors and Associated Equipment* 258.3 (1987), pp. 289–296. ISSN: 0168-9002. DOI: https://doi.org/10.1016/0168-9002(87)90907-7.

[142] Philip E Miller and M Bonner Denton. "The quadrupole mass filter: basic operating concepts". In: *Journal of chemical education* 63.7 (1986), p. 617. DOI: 10.1021/ed063p617.

[143] Peter H Dawson. *Quadrupole Mass Spectrometry and its Applications*. Elsevier Science Ltd, 1976. ISBN: 978-0-444-41345-1. DOI: 10.1016/C2013-0-04436-2.

[144] Klaus Blaum. "Resonante Laserionisations-Massenspektrometrie an Gadolinium zur IsotopenhäuÞgkeitsanalyse mit geringsten Mengen". PhD thesis. Johannes Gutenberg-Universität Mainz, 2000.

[145] V. D. Berkout and V. M. Doroshenko. "Improving the Quality of the Ion Beam Exiting a Quadrupole Ion Guide". In: *Journal of the American Society for Mass Spectrometry* 17.3 (2006), pp. 335–340. ISSN: 1044-0305. DOI: https://doi.org/10.1016/j.jasms.2005.12.002.

[146] Peter Strehl. *Beam instrumentation and diagnostics*. Vol. 120. Springer, 2006. ISBN: 978-3-540-26404-0. DOI: 10.1007/3-540-26404-3.

[147] Peter Forck. "Lecture notes on beam instrumentation and diagnostics". In: *Joint Universities Accelerator School (JUAS 2010)* (2010).

[148] P. G. Hansen. *History of CERN, III*. Amsterdam: North-Holland, 1996. ISBN: 9780444896551.

[149] E. Kugler et al. "The new CERN-ISOLDE on-line mass-separator facility at the PS-Booster". In: *Nuclear Instruments and Methods in Physics Research Section B: Beam Interactions with Materials and Atoms* 70.1 (1992), pp. 41 –49. ISSN: 0168-583X. DOI: https://doi.org/10.1016/0168-583X(92)95907-9.

[150] Esma Mobs. "The CERN accelerator complex - 2019. Complexe des accélérateurs du CERN - 2019". In: (2019). General Photo. URL: https://cds.cern.ch/record/2684277.

[151] O. Kester et al. "Accelerated radioactive beams from REX-ISOLDE". In: *Nuclear Instruments and Methods in Physics Research Section B: Beam Interactions with Materials and Atoms* 204 (2003). 14th International Conference on Electromagnetic Isotope Separators and Techniques Related to their Applications, pp. 20 –30. ISSN: 0168-583X. DOI: https://doi.org/10.1016/S0168-583X(02)01886-4.

[152] D. Habs et al. "The REX-ISOLDE project". In: *Nuclear Instruments and Methods in Physics Research Section B: Beam Interactions with Materials and Atoms* 126.1 (1997). International Conference on Electromagnetic Isotope Separators and Techniques Related to Their Applications, pp. 218 –223. ISSN: 0168-583X. DOI: https://doi.org/10.1016/S0168-583X(97)01036-7.

[153] M. Lindroos et al. "HIE-ISOLDE". In: *Nuclear Instruments and Methods in Physics Research Section B: Beam Interactions with Materials and Atoms* 266.19 (2008). Proceedings of the XVth International Conference on Electromagnetic Isotope Separators and Techniques Related to their Applications, pp. 4687 –4691. ISSN: 0168-583X. DOI: https://doi.org/10.1016/j.nimb.2008.05.136.

[154] Mats Lindroos and Thomas Nilsson. *HIE-ISOLDE: the technical options. The High Intensity and Energy ISOLDE (HIE-ISOLDE) project.* CERN Yellow Reports: Monographs. Geneva: CERN, 2006. DOI: 10.5170/CERN-2006-013.

[155] Buehler L. Lawson Z. Marzari S.-Stachura M. Stora T. Dos Santos Augusto R.M. "CERN-MEDICIS (Medical Isotopes Collected from ISOLDE): A New Facility". In: *Applied Sciences* 4.2 (2014), pp. 256–281. DOI: https://doi.org/10.1016/0168-583X(92)95907-9.

[156] Wilkins S. Fedosseev V.N. et al. Gadelshin V.M. "First laser ions at the CERN-MEDICIS facility". In: *Hyperfine Interact* 241.55 (2020). DOI: https://doi.org/10.1007/s10751-020-01718-y.

[157] I. Podadera-Aliseda. "New developments on preparation of cooled and bunched Radioactive Ion beams at ISOL facilities: the ISCOOL project and the rotating wall cooling". Presented on 07 Jul 2006. 2006. URL: https://cds.cern.ch/record/975263.

[158] Mané, E. et al. "An ion cooler-buncher for high-sensitivity collinear laser spectroscopy at ISOLDE". In: *Eur. Phys. J. A* 42.3 (2009), pp. 503–507. DOI: 10.1140/epja/i2009-10828-0.

[159] J.P. Ramos et al. "Design and tests for the new CERN-ISOLDE spallation source: an integrated tungsten converter surrounded by an annular UCx target operated at 2000°C". In: *Nuclear Instruments and Methods in Physics Research Section B: Beam Interactions with Materials and Atoms* 463 (2020), pp. 357 –363. ISSN: 0168-583X. DOI: https://doi.org/10.1016/j.nimb.2019.04.060.

[160] Richard Catherall et al. "Radioactive ion beams produced by neutron-induced fission at ISOLDE". In: *Nuclear Instruments and Methods in Physics Research Section B: Beam Interactions with Materials and Atoms* 204 (2003). 14th International Conference on Electromagnetic Isotope Separators and Techniques Related to their Applications, pp. 235–239. ISSN: 0168-583X. DOI: https://doi.org/10.1016/S0168-583X(02)01915-8.

[161] T. Stora. "Recent developments of target and ion sources to produce ISOL beams". In: *Nuclear Instruments and Methods in Physics Research Section B: Beam Interactions with Materials and Atoms* 317 (2013). XVIth International Conference on ElectroMagnetic Isotope Separators and Techniques Related to their Applications, December 2–7, 2012 at Matsue, Japan, pp. 402 –410. ISSN: 0168-583X. DOI: https://doi.org/10.1016/j.nimb.2013.07.024.

[162] U Köster. "ISOLDE target and ion source chemistry". In: *Radiochim. Acta* 89.CERN-OPEN-2001-075. 11-12 (2001), 749–756. 9 p. URL: https://cds.cern.ch/record/526080.

[163] Joao Pedro Ramos. "Titanium carbide-carbon porous nanocomposite materials for radioactive ion beam production: processing, sintering and isotope release properties". Presented 26 Jan 2017. 2017. URL: https://cds.cern.ch/record/2243566.

[164] O.W. Richardson. "LI. Some applications of the electron theory of matter". In: *The London, Edinburgh, and Dublin Philosophical Magazine and Journal of Science* 23.136 (1912), pp. 594–627. DOI: https://doi.org/10.1080/14786440408637250.

[165] O. W. Richardson. "Electron Emission from Metals as a Function of Temperature". In: *Phys. Rev.* 23 (2 1924), pp. 153–155. DOI: 10.1103/PhysRev.23.153.

[166] Saul Dushman. "Electron Emission from Metals as a Function of Temperature". In: *Phys. Rev.* 21 (6 1923), pp. 623–636. DOI: 10.1103/PhysRev.21.623.

[167] M. Huyse. "Ionization in a hot cavity". In: *Nuclear Instruments and Methods in Physics Research* 215.1 (1983), pp. 1 –5. ISSN: 0167-5087. DOI: https://doi.org/10.1016/0167-5087(83)91284-X.

[168] R. Kirchner. "On the thermoionization in hot cavities". In: *Nuclear Instruments and Methods in Physics Research Section A: Accelerators, Spectrometers, Detectors and Associated Equipment* 292.2 (1990), pp. 203 –208. ISSN: 0168-9002. DOI: https://doi.org/10.1016/0168-9002(90)90377-I.

[169] Fabio Schwellnus. "Entwicklung von Ionenquellen zur Optimierung von Selektivität und Effizienz bei der resonanten Laserionisation". PhD thesis. 2010. URL: http://doi.org/10.25358/openscience-4621.

[170] V. I. Mishin, A. L. Malinovsky, and D. V. Mishin. "Resonant Ionization Laser Ion Source (RILIS) With Improved Selectivity Achieved By Ion Pulse Compression Using In-Source Time-of-flight Technique". In: *AIP Conference Proceedings* 1104.1 (2009), pp. 207–212. DOI: 10.1063/1.3115604.

[171] S. Rothe et al. "Laser ion beam production at CERN-ISOLDE: New features – More possibilities". In: *Nuclear Instruments and Methods in Physics Research Section B: Beam Interactions with Materials and Atoms* 376 (2016). Proceedings of the XVIIth International Conference on Electromagnetic Isotope Separators and Related Topics (EMIS2015), Grand Rapids, MI, U.S.A., 11-15 May 2015, pp. 91–96. ISSN: 0168-583X. DOI: https://doi.org/10.1016/j.nimb.2016.02.024.

[172] Katerina Chrysalidis. "Improving the Spectral Coverage and Resolution of the ISOLDE RILIS". Presented 29 Nov 2019. PhD thesis. 2019. DOI: 10.17181/CERN.8OTS.NL3N.

[173] Valentin Fedosseev et al. "Ion beam production and study of radioactive isotopes with the laser ion source at ISOLDE". In: *Journal of Physics G: Nuclear and Particle Physics* 44.8 (2017), p. 084006. DOI: 10.1088/1361-6471/aa78e0.

[174] F. Scheerer et al. "A chemically selective laser ion source for on-line mass separation". In: *Review of Scientific Instruments* 63 (1992), pp. 2831 –2833. DOI: 10.1063/1.1142820.

[175] V.I. Mishin et al. "Chemically selective laser ion-source for the CERN-ISOLDE on-line mass separator facility". In: *Nuclear Instruments and Methods in Physics Research Section B: Beam Interactions with Materials and Atoms* 73.4 (1993), pp. 550 –560. ISSN: 0168-583X. DOI: https://doi.org/10.1016/0168-583X(93)95839-W.

[176] V.N. Fedosseev et al. "ISOLDE RILIS: New beams, new facilities". In: *Nuclear Instruments and Methods in Physics Research Section B: Beam Interactions with Materials and Atoms* 266.19 (2008). Proceedings of the XVth International Conference on Electromagnetic Isotope Separators and Techniques Related to their Applications, pp. 4378 –4382. ISSN: 0168-583X. DOI: https://doi.org/10.1016/j.nimb.2008.05.038.

[177] L. Penescu et al. "Development of high efficiency Versatile Arc Discharge Ion Source at CERN ISOLDE". In: *Review of Scientific Instruments* 81.2 (2010), 02A906. DOI: 10.1063/1.3271245.

[178] R. Kirchner and E. Roeckl. "A novel ISOL ion source". In: *Nuclear Instruments and Methods* 139 (1976), pp. 291 –296. ISSN: 0029-554X. DOI: https://doi.org/10.1016/0029-554X(76)90687-X.

[179] C. D. Child. "Discharge From Hot CaO". In: *Phys. Rev. (Series I)* 32 (5 1911), pp. 492–511. DOI: 10.1103/PhysRevSeriesI.32.492.

[180] Liviu Constantin Penescu. "Techniques to produce and accelerate radioactive ion beams. Tehnici de producere si accelerare a fasciculelor radioactive". Presented 2009. PhD thesis. 2009. URL: https://cds.cern.ch/record/2259078.

[181] Y. Martinez Palenzuela et al. "Enhancing the extraction of laser- ionized beams from an arc discharge ion source volume". In: *Nuclear Instruments and Methods in Physics Research Section B: Beam Interactions*

with Materials and Atoms 431 (2018), pp. 59 –66. ISSN: 0168-583X. DOI: https://doi.org/10.1016/j.nimb.2018.06.006.

[182] T. Day Goodacre et al. "Blurring the boundaries between ion sources: The application of the RILIS inside a FEBIAD type ion source at ISOL-DE". In: *Nuclear Instruments and Methods in Physics Research Section B: Beam Interactions with Materials and Atoms* 376 (2016). Proceedings of the XVIIth International Conference on Electromagnetic Isotope Separators and Related Topics (EMIS2015), Grand Rapids, MI, U.S.A., 11-15 May 2015, pp. 39 –45. ISSN: 0168-583X. DOI: https://doi.org/10.1016/j.nimb.2016.03.005.

[183] Liviu Penescu et al. "Arc Discharge Ion Source Development at CERN ISOLDE". In: *University" Politehnica" of Bucharest Scientific Bulletin, Series A: Applied Mathematics and Physics* 72.2 (2010), pp. 121–132. URL: https://cds.cern.ch/record/1359345.

[184] Jochen Ballof. In preparation. PhD thesis. 2021.

[185] T. K. Sato et al. "Measurement of the first ionization potential of lawrencium, element 103". In: *Nature* 520.7546 (2015), pp. 209–211. ISSN: 1476-4687. DOI: 10.1038/nature14342.

[186] D.A. Fink et al. "On-line implementation and first operation of the Laser Ion Source and Trap at ISOLDE/CERN". In: *Nuclear Instruments and Methods in Physics Research Section B: Beam Interactions with Materials and Atoms* 344 (2015), pp. 83–95. ISSN: 0168-583X. DOI: https://doi.org/10.1016/j.nimb.2014.12.007.

[187] R. Heinke. "In-source high-resolution spectroscopy of holmium radioisotopes - On-line tailored perpendicular laser interaction at ISOL-DEs Laser Ion Source and Trap LIST". Presented 16 Oct 2019. PhD thesis. 2019. URL: https://cds.cern.ch/record/2718446.

[188] Katja Wies. "Entwicklung des Laserionenquellen- und fallenprojekts LIST fur Ultraspurendetektion und Grundlagenforschung". PhD thesis. 2006. DOI: 10.25358/openscience-909.

[189] G. D. Alton et al. "A high efficiency, kinetic-ejection negative ion source for RIB generation". In: *AIP Conference Proceedings* 473.1 (1999), pp. 330–340. DOI: 10.1063/1.58953.

[190] G.D Alton et al. "A new concept kinetic-ejection negative-ion source for rib generation". In: *Nuclear Instruments and Methods in Physics Research Section B: Beam Interactions with Materials and Atoms* 170.3 (2000), pp. 515 –522. ISSN: 0168-583X. DOI: https://doi.org/10.1016/S0168-583X(00)00238-X.

[191] Jacques Lettry. "Off-Line Isotope Separator". In: (1994). URL: https://cds.cern.ch/record/2691985.

[192] ETP Ion Detect. *MagneToF detector*. ETP Ion Detect. Melrose Park, Australia, 2013. URL: https://www.etp-ms.com/file-repository/8.

[193] H. Frånberg et al. "Off-line commissioning of the ISOLDE cooler". In: *Nuclear Instruments and Methods in Physics Research Section B: Beam Interactions with Materials and Atoms* 266.19 (2008). Proceedings of the XVth International Conference on Electromagnetic Isotope Separators and Techniques Related to their Applications, pp. 4502–4504. ISSN: 0168-583X. DOI: https://doi.org/10.1016/j.nimb.2008.05.097.

[194] S. Warren et al. "Offline 2, ISOLDE's target, laser and beams development facility". In: *Nuclear Instruments and Methods in Physics Research Section B: Beam Interactions with Materials and Atoms* 463 (2020), pp. 115 –118. ISSN: 0168-583X. DOI: https://doi.org/10.1016/j.nimb.2019.07.016.

[195] Annie Ringvall-Moberg. In preparation. PhD thesis.

[196] D. Hanstorp. "A secondary emission detector capable of preventing detection of the photoelectric effect induced by pulsed lasers". In: *Measurement Science and Technology* 3.5 (1992), p. 523. DOI: 10.1088/0957-0233/3/5/013.

[197] Francesco Bonaccorso et al. "Graphene photonics and optoelectronics". In: *Nature photonics* 4.9 (2010), p. 611. DOI: `10.1038/nphoton.2010.186`.

[198] Lars Bengtsson. "24-channel dual microcontroller-based voltage controller for ion optics remote control". In: *Nuclear Instruments and Methods in Physics Research Section A: Accelerators, Spectrometers, Detectors and Associated Equipment* 890 (2018), pp. 96–101. ISSN: 0168-9002. DOI: `https://doi.org/10.1016/j.nima.2018.02.035`.

[199] H. Wollnik and M. Przewloka. "Time-of-flight mass spectrometers with multiply reflected ion trajectories". In: *International Journal of Mass Spectrometry and Ion Processes* 96.3 (1990), pp. 267–274. ISSN: 0168-1176. DOI: `https://doi.org/10.1016/0168-1176(90)85127-N`.

[200] Frank Wienholtz et al. "Towards ultrahigh-resolution multi-reflection time- of-flight mass spectrometry at ISOLTRAP". In: *Physica Scripta* 2015.T166 (2015), p. 014068. DOI: `10.1088/0031-8949/2015/t166/014068`.

[201] R.N. Wolf et al. "ISOLTRAP's multi-reflection time-of-flight mass separator/spectrometer". In: *International Journal of Mass Spectrometry* 349 (2013), pp. 123–133. DOI: `10.1016/j.ijms.2013.03.020`.

[202] S. Sels et al. "First steps in the development of the Multi Ion Reflection Apparatus for Collinear Laser Spectroscopy". In: *Nuclear Instruments and Methods in Physics Research Section B: Beam Interactions with Materials and Atoms* 463 (2020), pp. 310–314. ISSN: 0168-583X. DOI: `https://doi.org/10.1016/j.nimb.2019.04.076`.

[203] S. Malbrunot-Ettenauer. *Benchmarking of a Multi Ion Reflection Apparatus for Collinear Laser Spectroscopy of radionuclides*. Tech. rep. CERN-INTC-2017-070. INTC-I-197. Geneva: CERN, 2017. URL: `https://cds.cern.ch/record/2266836`.

[204] F.M. Maier et al. "Simulations of a proof-of-principle experiment for collinear laser spectroscopy within a multi-reflection time-of-flight device". In: *Hyperfine Interactions* 240.1 (2019), pp. 1–13. DOI: 10.1007/s10751-019-1575-x.

[205] F. Wienholtz et al. "Mass-selective ion ejection from multi-reflection time-of-flight devices via a pulsed in-trap lift". In: *International Journal of Mass Spectrometry* 421 (2017), pp. 285–293. ISSN: 1387-3806. DOI: https://doi.org/10.1016/j.ijms.2017.07.016.

[206] Robert N. Wolf et al. "Static-mirror ion capture and time focusing for electrostatic ion-beam traps and multi-reflection time-of-flight mass analyzers by use of an in-trap potential lift". In: *International Journal of Mass Spectrometry* 313 (2012), pp. 8–14. ISSN: 1387-3806. DOI: https://doi.org/10.1016/j.ijms.2011.12.006.

[207] Franziska Maria Maier. "Laser Spectroscopy of Short-Lived- Radionuclides in an Ion Trap: MIRACLS proof-of-principle experiment and the simulation of the future 30-keV MR-ToF device". Universität Linz, 2019. URL: https://miracls.web.cern.ch/theses/FranziskaMaier.pdf.

[208] Fabian Hummer. "Investigation of Space Charge Effects in MIRACLS' Proof-of-Principle MR-ToF Device". Universität Linz, 2019. URL: https://miracls.web.cern.ch/theses/FabianHummer.pdf.

[209] L. Fischer. "Improvements of the beam intensity of stable Mg ions for the proof-of-principle experiment of collinear laser spectroscopy on short-lived nuclides in a multi ion reflection apparatus". Bachelor's thesis, CERN, 2018. URL: https://miracls.web.cern.ch/theses/LaurinFischer.pdf.

[210] T. H. Maiman. "Stimulated Optical Radiation in Ruby". In: *Nature* 187.4736 (1960), pp. 493–494. ISSN: 1476-4687. DOI: 10.1038/187493a0.

[211] P. A. Franken et al. "Generation of Optical Harmonics". In: *Phys. Rev. Lett.* 7 (4 1961), pp. 118–119. DOI: 10.1103/PhysRevLett.7.118.

[212] O.I. Klyushnikov. "Method to determine the work function using X-ray photoelectron spectroscopy". In: *Journal of structural chemistry* 39.6 (1998), pp. 944–947. DOI: 10.1007/BF02903611.

[213] Michiko Yoshitake. "Measurement of Work Function". In: *Work Function and Band Alignment of Electrode Materials: The Art of Interface Potential for Electronic Devices, Solar Cells, and Batteries*. Tokyo: Springer Japan, 2021, pp. 71–95. ISBN: 978-4-431-56898-8. DOI: 10.1007/978-4-431-56898-8_4.

[214] S. Evans. "Work function measurements by X-Pe spectroscopy, and their relevance to the calibration of X-Pe spectra". In: *Chemical Physics Letters* 23.1 (1973), pp. 134–138. ISSN: 0009-2614. DOI: https://doi.org/10.1016/0009-2614(73)89582-X.

[215] Valentine Petit. "Conditioning of Surfaces in Particle Accelerators. Conditionnement des surfaces dans les accelerateurs de particules". Presented 17 Jan 2020. PhD thesis. 2019. DOI: 10.17181/CERN.941V.OBEC.

[216] William Lawrence Bragg. "The Specular Reflection of X-rays." In: *Nature* 90.2250 (1912), pp. 410–410. DOI: 10.1038/090410b0.

[217] William Lawrence Bragg. "The structure of some crystals as indicated by their diffraction of X-rays". In: *Proceedings of the Royal Society of London. Series A, Containing papers of a mathematical and physical character* 89.610 (1913), pp. 248–277. DOI: 10.1098/rspa.1913.0083.

[218] A.A. Avdienko and MD Malev. "Poisoning of LaB_6 cathodes". In: *Vacuum* 27.10 (1977), pp. 583–588. ISSN: 0042-207X. DOI: https://doi.org/10.1016/S0042-207X(77)80438-7.

[219] F. Schwellnus et al. "Study of low work function materials for hot cavity resonance ionization laser ion sources". In: *Nuclear Instruments and Methods in Physics Research Section B: Beam Interactions with Materials and Atoms* 267.10 (2009), pp. 1856–1861. ISSN: 0168-583X. DOI: https://doi.org/10.1016/j.nimb.2009.02.068.

[220] Ryan M. Jacobs, Dane Morgan, and John H Booske. "Strontium vanadate: An ultra-low work function electron emission material". In: *2015 IEEE International Vacuum Electronics Conference (IVEC)*. IEEE. 2015, pp. 1–2. DOI: 10.1109/IVEC.2015.7223772.

[221] Ryan M. Jacobs, Dane Morgan, and John H Booske. "Doped strontium vanadate: Computational design of a stable, low work function material". In: *2016 IEEE International Vacuum Electronics Conference (IVEC)*. IEEE. 2016, pp. 1–2. DOI: 10.1109/IVEC.2016.7561807.

[222] J. Macias, A.A. Yaremchenko, and J.R. Frade. "Redox transitions in strontium vanadates: Electrical conductivity and dimensional changes". In: *Journal of Alloys and Compounds* 601 (2014), pp. 186–194. ISSN: 0925-8388. DOI: https://doi.org/10.1016/j.jallcom.2014.02.148.

[223] Javier Macías, Aleksey A Yaremchenko, and Jorge R Frade. "Enhanced stability of perovskite-like $SrVO_3$-based anode materials by donor-type substitutions". In: *Journal of Materials Chemistry A* 4.26 (2016), pp. 10186–10194. DOI: 10.1039/C6TA02672A.

[224] Takuji Maekawa, Ken Kurosaki, and Shinsuke Yamanaka. "Physical properties of polycrystalline SrVO3- δ". In: *Journal of alloys and compounds* 426.1-2 (2006), pp. 46–50. DOI: 10.1016/j.jallcom.2006.02.026.

[225] A.A. Yaremchenko et al. "Electrical conductivity, thermal expansion and stability of Y-and Al-substituted SrVO3 as prospective SOFC anode material". In: *Solid State Ionics* 247 (2013), pp. 86–93. DOI: 10.1016/j.ssi.2013.06.002.

[226] G. Bansal et al. "Cesium Delivery System for Negative Ion Source at IPR". In: *AIP Conference Proceedings* 1390.1 (2011), pp. 614–623. DOI: 10.1063/1.3637433.

[227] Takatoshi Morishita et al. "Mechanism of Negative Ion Production in a Cesium Seeded Ion Source". In: *Japanese Journal of Applied Physics* 40.Part 1, No. 7 (2001), pp. 4709–4714. DOI: 10.1143/jjap.40.4709.

[228] M. Fröschle et al. "Recent developments at IPP on evaporation and control of caesium in negative ion sources". In: *Fusion Engineering and Design* 84.2 (2009). Proceeding of the 25th Symposium on Fusion Technology, pp. 788–792. ISSN: 0920-3796. DOI: https://doi.org/10.1016/j.fusengdes.2008.12.063.

[229] P. Singh et al. "Characterization of in situ work function and cesium flux measurement setup suitable for cesium seeded negative ion source applications". In: *Nuclear Fusion* 59.10 (2019), p. 106023. DOI: 10.1088/1741-4326/ab312c.

[230] Thierry Stora. private communication. Mar. 2021.

[231] Yuan Liu. private communication. Mar. 5, 2021.

[232] Isaac Asimov. "The natural occurrence of short-lived radioisotopes". In: *Journal of Chemical Education* 30.12 (1953), pp. 616–617. DOI: 10.1021/ed030p398.

[233] Berta Karlik and Trande Bernert. "Das Element 85 in den natürlichen Zerfallsreihen". In: *Zeitschrift für Physik A Hadrons and Nuclei* 123.1-2 (1944), pp. 51–72. DOI: 10.1007/BF01375144.

[234] M. Zalutsky et al. "Astatine-211: production and availability." In: *Current Radiopharmaceuticals* 4.3 (2011), pp. 85–177. ISSN: 1874-4729. DOI: 10.2174/1874471011104030177.

[235] D.A. Mulford et al. "The promise of Targeted α-Particle Therapy." In: *Journal of Nuclear Medicine* 4.46 (2005), pp. 199–204. ISSN: 0161-5505. URL: https://jnm.snmjournals.org/content/46/1_suppl/199S.

[236] David Teze et al. "Targeted radionuclide therapy with astatine-211: Oxidative dehalogenation of astatobenzoate conjugates". In: *Scientific Reports* 7 (May 2017), p. 2579. DOI: 10.1038/s41598-017-02614-2.

[237] D.S. Wilbur. "Enigmatic astatine". In: *Nature Chemistry* 5 (Mar. 2013), p. 246. DOI: 10.1038/nchem.1580.

[238]   S. Rothe et al. "Measurement of the first ionization potential of as-tatine by laser ionization spectroscopy". In: *Nature Communications* 4 (2013), p. 1835. DOI: 10.1038/ncomms2819.

[239]   Zhiwei Chang et al. "Ionization Potentials, Electron Affinities, Res-onance Excitation Energies, Oscillator Strengths, And Ionic Radii of Element Uus (Z = 117) and Astatine". In: *The Journal of Physical Chem-istry A* 114.51 (2010), pp. 13388–13394. DOI: 10.1021/jp107411s.

[240]   Junqin Li et al. "Theoretical study for the electron affinities of negative ions with the MCDHF method". In: *Journal of Physics B: Atomic, Molec-ular and Optical Physics* 45.16 (2012), p. 165004. DOI: 10.1088/0953-4075/45/16/165004.

[241]   A. Borschevsky et al. "Ionization potentials and electron affinities of the superheavy elements 115-117 and their sixth-row homologues Bi, Po, and At". In: *Physical Review A* 91.2 (2015), p. 020501. ISSN: 10941622. DOI: 10.1103/PhysRevA.91.020501.

[242]   R. Si and C. Froese Fischer. "Electron affinities of At and its homol-ogous elements Cl, Br, and I". In: *Phys. Rev. A* 98 (5 2018), p. 052504. DOI: 10.1103/PhysRevA.98.052504.

[243]   Brian A. Finney and Kirk A. Peterson. "Beyond chemical accuracy in the heavy p-block: The first ionization potentials and electron affini-ties of Ga–Kr, In-Xe, and Tl–Rn". In: *The Journal of Chemical Physics* 151.2 (2019), p. 024303. DOI: 10.1063/1.5110174.

[244]   James G. Cubiss et al. "Charge radii and electromagnetic moments of $^{195-211}$At". In: *Physical Review C* 97 (5 2018), p. 054327. DOI: 10.1103/PhysRevC.97.054327.

[245]   R. J. Peláez et al. "Pulsed photodetachment microscopy and the elec-tron affinity of iodine". In: *Journal of Physics B: Atomic, Molecular and Optical Physics* 42.12 (2009), p. 125001. DOI: 10.1088/0953-4075/42/12/125001.

[246] DIRAC, a relativistic ab initio electronic structure program, Release DIRAC15 (2015), written by R. Bast, T. Saue, L. Visscher, and H. J. Aa. Jensen, with contributions from V. Bakken, K. G. Dyall, S. Dubillard, U. Ekstroem, E. Eliav, T. Enevoldsen, E. Fasshauer, T. Fleig, O. Fossgaard, A. S. P. Gomes, T. Helgaker, J. Henriksson, M. Ilias, Ch. R. Jacob, S. Knecht, S. Komorovsky, O. Kullie, J. K. Laerdahl, C. V. Larsen, Y. S. Lee, H. S. Nataraj, M. K. Nayak, P. Norman, G. Olejniczak, J. Olsen, Y. C. Park, J. K. Pedersen, M. Pernpointner, R. Di Remigio, K. Ruud, P. Salek, B. Schimmelpfennig, J. Sikkema, A. J. Thorvaldsen, J. Thyssen, J. van Stralen, S. Villaume, O. Visser, T. Winther, and S. Yamamoto (see http://www.diracprogram.org).

[247] T Carette and M R Godefroid. "Isotope shift on the chlorine electron affinity revisited by an MCHF/CI approach". In: *Journal of Physics B: Atomic, Molecular and Optical Physics* 46.9 (2013), p. 095003. DOI: 10.1088/0953-4075/46/9/095003.

[248] J. Ballof et al. "The upgraded ISOLDE yield database – A new tool to predict beam intensities". In: *Nuclear Instruments and Methods in Physics Research Section B: Beam Interactions with Materials and Atoms* 463 (2020), pp. 211 –215. ISSN: 0168-583X. DOI: https://doi.org/10.1016/j.nimb.2019.05.044.

[249] Thierry Gharsa. private communication. Feb. 22, 2020.

[250] S Rothe et al. *Determination of the electron affinity of astatine and polonium by laser photodetachment*. Tech. rep. CERN-INTC-2016-017. INTC-P-462. Geneva: CERN, 2016. DOI: 10.17181/CERN.OZFJ.5MKK.

[251] Junqin Li et al. "Theoretical study for the electron affinities of negative ions with the MCDHF method". In: *Journal of Physics B: Atomic, Molecular and Optical Physics* 45.16 (2012), p. 165004. DOI: 10.1088/0953-4075/45/16/165004.

[252] Jochen Ballof. Yield database. Accessed 2021-March-10. URL: https://isoyields2.web.cern.ch/YieldBasic.aspx?Z=84.

[253]   H. T. Schmidt et al. "Rotationally Cold OH$^-$ Ions in the Cryogenic Electrostatic Ion-Beam Storage Ring DESIREE". In: *Phys. Rev. Lett.* 119 (7 2017), p. 073001. DOI: 10.1103/PhysRevLett.119.073001.

[254]   Dahl D. Manura D. *Simion (r) 8.1 user manual*. Scientific Instrument Service. 2013.

[255]   Sebastian Raeder. "Spurenanalyse von Aktiniden in der Umwelt mittels Resonanzionisations-Massenspektrometrie". PhD thesis. Johannes Gutenberg-Universität Mainz, 2010. DOI: 10.25358/openscience-4788.

[256]   *Minutes of the 61st meeting of the INTC held on Tuesday 2 and Wednesday 3 July 2019*. Tech. rep. Geneva: CERN, 2019. URL: https://cds.cern.ch/record/2681119.

[257]   *Minutes of the 56th meeting of the INTC held on Wednesday 28 and Thursday, 29 June 2017*. Tech. rep. Geneva: CERN, 2017. URL: https://cds.cern.ch/record/2290441.

Curriculum Vitae

Personal Data

Name:	David Leimbach
Adress:	Rue de la Gare 9, 01710 Thoiry, France
Nationality:	German
Phone:	0041754111731
Email:	David.leimbach@cern.ch
Date of birth:	05.03.1992

Education

From 02/2018-present	Doctoral student at CERN and the Johannes Guttenberg-Universität Mainz
04/2017-12/2017	Master thesis project at CERN-ISOLDE
from 08/2016-03/2017	Continuation of master studies abroad at the University of Gothenburg
10/2015-12/2017	M.Sc. in physics at the Philipps-University Marburg
10/2011-09/2015	B.Sc. in physics at the Philipps-University Marburg
06/2002 – 07/ 2011	Gymnasium Elisabethschule Marburg; graduated with Abitur

Experience

04/2015- September 2016	**Research assistant** at the research group „Laserspectroscopy" led by PD Dr. Sangam Chatterjee at the Philipps-University of Marburg
04/2013- September 2016	**Student assistant** at the Faculty of Physics at the Philipps-University of Marburg teaching physics and supervising lab work of students from the departments of: - Biology - Pharmacy - Dentistry - Medicine
18/01/2010-29/01/2010	**Internship** at the High-Tech Gründerfonds in Bonn, Germany
12/03/2007-23/3/2007	**Internship** at the police Department Marburg-Biedenkopf, Germany

Particular expertise

Languages:
- German (mother tongue)
- English (C1)
- French (beginner)

Programming skills:
- LabView, Python, Mathematica
- SIMION, CST Studio, COMSOL

Additonal Information

Conferences:
- DPG Frühjahrstagung 2015 (poster presentation)
- ICIS 2017 (poster presentation)
- ISOLDE workshop and Users meeting 2017 (award for best poster presentation)
- EMIS 2018 (poster presentation)
- ISOLDE workshop and Users meeting 2018 (invited talk)
- DPG Frühjahrstagung Rostock 2019 (oral presentation)
- ISOLDE physics group seminar 2019 (invited talk)
- PLATAN 2019 (oral presentation)
- ICPEAC 2019 (poster presentation)
- ISOLDE workshop and Users meeting 2020 (invited talk)

Publications:
- J. Warbinek, D. Leimbach, D. Lu *et al.,* A graphene-based neutral particle detector, Applied Physics Letters 114, 061902 (2019) https://doi.org/10.1063/1.5080517
- D. Leimbach, *et al.*, Upgrades of the GANDALPH photodetachment detector towards the determination of the electron affinity of astatine, Nuclear Instruments and Methods in Physics Research Section B: Beam Interactions with Materials and Atoms 463, Pages 277-279, (2020), ISSN 0168-583X, https://doi.org/10.1016/j.nimb.2019.05.015.
- D. Leimbach, Karls, J., Guo, Y. *et al.* The electron affinity of astatine. *Nat Commun* **11,** 3824 (2020). https://doi.org/10.1038/s41467-020-17599-2

Further education:
- Habilitation electrique (2017)
- ISOLDE- Experimental Hall-Radiation Protection and electrical safety (2017)
- Vsim workshop (Leuven, 2018)
- LabView core 1 and 2 (2019)
- Fluka beginers course (2018)
- VSim workshop at EMIS (2018)
- COMSOL Electromagnetics Modeling Day (2019)
- Scientific writing course (2019)
- CERN accelerator school (2019)
- SmarTeam- Catia data manager at CERN (2019)
- Python for Beginners (online course at udemy.com, 2020)

Drivers License: German „Klasse B"

Hobbys:
- Running
- Football
- Traveling
- Socialising
- Reading